Porous Electrode Modeling and its Applications to Li-ion Batteries

Zhiqiang Chen[a,b], Dmitri L. Danilov[a,b], Rüdiger-A. Eichel[b,c], Peter H.L. Notten[a,b,d,*]

[a]Eindhoven University of Technology, Eindhoven, 5600 MB, the Netherlands
[b]Fundamental Electrochemistry (IEK-9), Forschungszentrum Jülich, D-52425, Germany
[c]RWTH Aachen University, Aachen, D-52074, Germany
[d]University of Technology Sydney, Broadway, Sydney, NSW 2007, Australia

* Corresponding author: p.h.l.notten@tue.nl

Abstract

Battery modeling has become increasingly important with the intensive development of Li-ion batteries (LIBs). The porous electrode model, relating battery performances to the internal physical and (electro)chemical processes, is one of the most adopted models in scientific research and engineering fields. Since Newman and coworkers' first implementation in the 1990s, the porous electrode model has kept its general form. Soon after that, many publications have focused on the applications to LIBs. In this review, the applications of the porous electrode model to LIBs are systematically summarized and discussed. With this model, various internal battery properties have been studied, such as Li^+ concentration and electric potential in the electrolyte and electrodes, reaction rate distribution, overpotential, and impedance. When coupled with thermal, mechanical, and aging models, the porous electrode model can simulate the temperature and stress distribution inside batteries and predict degradation during battery operation. With the help of state observers, the porous electrode model can monitor various battery states in real-time for battery management systems (BMS). Even though the porous electrode models have multiple advantages, some challenges and limitations still have to be addressed. The present review also gives suggestions to overcome these limitations in future research.

Keywords: Porous electrode model, Performance modeling, Li-ion battery

1. Introduction

The demand for energy has increased enormously due to economic and technological developments and the growth of the world population. Traditional fossil fuels are still dominant in the energy and power supply due to their conveniences to use. The massive consumption will definitely deplete these fuels in the future because they are non-renewable. The low energy utilization efficiency is also causing tremendous energy waste. Furthermore, the consequent emission of greenhouse gases and other pollutants will cause global warming and other severe environmental problems [1-3]. Therefore, exploring alternative energy sources is urgent and demanding in the energy research field.

Renewable energy sources, such as solar, wind, marine, and geothermal energies, are excellent candidates because they are safe, clean, permanent, and environment friendly. However, the intermittent nature limits the extensive applications of these renewable energy sources because it is challenging to meet the constant demand. Using energy storage systems is an essential solution to buffer the energy input and provide continuous supply. The battery-based stationary energy storage devices are currently the most popular energy storage systems for renewable energy sources. Li-ion batteries (LIBs) play a dominant role among all battery systems due to their excellent characteristics, such as high energy and power density, high coulombic and energy efficiency, and low cost [4, 5]. In addition to applications in stationary energy storage devices, LIBs are also widely used in portable electronic devices, electric vehicles (EV), and hybrid electric vehicles (HEV).

A typical Li-ion battery consists of a positive electrode (cathode), a negative electrode (anode), a separator, and an electrolyte. The positive and negative electrodes usually are made up of current collectors, active materials, conducting additives, and polymer binders. The separator is a porous polymer membrane; an electronic insulator sandwiched between the positive and negative electrodes. The electrolyte is an electronic insulator but an ionic conductor. It provides an ionic pathway between the cathode and anode. According to the composition, the electrolytes can be classified as liquid, solid polymer, and solid inorganic electrolytes [6, 7]. During the operation of LIBs, electrochemical charge-transfer reactions occur at the surface of the electrode active materials with the simultaneous movement of electrons and ions [8]. Equations 1 and 2 show the partial electrochemical reactions of a typical intercalation-type $LiMO_2/C_6$ cell, respectively, which involve the charge transfer reactions at the positive and negative electrodes, according to

$$\mathrm{LiMO_2} \underset{\text{discharge}}{\overset{\text{charge}}{\rightleftarrows}} \mathrm{Li_{1-x}MO_2} + x\mathrm{Li^+} + xe^-, \quad (1)$$

and

$$\mathrm{C_6} + y\mathrm{Li^+} + ye^- \underset{\text{discharge}}{\overset{\text{charge}}{\rightleftarrows}} \mathrm{Li}_y\mathrm{C_6}\,. \quad (2)$$

During charging, electrons released from the positive electrode flow to the negative electrode through the connecting external circuit. Electrochemical oxidation and reduction reactions occur simultaneously at the positive and negative electrodes with the extraction and insertion of Li^+ to keep electro-neutrality. Subsequently, Li-ions move from the positive electrode to the negative electrode via the electrolyte by diffusion and migration. As a result, an electric potential difference between the two electrodes evolves. These processes are reversed when the battery is discharging. For this reason, the LIBs are initially called 'rocking-chair cells'.

Considering the complexity of the physical and electrochemical processes occurring inside batteries, modeling is a powerful tool for developing more advanced batteries. Multiscale models have been proposed and developed to mathematically accounting for the physical and (electro)chemical phenomena at different spatial scales [9-12]. At atomic level, some modeling tools, such as density functional theory (DFT) calculations and molecular dynamics (MD) simulations, are adopted to invertigate the material fundamental properties based on quantum mechanics or Newton's law [13]. At mesoscale level (from cluster to electrode), the phase-field (PF) modeling is frequently used to study physical and chemical reactions within a microstructure [14], such as dendrite growth and crack propagation. At macroscale level (from particle to cell), models are used to optimize the electrode and battery design by considering the relationship between battery design parameters and performance. This is also crucial for many engineering applications [11, 15, 16], such as degradation awareness and battery states monitoring.

The review of DFT calculations and PF modeling can be found elsewhere [14, 17]. The present review focuses more on the macroscale modeling. Three kinds of macroscale models are commonly distinguished: empirical models, equivalent circuit models, and electrochemical models [18-22]. Empirical models use experimental data to derive empirical equations through a fitting process. Such equations are further used to determine various battery parameters like the terminal voltage, throughput current, surface temperature, and State-of-Charge (SoC) [18]. These models are simple and easy to implement. However, the accuracy of these models is relatively

low due to the highly non-linear behavior of batteries under dynamic loading conditions. The estimated parameters usually do not have a physical meaning. Therefore, the simulations are only valid in the interpolation regions [18, 19].

The equivalent circuit model (ECM) uses a series of electrical circuit components, such as resistances and capacitances, to describe the relationship between the current and terminal voltage of batteries [19]. Due to its simplicity and easy implementation, ECM is frequently adopted in battery impedance modeling and online battery state estimations [15, 23]. ECM can also be applied to model thermal behavior [24]. Compared to empirical models, ECM has a physical meaning in terms of electrical circuit components [20, 22]. They can, to some extent, help in understanding the battery performance. By adding more electrical circuit components, the accuracy of ECM can be improved [19]. However, ECM generally lacks predictive power and suffers from poor out-of-sample performance. That means ECM can accurately fit the available data set but cannot predict the behavior of the battery for different experimental conditions. It is also challenging for ECM to forecast battery degradation and parameters of aged cells [25].

Electrochemical models describe the thermodynamics, the (electro)chemical reaction kinetics, and transport processes inside batteries. They provide a sophisticated and advanced tool for reaction mechanistic analysis, battery design optimization, battery state estimation, *etc*. One of the most famous electrochemical models is the porous electrode model, developed by Newman and his colleagues [26-28]. They are composed of a coupled system of ordinary differential equations (ODEs), partial differential equations (PDEs), and algebraic equations to describe the various processes inside batteries. Nowadays, porous electrodes serve as the major components for commercial LIBs due to their advantages over nonporous counterparts [29, 30]. Porous electrode models are, therefore, widely adopted for battery modeling [11, 31]. Compared to empirical models and ECM, porous electrode models favorably combine the advantages of the physical description of battery performances with a high accuracy attributed to the detailed representation of electrodes' microstructure and electrolyte properties.

Porous electrode models have been used in many publications to illustrate battery-related issues, *i.e.,* battery performance and its influencing factors, battery optimization, mechanism analysis, experimental validation, *etc*. This comprehensive review summarizes the development and applications of the porous electrode model for LIBs. It aims to understand the various critical processes inside LIBs and clarify the remaining challenges for future research. The

structure of this review is organized as follows. The characteristics of porous electrodes and the corresponding porous electrode models are presented in Section 2. Section 3 describes the applications of porous electrode models. These applications include battery performance modeling and optimization, overpotential and impedance modeling, temperature and stress simulations, and battery aging prediction. In addition, model simplifications are also addressed to be applied in advanced battery management systems (BMS). The remaining future challenges of porous electrode modeling are presented in Section 4.

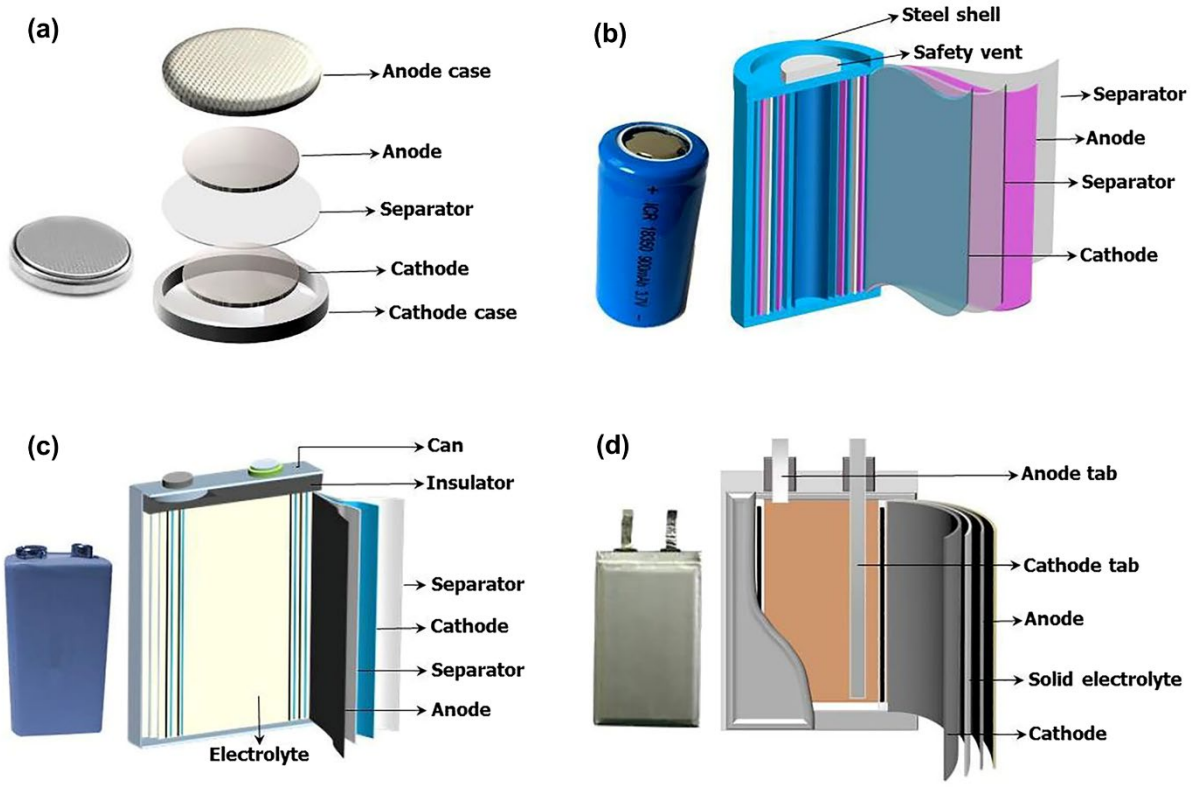

Figure 1. Schematic illustration of typical commercial Li-ion battery configurations: (a) coin, (b) cylindrical, (c) prismatic, and (d) pouch-type cells [32]. Reproduced under the terms of the CC BY 4.0 license [32]. Copyright 2019, the Authors.

2. Porous electrode modeling

Figure 1 shows four types of typical commercial LIBs with coin-type (a), cylindrical (b), prismatic (c), and pouch-type (d) cells. The Li-ion battery structure remains, however, the same and includes a cathode, an anode, a separator, and an electrolyte. Figure 2a shows a cross-sectional view of stacked electrodes and separators of a commercial $LiCoO_2$/graphite cell. The upper composite layer corresponds to the graphite anode. The middle layer shows the separator,

and the bottom layer stands for the $LiCoO_2$ cathode. To guide the eye, Figure 2b shows an artificially colored image of the same battery stack, where the green area represents the graphite particles in the anode, and red corresponds to the $LiCoO_2$ particles in the cathode. Black refers to either the separator between the two electrodes or the voids in both porous electrodes.

A porous electrode is defined as a composite solid containing interconnected void space that constitutes a significant portion of the volume [33]. These void spaces are filled by the liquid electrolyte in a typical Li-ion battery. Electrochemical charge transfer reactions occur at the electrode/electrolyte interface. One of the most important features of porous electrodes is the enlarged interfacial areas, which make the electrochemical behavior of porous electrodes different from that of planar electrodes. The use of porous electrodes also reduces the ionic diffusion pathways within the solid matrix and improves heat dissipation. Those improvements enable LIBs to show higher rate capabilities, and better cycle live performance compared to batteries using nonporous materials [29]. Due to the numerous advantages, using porous electrodes is nowadays a generally accepted strategy for LIBs [29, 34]. Various physical properties, such as porosity, tortuosity, thickness, and specific areas, are essential characteristics for understanding the operation of porous electrodes.

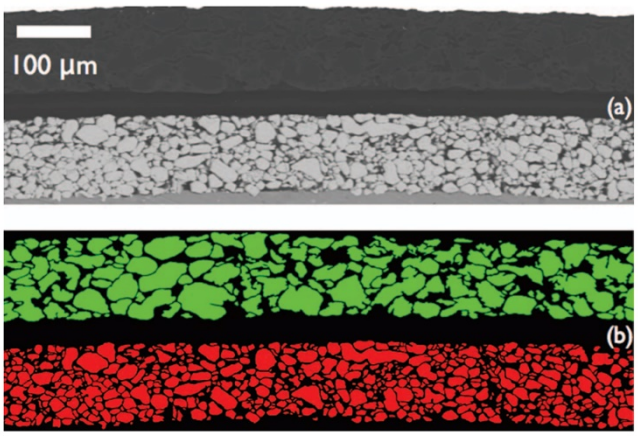

Figure 2. (a) Cross-sectional scanning electron microscope (SEM) view of a commercial $LiCoO_2$/graphite cell, showing the porous anode (top) and cathode (bottom), and separator in between. (b) Artificially colored image of (a) at the same magnification. The green and red colors show the graphite and $LiCoO_2$ particles, respectively. The black background refers to the separator (in the middle), and inert components or void spaces in electrodes [35]. Reproduced with permission [35]. Copyright 2009, IOP Publishing.

Porosity (ε) refers to the percentage of pore volume inside porous electrodes and is one of the most significant engineering factors [36]. Porosity can be considered at the level of the active material or at the level of the electrode. At the active material level, the pore properties are defined by the material microstructures, which are closely related to the synthesis methods and manufacturing conditions. Particle size and particle packing are the most relevant factors at the electrode level. The synthesis method and production conditions of the electrode materials mainly determine the particle size. Particle packing is related to the electrode fabrication process. In commercial battery-grade active materials, the electrode porosity is mainly determined at the electrode level.

Tortuosity (τ) is another parameter that influences the effective transport pathways of ions and electrons inside porous electrodes [30, 37]. The electronic and ionic movements are seriously hindered in highly tortuous electrodes because the pathways wag and bend in various directions. In contrast, porous electrodes with low tortuosity can improve electrolyte penetration and transport kinetics across the electrode thickness significantly [38], thereby improving the electrochemical electrode properties. The fabrication processes of powder-based porous electrodes include slurry preparation, coating, drying, and electrode pressing [34]. All these processes affect the electrode morphology and microstructure, further influencing the porosity and tortuosity of porous electrodes. Finally, external pressure applied to batteries also influences the porosity and tortuosity [39]. Due to the complexity of the microstructure and multiple physical and (electro)chemical phenomena inside porous electrodes, an in-depth understanding of porous electrodes is highly desirable. For this reason, porous electrode models have been developed.

The earliest description of a porous electrode model started in the 1960^{s}. In 1960, Euler and Nonnenmacher [40] related the current distribution in porous electrodes to the macroscopic electrode properties, such as porosity, average surface area per volume, effective conductivity, and double-layer capacity charging per unit volume, assuming a constant concentration and linearized Butler-Volmer relationship. In 1962, Newman and Tobias [41] analyzed the current distribution in porous electrodes with a dilute solution theory. With linear and Tafel simplifications of the Butler-Volmer equation, the analytical equations for current distribution were derived with the assumption of the absence of concentration gradient in the electrolyte. In 1973, Newman and Chapman [42] used a concentrated solution theory to describe the restricted diffusion in a binary electrolyte. They accurately measured the diffusion coefficient in an as-

denoted vertical experimental cell, designed to perform optical measurements of the electrolyte properties.

In 1975, Newman and Tiedemann reviewed the previous investigations and developed a porous electrode theory for battery applications based on a macroscopic description [26]. In this theory, the geometry of a porous electrode was simplified and treated averagely, ignoring the actual geometric pore details. Ionic mass transport in the pores of the porous electrode regions were described by both dilute and concentrated solution theory, considering the electroneutrality condition and pore volume changes during operation. The electric potential distributions in the solid and electrolyte-filled pores were expressed as continuous functions with respect to time and space coordinates. The Butler-Volmer equation described the charge-transfer reactions at the interfacial regions. This theory provided a basic theoretical framework for investigating the physical and electrochemical processes in batteries.

In 1993, Doyle, Fuller, and Newman [27] developed a porous electrode model for a Li anode/polymer electrolyte/porous-insertion-cathode cell with the help of the porous electrode theory. They used the concentrated solution theory for the electrolyte in both the porous electrode and separator region. The active material in the porous electrode was assumed to be spherical particles aligned with the battery thickness direction. Fick's law expressed the Li^+ diffusion limitation inside the spherical particles. In addition, Duhamel's superposition was used to calculate the Li^+ concentration at the particle surface to reduce the computing burden caused by solid-state diffusion. In 1994, Fuller, Doyle, and Newman [28] applied this porous electrode model to a graphite/$LiMn_2O_4$ cell. This model was also proven to successfully fit and predict the performance of a Li-ion battery with two porous insertion electrodes. Since then, the porous electrode model for LIBs has been completed and remained the most popular framework for Li-ion battery modeling up to date., Nowadays, it is usually called a pseudo-two-dimensional (P2D) model [16, 43] or Doyle-Fuller-Newman (DFN) model [44-46].

Figure 3a shows a cross-sectional simplification of a lithium-ion battery with two porous electrodes and a porous separator. In this layout, the active materials in the anode and cathode are simplified to spherical particles with gray and orange colors. The conducting additives are simplified to black small particles. The porosity and tortuosity are also geometrically simplified. Figure 3b shows the corresponding P2D model. The x-dimension represents the macroscale where the mass transfer, electric potential in the solid, and electrolyte are simulated. The r_n and r_p denote the radius of the active particles of negative and positive electrodes. The values of r_n and r_p are in general, not the same but based on the average particle sizes in anode and cathode.

The mass transport inside the negative and positive electrode particles are simulated in r_n and r_p direction, respectively. The governing equations of the P2D model are listed in Table 1, and include several ODEs, PDEs, and algebraic equations. The meaning of symbols is listed in Table 6. Fick's law gives the Li^+ concentration distribution inside the solid particles in spherical coordinates (Equation 3). The Li^+ concentration in the electrolyte at the porous electrode and separator regions are given by Equations 7 and 12 and are based on Fick's laws, considering mass conservation. The electric potential in the solid matrix is given by Equation 9, representing Ohm's law. The electric potential in the electrolyte is given by Equations 8 and 13 for the porous electrode and separator region, respectively, using Ohm's law and Kirchhoff's current law. The charge-transfer reactions occur at the electrode/electrolyte interfaces and are expressed by Butler-Volmer equations (Equations 4-6). The electronic currents are transformed into ionic currents in Equation 11. The battery output voltage is expressed as the electric potential difference between the two current collectors (Equation 14). The relations between the various parameters in the P2D model are summarized in Figure 4.

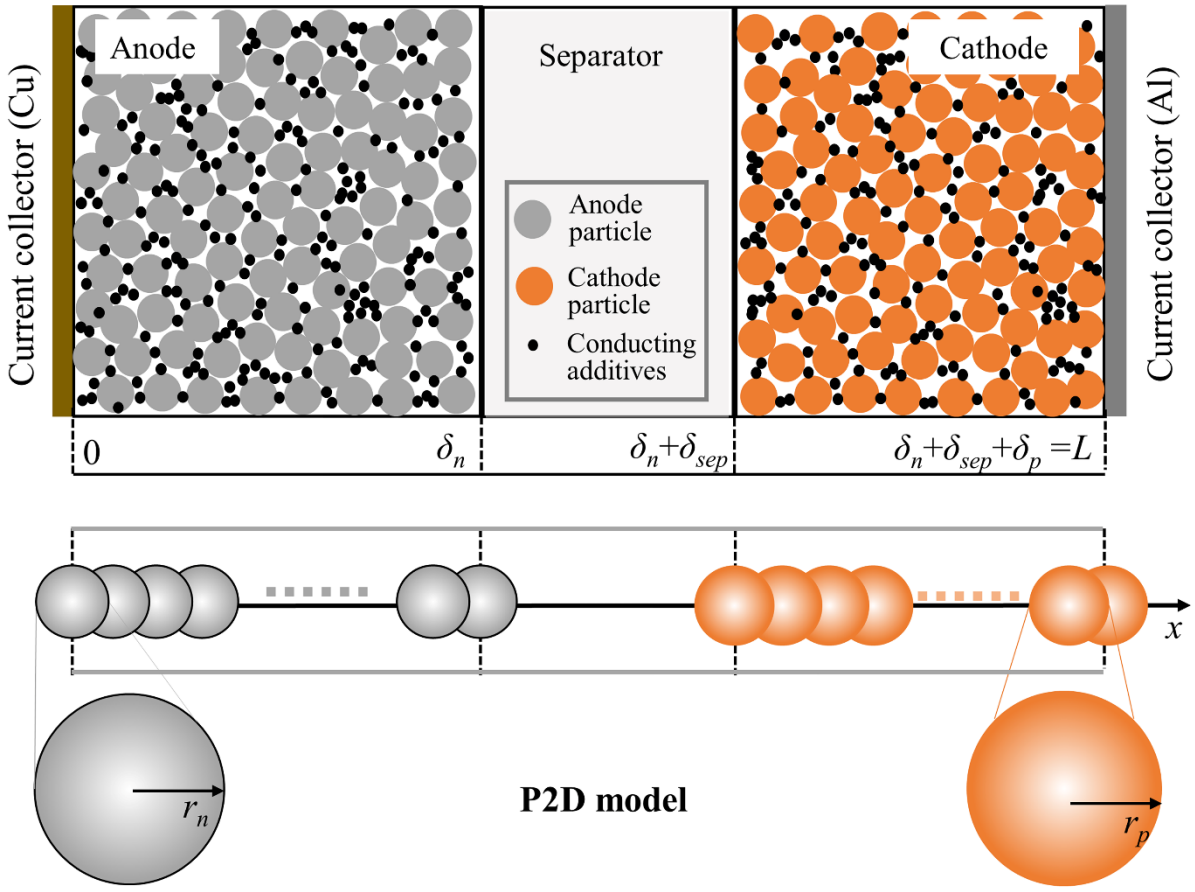

Figure 3. (a) Cross-sectional layout of a lithium-ion battery with two porous electrodes and a porous separator. The active materials in the anode and cathode are simplified to spherical

particles with gray and orange colors. The conducting additives are simplified to black small particles. δ_n, δ_{sep} and δ_p represent the thickness of the negative electrode, separator, and positive electrode, respectively. The total thickness is denoted as L, which is equal to $\delta_n + \delta_{sep} + \delta_p$. (b) Configuration of a corresponding P2D model. The x-direction represents the macroscale axis where the mass transfer, and electric potential in the solid and electrolyte are modeled across the thickness. r_n and r_p denote the microscale of Li-ion mass transfer inside the anode and cathode particles, respectively.

It is worth mentioning that the equations listed in Table 1 are derived based on the concentrated solution theory and porous electrode theory. The exact formulation of the charge-transfer kinetics can vary considerably. For instance, the exchange current density has been related to the Li^+-concentration in the electrode and electrolyte. In that case, concentration-dependent multipliers appear in front of the exponential terms [47-49], as shown in Equations 5b and 6b (Table 1). In a typical P2D model, the electric potential in the electrode and electrolyte is defined as the potential *versus* a Li reference electrode [50]. However, absolute (galvanic) potentials are quite often used in the Nernst-Plank type approach [51, 52], which is the essence of the dilute solution theory [50, 53]. When adopting absolute potentials in a porous electrode model, the $2(RT/F)(1-t_+)$ multiplier in Equations 8 and 13 should be replaced by $(RT/F)(1-2t_+)$ [48, 54].

Due to the complex coupled relations among the equations listed in Table 1, analytical solutions of the system are not available. Numerical solutions are therefore commonly applied. The most common numerical techniques used are Finite-Difference Method (FDM) [55], the Finite-Volume Method (FVM) [56], and Finite-Element Method (FEM) [57]. By these methods, the PDEs are discretized into a system of algebraic equations, including boundary and initial conditions. This system, in turn, can be solved by various methods. The advantages and disadvantages of these three numerical techniques have been reviewed in Ref. [57]. FDM and FVM are simple and accurate and can be applied to regular geometries. FVM performs better than FDM. FDM shows more accuracy with a small number of spatial nodes. FEM can be applied for cases with irregular geometries, unusual boundary conditions, or heterogeneous compositions. These numerical calculations have been implemented in software MATLAB [56, 58], FORTRAN [27, 28], C++ [46], and Python [59], *etc*. Commercial software with porous electrode

model implementation is also available, such as COMSOL, Ansys, AutoLion, and Battery Design Studio (BDS).

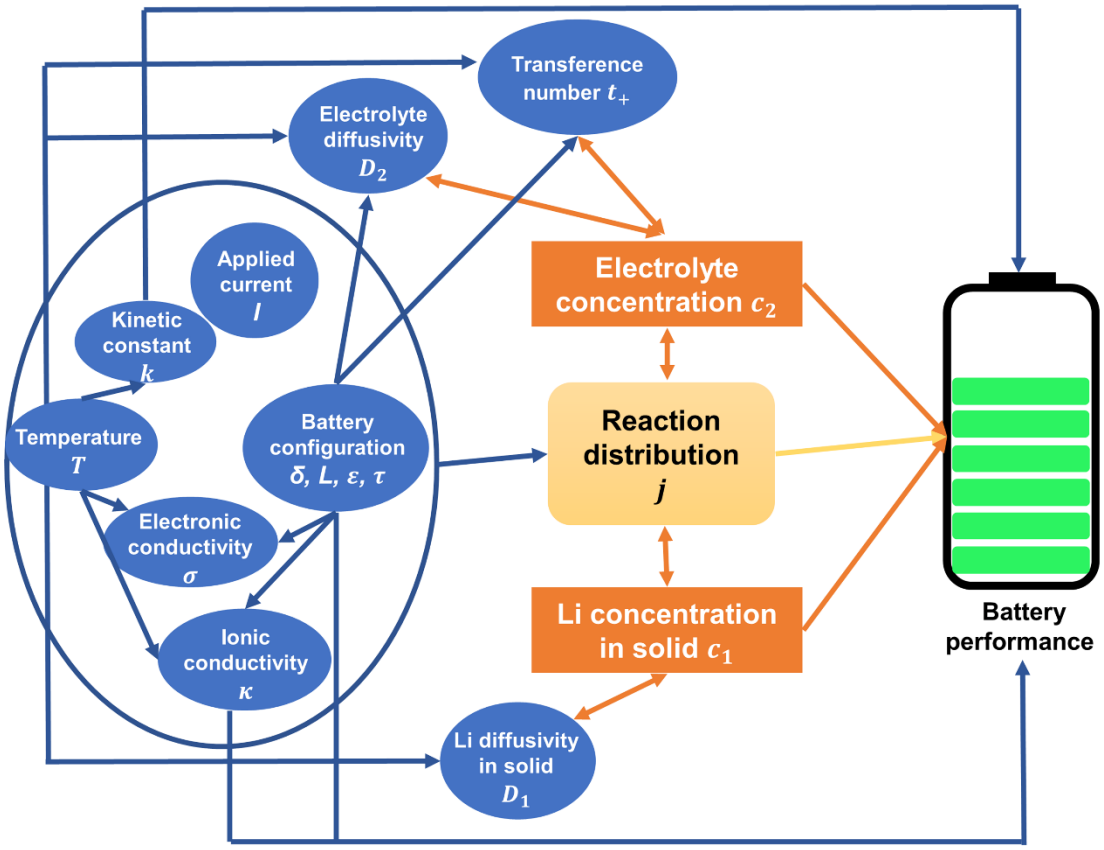

Figure 4. Relations between the various parameters in a P2D model. The one-way arrow represents that the variable at the beginning of the arrow influences the variable at the end of the arrow. The double-sided arrow denotes that the variables at both sides of the arrow influence each other.

Table 1. Governing equations used in a P2D model [27, 28, 60]. The meaning of symbols is listed in Table 6.

	Governing equations	Eq.	Boundary and initial conditions
Porous electrode regions ($m = n, p$)			
Diffusion in particles	$\frac{\partial c_{1,m}}{\partial t} = \frac{1}{r^2}\frac{\partial}{\partial r}\left(r^2 D_{1,m}\frac{\partial c_{1,m}}{\partial r}\right)$	3	$-D_{1,m}\frac{\partial c_{1,m}}{\partial r}\Big\|_{r=R_i} = j_m$, $\frac{\partial c_{1,m}}{\partial r}\Big\|_{x=0} = 0$. $c_{1,m}\Big\|_{t=0} = c_{1,m}^0$
	$\eta_{\mathrm{m}}^{ct} = \Phi_1 - \Phi_2 - U_m^s$	4	-
Kinetics	$i_m^{0,a} = Fk_m\left(c_{1,m}^{max} - c_{1,m}^s\right)^{\alpha_m}\left(c_{1,m}^s\right)^{1-\alpha_m}(c_2)^{\alpha_m}$	5a	-
	$i_m^{0,b} = Fk_m\left(c_{1,m}^{max} - \bar{c}_{1,m}\right)^{\alpha_m}\left(\bar{c}_{1,m}\right)^{1-\alpha_m}(\bar{c_2})^{\alpha_m}$	5b	-
	$j_m^a = \frac{i_m^{0,a}}{F}\left[\exp\left(\frac{\alpha_m F\eta_m^{ct}}{RT}\right) - \exp\left(-\frac{(1-\alpha_m)F\eta_m^{ct}}{RT}\right)\right]$.	6a	-
	$j_m^b = \frac{i_m^{0,b}}{F}\left[\frac{c_{1,m}^s}{\bar{c}_{1,m}}\exp\left(\frac{\alpha_m F\eta_m^{ct}}{RT}\right) - \frac{c_{1,m}^{max} - c_{1,m}^s}{c_{1,m}^{max} - \bar{c}_{1,m}}\frac{c_2}{\bar{c_2}}\exp\left(-\frac{(1-\alpha_m)F\eta_m^{ct}}{RT}\right)\right]$	6b	-
Mass balance	$\varepsilon_m\frac{\partial c_2}{\partial t} = \frac{\partial}{\partial x}\left(D_{2,m}^{eff}\frac{\partial c_2}{\partial x}\right) + a_m j_m(1-t_+)$	7	$D_{2,n}^{eff}\frac{\partial c_2}{\partial x}\Big\|_{x=0} = 0$, $D_{2,n}^{eff}\frac{\partial c_2}{\partial x}\Big\|_{x=\delta_n} = D_{2,sep}^{eff}\frac{\partial c_2}{\partial x}\Big\|_{x=\delta_n}$; $D_{2,p}^{eff}\frac{\partial c_2}{\partial x}\Big\|_{x=\delta_n+\delta_{sep}} = D_{2,sep}^{eff}\frac{\partial c_2}{\partial x}\Big\|_{x=\delta_n+\delta_{sep}}$, $D_{2,p}^{eff}\frac{\partial c_2}{\partial x}\Big\|_{x=L} = 0$;
Potential in solution	$i_2 = -\kappa_m^{eff}\frac{\partial\Phi_2}{\partial x} + \frac{2\kappa_m^{eff}RT}{F}(1-t_+)\left(1+\frac{dlnf_\pm}{dlnc_2}\right)\frac{\partial lnc_2}{\partial x}$	8	$i_2\|_{x=0} = 0$, $i_2\|_{x=\delta_n} = I$; $i_2\|_{x=\delta_n+\delta_{sep}} = I$, $i_2\|_{x=L} = 0$;
Potential in solid	$i_1 = -\sigma_m^{eff}\frac{\partial\Phi_1}{\partial x}$	9	$i_1\|_{x=0} = I$, $i_1\|_{x=\delta_n} = 0$; $i_1\|_{x=\delta_n+\delta_{sep}} = 0$, $i_1\|_{x=L} = I$;
	$i_1 + i_2 = I$	10	-
	$a_m j_m = \frac{1}{F}\frac{\partial i_2}{\partial x}$	11	-
Separator region			
Mass balance	$\varepsilon_{sep}\frac{\partial c_2}{\partial t} = \frac{\partial}{\partial x}\left(D_{2,sep}^{eff}\frac{\partial c_2}{\partial x}\right)$	12	See Equation 7
Potential in solution	$i_2 = -\kappa_{sep}^{eff}\frac{\partial\Phi_2}{\partial x} + \frac{2\kappa_{sep}^{eff}RT}{F}(1-t_+)\left(1+\frac{dlnf_\pm}{dlnc_2}\right)\frac{\partial lnc_2}{\partial x}$	13	$i_2 = I$.
Battery output voltage			
	$V_{bat} = \Phi_1\|_{x=L} - \Phi_1\|_{x=0} - IR_f$	14	-

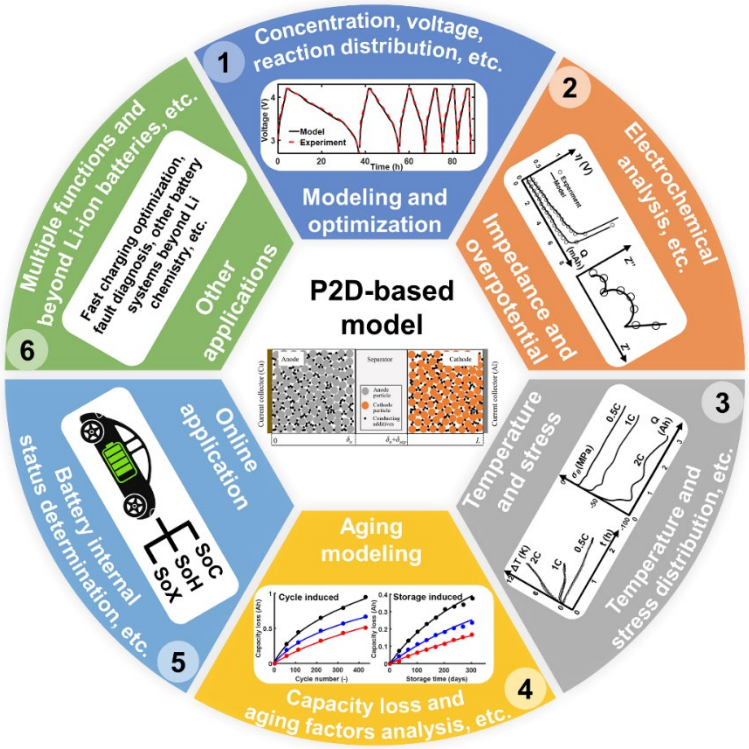

Figure 5. Layout of the applications of P2D models to Li-ion batteries.

3. Applications to Li-ion batteries

P2D-based models have been extensively used in simulations of Li-ion batteries, as schematically shown in Figure 5. In this section, the major applications to Li-ion batteries will be reviewed. Critical issues using P2D models will be introduced in the following subsections, including battery performance modeling and battery optimization, battery overpotential and impedance response modeling, battery temperature and stress modeling, battery aging modeling, battery internal status estimations, and other applications.

3.1 Battery modeling and optimization

Many parameters affect the battery's performance. Some macroscopic parameters can be directly determined by experiments, such as thickness, porosity, *etc*. Most of the material related parameters can be theoretically determined by DFT and MD simulations under thermodynamic equilibrium [9, 10, 17, 61, 62], such as electronic and ionic conductivities, Li diffusion coefficients in the electrolyte and electrodes, equilibrium potential, charge-transfer

reaction constant, *etc*. Note that these kinds of parameters can also be experimentally measured or approximated. Other parameters can only be estimated or optimized, such as Bruggeman coefficient, charge-transfer coefficients, *etc*. All these parameters works as the input for porous electrode models under current applied. The output battery macroscopic characteristics from porous electrode models are of great interest for battery optimized design and use. Note that these macroscopic characteristics cannot be calculated by DFT and MD simulaitons since the special scale problems.

To determine battery macroscopic characteristics under current applied, the main criteria are the deviation between the experimentally observed and simulated battery voltage when the aforementioned parameters serve as the input for porous electrode models. The optimized set of parameters can then be obtained by minimizing the difference between the experimental and simulated voltages. Usually, the Root-Mean-Squared Error (RMSE) between these voltages is minimized. The battery performance and macroscopic characteristics can therefore be critically evaluated using these optimized parameters. For example, the battery output voltage at different C-rates, the Li^+ concentration distribution, the electric potential distribution in the electrolyte, and the electrode reaction rate distribution can be studied. This section reviews the battery macroscopic characteristics and optimization-related issues to improve the battery performance using porous electrode models.

3.1.1 Battery characteristics modeling

3.1.1.1 Li^+-concentration in the electrolyte and electrodes

The active materials frequently used as porous anode in commercial LIBs are graphite-based materials: C_6 (further denoted as C), lithium titanate: $Li_4Ti_5O_{12}$ (LTO), silicon-based materials (Si), *etc*. The active materials often used for porous cathodes include oxides of, for example, lithium manganese ($LiMn_2O_4$), lithium cobalt oxide: $LiCoO_2$ (LCO), lithium nickel-cobalt-manganese oxide: $LiNi_xCo_yMn_{1-x-y}O_2$ (LNCM), lithium nickel-cobalt-aluminum oxide: $LiNi_{0.85}Co_{0.1}Al_{0.05}O_2$ (LNCA), and lithium iron phosphate: $LiFePO_4$ (LFP) [63]. The most popular electrolytes are non-aqueous solutions, in which the lithium hexafluorophosphate ($LiPF_6$) salt is dissolved in a mixture of organic solvents, including various combinations of ethylene carbonate (EC), dimethyl carbonate (DMC), propylene carbonate (PC), diethyl carbonate (DEC), and ethyl methyl carbonate (EMC) [7]. $LiPF_6$ dissolved in these solvents is dissociated into solvated Li^+ and PF_6^- ions, for which the solvation structure depends on the

nature of the solvent. This type of electrolyte is called a binary electrolyte. Various combinations of salts and solvents result in different electrolyte properties, such as viscosity, conductivity, and diffusivity [64, 65]. In addition, electrolyte additives such as, for example, vinylene carbonate (VC) and fluoroethylene carbonate (FEC), are used to increase the stability of the electrolyte in contact with the electrodes.

During operation, Li^+ concentration gradients in both the electrolyte [53, 66, 67] and electrodes [68-72] are developed due to ionic transport limitations. The ionic transport in the electrolyte has been quantitatively described by electrolyte transport characteristics, such as salt diffusion coefficients and transference numbers [50]. These properties are, in turn, influenced by the electrolyte salt concentration and temperature [73-75]. A low temperature and large salt concentration lead to small salt diffusion coefficients and low cation transference numbers, which enlarge the Li^+-concentration gradients in the electrolyte. These two parameters are mathematically related to each other [49, 50, 76]. In addition, other factors, like the applied current density, porosity, convection, *etc.,* also influence the electrolyte concentration distribution.

Two kinds of Li^+-concentration gradients can be considered in the electrodes: microscopically inside individual particles [72] and macroscopically across the electrode thickness [77]. The concentration gradient in a single particle depends on the Li^+ diffusion coefficient in the solid, which is affected by the Li^+-concentration, temperature, and material crystal structure. Li^+ concentration gradients among multiple particles result from the charge-transfer reaction heterogeneity. Generally, reactions occur with higher rates near the separator interface [68-71, 78]. The higher reaction rate at the separator interface makes the Li^+ concentration inside particles at this interface higher than that at the current collector during lithiation. In contrast, Li^+ concentration inside particles at the separator interface will be lower than that at the current collector during delithiation. It is commonly accepted that Li^+ diffusion among particles is very slow. The main Li transport pathways between particles take place via the electrolyte present inside the porous electrodes [79].

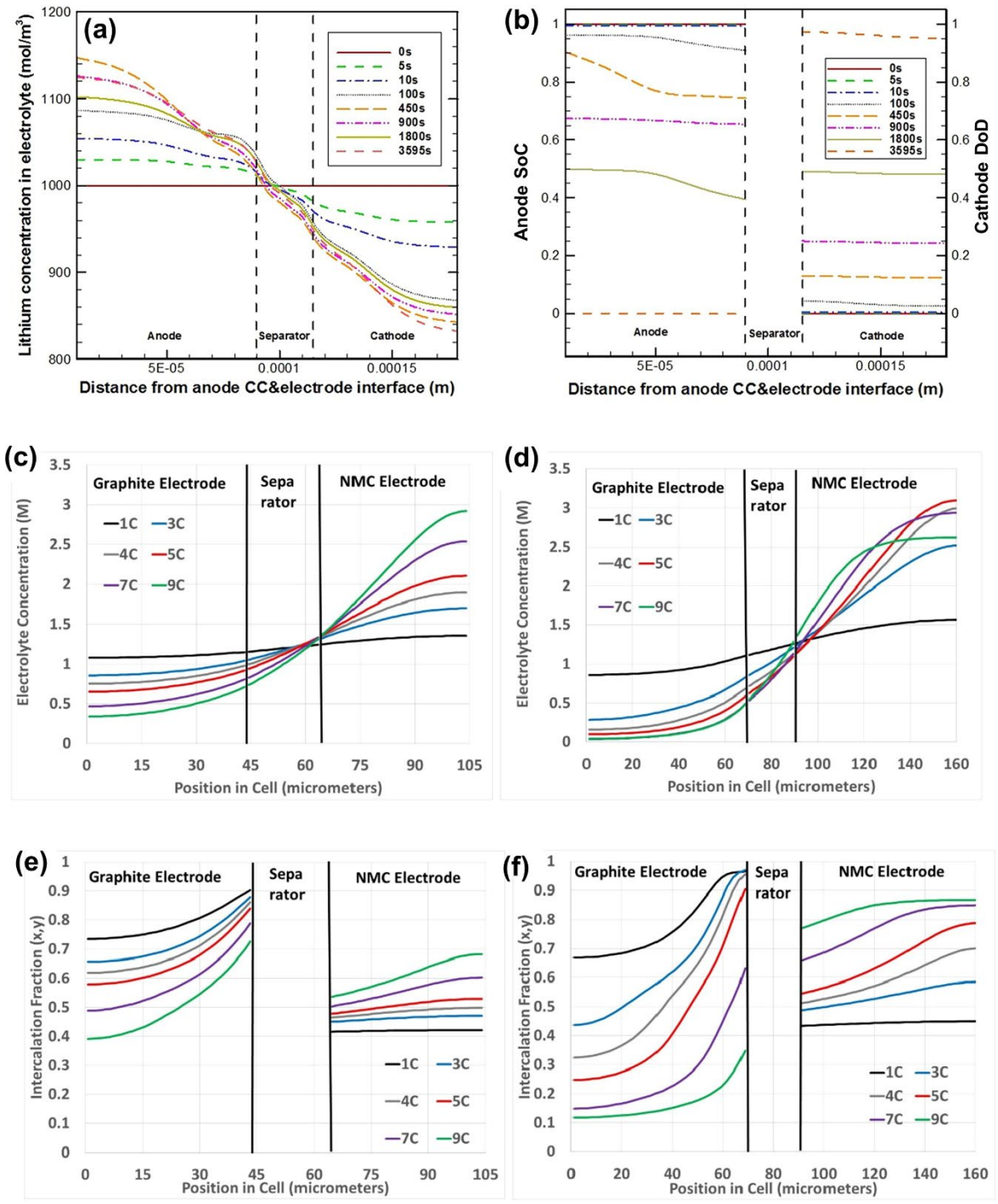

Figure 6. Simulations of (a) the Li^+-concentration gradients in the electrolyte, (b) SoC-distribution in the anode, and DoD-distribution in the cathode [80] during constant current (0.1C) discharging. (c-d) The salt concentration in the electrolyte at the end of charging (4.1 V) under various indicated C-rates for a low (1.5 mAh/cm^2) and a moderate (2.5 mAh/cm^2) mass-loading cell. (e-f) The intercalation fraction at the end of charging under various C-rates for low and moderate mass-loading cells [81]. The intercalation fraction represents the ratio of Li^+ concentration and the maximum available Li^+ concentration in the particle. (a-b) Reproduced

under the terms of the CC BY 4.0 license [80]. Copyright 2016, The Authors. (c-f) Rerroduced with permission [81]. Copyright 2020, Elsevier.

Visualization of the Li^+-concentration distribution inside the electrolyte and electrodes is of great importance for many applications, including the design of optimal functioning porous electrodes and the optimization of efficient charging protocols. P2D-based model simulations have been extensively applied for these purposes [56, 80-91]. For example, Jiang *et al.* [80] simulated the Li^+-concentration in the electrolyte (Figure 6a), and the SoC and depth of discharge (DoD) variations in the anode and cathode (Figure 6b) at various constant current discharge times. It can be observed that Li^+-concentration gradients in the electrolyte evolve quickly after applying the current. The Li^+-concentrations in the delithiated anode region are higher than that in the cathode region under these discharging conditions. Figure 6b shows that the degree of discharging in the anode is relatively non-uniform. In contrast, simulations show that the gradients are relatively uniform in the porous cathode electrode. As revealed in Ref. [92], the various phase transformations of the graphite electrode result in a relatively flat open-circuit voltage (OCV) of the anode, eventually causing nonuniform utilization of active materials and larger nonuniformity in Li^+ concentration inside the electrode.

Similar observations of the Li^+ concentration in the electrolyte and electrodes based on a P2D model has been reported by Torchio [56], Xia [82], Ghalkhani [83], Rahimian [89], and Saw [91]. In these publications, the development of the Li^+ concentration in the electrolyte showed an opposite trend in the cathode and anode region. The Li^+ concentration in the electrode shows a gradient across electrode thickness. This gradient is attributed to the nonuniform reaction rate distribution. At the same time, there is a gradient inside particles in the radial direction. This gradient is as a result of the diffusion inside particles. The concentration differences in both the electrodes and electrolyte were found to be influenced by the transport parameters and applied current.

In addition to dependence on the transport parameters and current, other factors, such as electrode microstructure, thickness, mass-loading density and electrode particle size, influence the Li^+ concentration in the electrolyte and electrodes. Jiang *et al.* [80] investigated the influence of the electrode thickness and particle size through P2D simulations. Thicker electrodes cause a decline in material utilization due to the longer diffusion pathways and lead to larger Li^+-concentration gradients and faster concentration depletion in the electrolyte. At high discharge

currents, the concentration gradients in both the electrodes and electrolytes become larger. The Li concentration gradients inside the electrode increased when larger particle sizes were simulated. Malifarge *et al.* [88] compared the influence of the electrode thickness and porosity on graphite electrodes through P2D-based simulations and experiments. Thick electrodes and small porosities caused larger Li^+ concentration gradients and, consequently, reduced the electrode utilization, especially at high current densities. Large overpotentials are observed under these conditions, impairing electrochemical battery performance.

Colclasure *et al.* [81] explored the electrolyte transport properties and electrode utilization for cells with a low (1.5 mAh/cm^2) and a moderate (2.5 mAh/cm^2) mass-loading electrode. Figure 6c-f shows the salt concentration in the electrolyte and intercalation fraction for the low and moderate mass-loading cells at the end of charging at various C-rates. Note that the intercalation fraction in Figure 6e and f represents the ratio of Li^+ concentration and the maximum available Li^+ concentration in the electrode. This ratio can also be viewed as the electrode utilization across the porous electrode. The low mass-loading cell showed smaller salt concentration gradients across the electrolyte and more uniform electrode utilization at various C-rates, as shown in Figure 6c and e. The moderate mass-loading cell showed larger salt concentration gradients in the electrolyte and more nonuniform electrode utilization, as shown in Figure 6d and f. This is because a moderate mass-loading cell has a thicker electrode, a lower porosity, and a higher tortuosity, leading to a complicated transport pathway in the electrolyte and a nonuniform reaction distribution. At a high charging rate, the moderate mass-loading cell shows a depletion of salt concentration in the graphite electrode region and a low interaction ratio in the graphite electrode, indicating low utilization. The moderate mass-loading cell was also tested and simulated at various temperatures. Operation at high temperatures revealed low concentration gradients and more uniform electrode utilization due to the improved transport and kinetic properties at high temperatures. Moreover, it was reported that the Li^+ concentration in the electrolyte showed striking waves during operations with a graphite-based porous electrode [92]. These waves are generated by the fluctuation of reaction rate distribution inside the porous electrode.

It can therefore be concluded that the Li^+ concentration in the electrolyte at a delithiated electrode is higher than that at a lithiated electrode. The Li^+ concentration at the surface of the electrode particles is higher than that at the center of these particles during lithiation, and the inverse holds during delithiation. Along the direction of the battery thickness, the Li^+ concentration in the electrode near the separator interface is larger than that near the current

collector interface during lithiation. The reverse holds during delithiation. Transport parameters, porous electrode geometry, current, and temperature all influence the Li^+ concentration distribution in both the electrolyte and electrode.

3.1.1.2 Electric potential distribution

Electric potential distribution in the electrolyte and electrodes are other important battery properties. The absolute electric potential has only a theoretical meaning and is not directly measurable. Typically, the electric potential difference *versus* a reference can, however, only be indirectly measured. In the initial definition of the concentrated solution theory [50], the potential in the electrolyte has been defined with respect to an appropriate reference electrode positioned in the electrolyte. The charge-transfer reaction kinetics are also influenced by the electric potential change across the electrode/electrolyte interface, which is determined by the electric potential difference between the electrode and electrolyte.

The electric potential distribution has been simulated using P2D-models as a function of position and time [80, 84, 89, 93, 94]. For applying the P2D model to LIBs, the electric potentials in the electrode and electrolyte are all defined with respect to a Li reference electrode for convenience. The electric potential difference in the electrode is influenced by the (effective) electronic conductivity (Equation 9 in Table 1). The electric potential difference in the electrolyte is a function of the (effective) ionic conductivity and its salt concentration (Equations 8 and 13). The electric potential in the solid phase generally varies only marginally with position but continuously with time [80, 94]. On the other hand, the electric potential distribution in the electrolyte shows a strong dependency on the electrode microstructure, current density distribution, and applied current [93, 95]. It has been demonstrated that a low porosity of the porous electrode leads to larger potential gradients in the electrolyte but has less influence on the electric potential gradients in the electrode. Jiang *et al.* [80] conducted simulations of the electric potential in the electrolyte and electrode for a thin and thick electrode, where the thick electrode showed much larger electrolyte potential gradients. Xu *et al.* [84] simulated the electric potential profiles at the end of galvanostatic discharging with different C-rates and electrode thicknesses. The electric potential was relatively homogeneous across the electrode thickness at different currents for thin electrodes. However, for thick electrodes, the electric potential showed larger gradients at high C-rates. Orikasa *et al.* [95] compared the ionic and electronic potential distribution for high porosity and low porosity electrodes, as shown in Figure 7. It can be seen that the electronic potential distribution is rather pronounced with respect to the porosity. Contrastingly, significant changes in the ionic potential distribution are

observed. Richardson *et al.* [94] used the P2D-model to simulate the electric potential at high C rates. The results showed that the electric potential in the electrode continuously varied with time while the electric potential in the electrode approached steady-state rapidly.

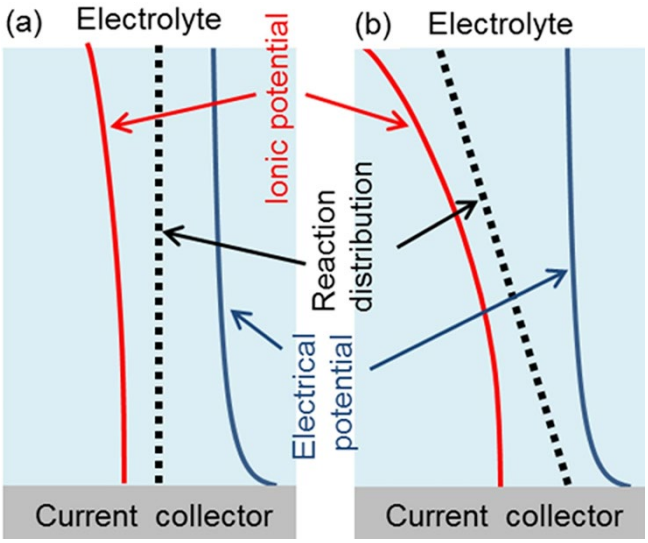

Figure 7. Ionic (red curves) and electric (blue curves) potential distribution for (a) a high and (b) low porosity electrode [95], where the bottom of this figure represents the current collector interface, and the top the separator/electrode interface. The dashed lines show the reaction distribution inside the electrodes. Reproduced under the terms of the CC BY 4.0 license [95]. Copyright 2016, The Authors.

3.1.1.3 Reaction rate distribution

The active materials and conducting additives constitute the electronically conductive network of porous electrodes in LIBs. The charge-transfer reaction takes place at the interface of the active material and electrolyte. However, due to the geometry, (micro)structure, physical and electrochemical properties of the porous electrodes and electrolyte, the charge-transfer reaction does not occur uniformly across the porous electrodes. The distribution of the charge-transfer reaction along the electrode thickness is usually found to be non-uniform and is often denoted as reaction rate distribution. Reaction rate distribution sometimes also refers to the reaction distribution, reaction flux or pore wall flux distribution [26, 27, 96, 97]. Electronic current distribution in the electrode and ionic current distribution in the electrolyte can be easily derived from the reaction rate distribution (Equations 4-6 and 10-11).

The reaction rate distribution is critically important for LIBs. It determines the electrochemical performance, battery overpotential, battery aging, heat, and stress generation. The numerous interrelations make it challenging to investigate the reaction rate distribution. Porous electrode models present an alternative for analyzing the reaction rate distribution in rechargeable batteries [50]. Newman and coworkers [26, 98] proposed four dimensionless ratios to determine the reaction rate distribution across porous electrodes, namely the dimensionless current density (Equation 15), the dimensionless exchange current (Equation 16), the ratio of charge transfer coefficients (Equation 17) and the ratio of effective conductivities in the electrolyte and electrode (Equation 18), according to

$$I_{dless} = \frac{\alpha_a FIL}{RT}\left(\frac{1}{\kappa^{eff}} + \frac{1}{\sigma^{eff}}\right), \tag{15}$$

$$i^0_{dless} = (\alpha_a + \alpha_c)\frac{Fai^0L^2}{RT}\left(\frac{1}{\kappa^{eff}} + \frac{1}{\sigma^{eff}}\right), \tag{16}$$

$$\alpha_a/\alpha_c\,, \tag{17}$$

$$\kappa^{eff}/\sigma^{eff}\,. \tag{18}$$

where I_{dless} or i^0_{dless} are the dimensionless current density and dimensionless exchange current density, α_a and α_c are the anodic and cathodic charge-transfer coefficients, a the specific area of the porous electrode, I the applied current density, L the porous electrode thickness, i^0 the exchange current density, κ^{eff} and σ^{eff} the effective ionic and electronic conductivity. R, T, and F are the gas constant, the temperature in Kelvin, and Faraday's constant, respectively. Note that the "effective conductivity" refers to the actual electronic and ionic pathway in the porous electrodes. When either the value of I_{dless} or i^0_{dless} is large, the reaction rate distribution is not uniform. The ratio of the effective conductivity ($\kappa^{eff}/\sigma^{eff}$) determines where the charge transfer reaction predominantly occurs: at the separator interface, the current collector interface, or simultaneously at both interfaces. However, these four dimensionless ratios are applied under two assumptions. The first can be interpreted as an absence of concentration gradients in the electrolyte and electrodes. The second presumes a constant surface potential. Note that the surface potential refers to the equilibrium potential at the surface of the electrodes.

In the applications to LIBs, these two assumptions usually do not hold. Only at the first moment after switching on the current and assuming that the battery was in equilibrium before, Equations 15-18 can be applied to determine the reaction rate distribution. Further analytical equations can be derived in this specific case. For example, the Tafel approximation [41] has been applied to the Butler-Volmer equation at high overpotentials to derive analytical equations for the reaction rate or current distribution without considering concentration gradients in the solution and electrodes. In Ref. [99], a linear approximation was applied to the Butler-Volmer equation at low overpotentials. A general solution has been written as an inverse Laplace transform. Furthermore, an asymptotical expression for short time intervals was found. Chen *et al.* [100] applied the porous electrode model and analytically derived the reaction rate distribution at short times and low overpotentials. It was interestingly be shown that small values of the effective electronic and ionic conductivity shift the reaction rate from the separator interface to the current collector interface. It was also discovered that an increase of the key parameters above a particular value, called saturation value, would not lead to considerable changes in the reaction rate distribution.

During long-time operation, concentration gradients in the electrolyte and electrodes are developed. The surface potential is not constant anymore and the conclusions based on Equations 15-18 do no longer hold. However, numerical analyses based on the P2D model can still be performed. Wang *et al.* [101] simulated the local current density distribution inside a porous LFP electrode during the operation of a Li/LFP cell. A small electronic conductivity was used in the simulations, leading to a dominant charge transfer reaction near the current collector at the beginning of the current applied. A reaction front formed near the current collector subsequently propagates towards the separator interface. That happened because the particles near the current collector had already reached their fully discharged state, and lithium ions could no longer be inserted. The reaction front moves towards the separator region to satisfy the charge balance condition. Similar behavior was later experimentally confirmed by Rittweger *et al.* [78] and denoted as the ‘intercalation frontier’. Tang *et al.* [97] investigated the influence of the effective electronic and ionic conductivities on the reaction rate distribution by numerical simulations. They demonstrated that the effective electronic and ionic conductivity values strongly influenced the local reaction rate and, consequently, the local current density. Wang *et al*. [96] numerically showed that the intrinsic thermodynamic behavior of the electrode materials, namely the equilibrium potential, also influenced the reaction inhomogeneity. The

slopes in the equilibrium voltage curves mitigated the reaction inhomogeneity. In contrast, the flats parts of the equilibrium voltage curves increased the reaction inhomogeneity.

Chen *et al.* [92] presented a further detailed investigation on the reaction distribution, as shown in Figure 8. They concluded that two factors influence the reaction rate distribution at long-time scales: thermodynamic (Figure 8a) and kinetic (Figure 8b) factors. The kinetic factor refers to the charge-transfer reaction heterogeneity, which causes the nonuniform utilization of porous electrodes. The thermodynamic factor refers to the OCV of the cell. The plateaus of the OCV curve tend to make the electrode utilization even more nonuniform. In contrast, the sloping parts make the electrode utilization more uniform. The voltage transitions from the plateaus to the sloping parts of the OCV curve generate the waves of the reaction distribution. The thermodynamic and kinetic factors are coupled and influence in this way the reaction distribution at longer time scales.

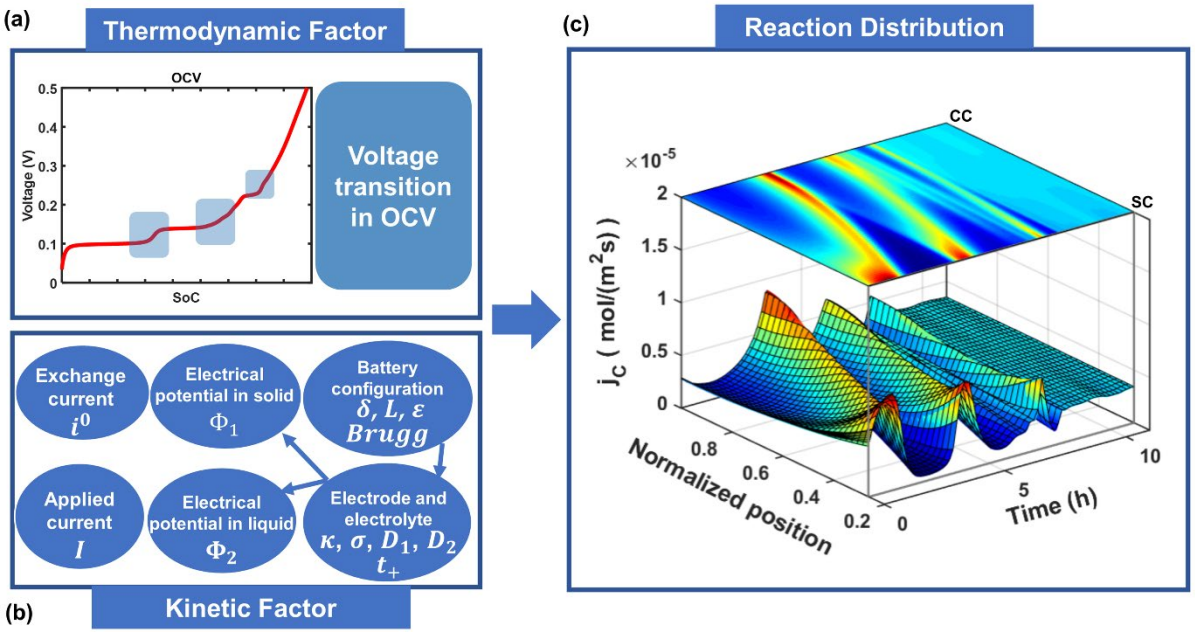

Figure 8. Dependency of the reaction distribution (j_C) on the thermodynamics and kinetics for a graphite-based porous electrode [92]. The thermodynamics refer to the OCV curve (a), and the kinetic factor refers to the charge transfer reaction heterogeneity, which is influenced by a series of kinetic-related parameters (b). (c) j_C as a function of normalized position and time during 0.1C delithiation. The corresponding projected 2D-contour image is shown on top. The planes at the front (SC) and back (CC) indicate the separator and current collector interfaces at normalized position of 0.26 and 1, respectively. Reproduced under the terms of the CC BY 4.0 license [92]. Copyright 2022, the Authors.

3.1.2 Optimization of electrode and electrolyte design

Commercial LIBs operate under various conditions and are often optimally designed for either high-energy or high-power applications. For portable electronics and mobile-phone applications, batteries need to provide as much energy as possible to extend the operation time within a single charge. Batteries need to endure high currents for power tools and reduce the voltage drop to deliver sufficient power. For the recently emerging electric vehicle (EV) market, the batteries must provide both a high-energy and high-power density to ensure a long-time driving range and quick short-time acceleration. In addition, a high-rate capability is also highly needed to meet the fast-charging demands for EVs. However, intrinsic limitations, such as diffusion in the electrolyte and electrodes, ohmic and kinetic resistances [102-104], cause difficulties in achieving the required power and energy density simultaneously. Therefore, it is vital to consider high energy/power demands in different scenarios for battery designs. The important factors that should be considered are electrode compositions, mass-loading density, electrode porosities, current collectors, separators, electrolytes, and connection tags [105].

Due to these multi-influencing factors, a trade-off strategy is usually applied to reach the maximum utilization of batteries in a specific situation. The P2D model can be used to clarify the complicated relationships between the battery performance and various battery parameters [84, 105-110]. Xu *et al.* [84] simulated the effect of the electrode thickness on the battery performance. They showed that the electrode thickness hardly affects the electrode utilization at low C-rates. Thick electrodes significantly reduce, however, the utilization at high C-rates due to the ohmic polarization and the transport limitation in the electrolyte. To maximize the battery energy density at various C-rates, De *et al.* [106] adopted a P2D model to optimize the battery design considering several battery parameters. It was concluded that lower porosities and larger electrode thicknesses were preferred to achieve the maximum energy at low discharge rates. For high C-rates, larger porosities and thinner electrodes were beneficial to reduce the mass transfer limitations within LIBs.

Mei *et al.* [107] investigated the effects of the electrode thickness, the volume fraction of the active material in the electrodes, and particle size on both the energy and power density. It was reported that the increasing electrode thickness and volume fraction of active materials increased the battery energy density but also increased the polarization and, consequently, the heat generation. Small particles helped to increase both the energy and power density. Taleghani *et al.* [108] studied the effects of porosity and multiple particles size distribution on the battery performance by using the P2D model. The maximum specific energy can be

obtained at a porosity of 0.55 while retaining the specific power for the Li/PEO_8-$LiCF_3SO_3$/TiS_2 battery system. Increasing the fraction of small particles increased the cell voltage and decreased the total polarization. That was more pronounced at high C-rates.

Multi-parameter optimization usually causes an enormous computation burden, especially when many battery parameters are used as input. Several approaches have been proposed to reduce the computing time and optimize the battery design under the framework of a P2D model, such as analytical derivations and parallel computation techniques. Wang and Tang [111] developed an efficient analytical model to evaluate the battery performance with different parameter sets. Their simulation results showed a close resemblance to the complete P2D model simulations. Figure 9a and b show the calculated specific capacity (Q_W) of LNCM/Li half-cells and LNCM/C_6 complete batteries as a function of cathode thickness (L_{cat}) and porosity (ε_{cat}). The maximum capacity can be extracted from both the analytical model and the P2D model. For porous electrodes used in a half-cell configuration, the rate performance is better than those used in a complete battery. For a better rate performance of thick electrodes, the adoption of active materials with a flat OCV curve, *i.e.,* $LiFePO_4$ and $Li_4Ti_5O_{12}$, should be avoided. Thermodynamically, this is because flat OCV intensifies the inhomogeneous utilization of active materials so as to decrease the energy and power density. This phenomenon will be even more pronounced at high C-rates.

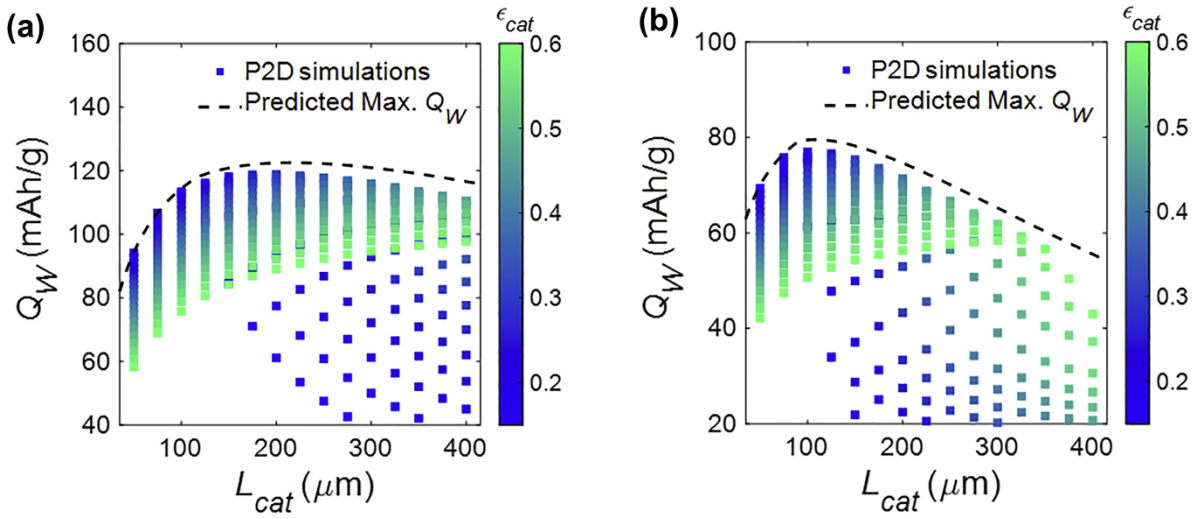

Figure 9. Optimization of (a) LNCM half-cells and (b) LNCM/graphite batteries as a function of the NMC cathode thickness (L_{cat}) and porosity (ε_{cat}) [111]. Squares represent the simulations results and the dashed lines denote the maximum specific capacity (Q_w) calculated by the analytical model. Reproduced under the terms of the CC BY 4.0 license [111]. Copyright 2020, the Authors.

However, other solutions from a kinetic perspective can be made to alleviate these restrictions, such as increasing the porosity and decreasing the electrode particle size to increase mass transport at the porous electrode [108]. Liu *et al.* [112] applied a modified Elitist Non-Dominated Sorting Genetic Algorithm to perform multi-objective and multi-parameter optimization of a complete P2D model. With the help of parallel computing, the computational cost has been significantly reduced. A sensitivity analysis suggested that a thinner electrode and smaller particle size can improve the battery performance. The optimized parameter set also showed a better cycling performance with fewer discharge capacity losses. Hui *et al.* [113] related two optimized electrode parameters (porosity and capacity loading) to the operating conditions and electrode/electrolyte properties. These simulations provided a guideline for manufacturing porous electrodes. They demonstrated that the electrode porosity mainly influenced the battery design at low C-rates. The tortuosity was also found to be an important parameter, influencing the optimized electrode porosity and capacity loading density.

In general, the intrinsic limitations of physical and (electro)chemical processes caused by the active electrode material and electrolyte cannot be avoided. Still, they can be mitigated through optimal battery design. The diffusion limitations in the electrolyte can be reduced by increasing the porosity and decreasing the thickness of the porous electrode. Adapting a novel salt or changing the solvent composition of the electrolyte is also an option [114]. Diffusion limitations in the electrodes can be mitigated by reducing the particle size. Optimizing synthesis conditions or fine-tuning the crystal structure of the material can be helpful [115]. Ohmic resistance limitations can also be reduced by increasing both the electrolyte ionic and electrode electronic conductivity. Surface-coating of the active materials and adding appropriate conducting additives will increase the electrode electronic conductivity further. Adjusting the electrolyte composition will change the electrolyte ionic conductivity [114]. Kinetic limitations can be adjusted by changing the composition of the electrode/electrolyte interfaces. For high-energy batteries, thick electrodes with minor porosity can be adopted. For high-power batteries, thin electrodes with appropriate porosity and small particle size must be considered.

3.1.3 Blending active materials

To optimize the energy/power density and other battery properties, such as thermal and cycling stability, blending two or more active materials into one electrode is a promising approach [116, 117]. For the cathode, various combinations have been applied, such as blends of

spinel ($LiMn_2O_4$) and layered oxides (LCO, LNCM, *etc.*), blends of olivine (LFP, $LiMnPO_4$) and layered oxides [116]. For the anode, graphite (C_6) mixed with silicon (Si) is a frequently used combination [117, 118]. By blending two or more active materials, the merits and disadvantages of the parent materials can be tailored to meet specific application scenarios such as, for example, fast charging by combining graphite with hard carbon [119]; high energy/power density, and lower cost by combining spinel $LiMn_2O_4$ and layered oxides; high energy/power density, and thermal stability by combining olivine LFP and layered oxides [116].

The P2D model can also be applied to simulate blending active materials in a porous electrode [119-124]. The electrochemical performance of each active material in a blended electrode can be separately modeled. Two (or multiple) parameter sets need then to be applied to the several processes in the P2D model. These processes include ionic diffusion inside the active material, charge transfer at the electrode/electrolyte interfaces, *etc*.

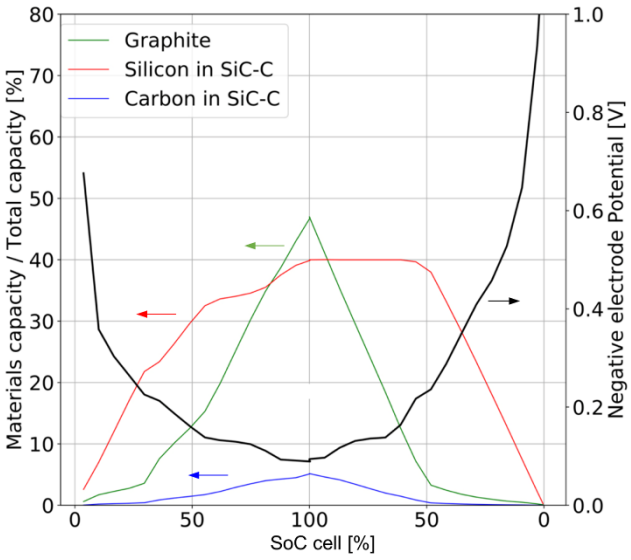

Figure 10. The capacity ratio of Si (red curve), carbon (blue), and graphite (green) in the negative electrode as a function of SoC during charging from 0 to 100% SoC and during discharging from 100 to 0% SoC at 0.05C [121]. The voltage curve is also shown (black). Reproduced with permission [121]. Copyright 2020, IOP Publishing.

Lory *et al.* [121] applied a P2D model to blend electrodes, consisting of a SiC composite and graphite as active material. Note that the SiC composite in this paper is composed of approximately 100 nm silicon flakes embedded in a carbon conducting matrix. Figure 10 shows the capacity ratio of Si, carbon, and graphite in the negative electrode as a function of SoC at

0.05C (dis)charging. A competing reaction among graphite, Si, and carbon in SiC composite was reported. During lithiation, the capacity transferred to Si (red curve in Figure 10) was leading between 0 and 80% SoC. After that, the capacity transferred to graphite (green curve) became more relevant. The capacity transferred to carbon (blue curve) remained small but showed similar behavior as graphite. During delithiation, the opposite occurred as the capacity of Si almost remained unchanged from 100 to 50% SoC, while the capacity of graphite and carbon decreased first. After the carbon and graphite had been fully delithiated, Si took over. This demonstrates that Si dominates the lithiated reaction during the initial stages of charging, followed by that of graphite and carbon. In contrast, Li extraction occurs preferentially at graphite and carbon, followed by that of Si. This behavior has also been observed in experiments [125]. The different (de)lithiation equilibrium potentials of graphite and Si are responsible for these observations. At high C-rates, the SoC range of the dominant Si reaction during lithiation is reduced slightly in line with the offset of the electrode potentials [121].

Chen *et al.* [119] used the P2D model to analyze the fast charging capability of a graphite/hard carbon composite anode. Their simulations confirmed that the improved homogeneity of the reaction current distribution of these composite anodes, enabling significant improvements in fast charging. In addition, they showed that subtle differences in local microstructures influenced the local current density and affected the charging capability. Appian *et al.* [123] simulated the electrochemical performance of Li-ion cells with a mixed $LiMn_2O_4$ - $LiNi_{0.6}Co_{0.2}Mn_{0.2}O_2$ cathode. Pure $LiNi_{0.6}Co_{0.2}Mn_{0.2}O_2$ electrodes combined high specific energy with low specific power and good cycling stability. Pure $LiMn_2O_4$, on the other hand, showed high specific energy and high specific power but suffered from large capacity fading during cycling. Tuning the ratio of $LiMn_2O_4$ and $LiNi_{0.6}Co_{0.2}Mn_{0.2}O_2$ optimized both the electrode-specific energy/power and cycling stability. Dai *et al.* [124] used a P2D model to analyze the stress effects on mixed $LiMn_2O_4$ - $LiNi_{0.8}Co_{0.15}Al_{0.05}O_2$ electrodes. They showed that adding $LiNi_{0.8}Co_{0.15}Al_{0.05}O_2$ to $LiMn_2O_4$ also reduced the stress induced at the end of discharge.

In addition to modeling of electrodes with different kinds of active materials, simulating the same active materials with different particle geometries might also be very useful to further optimize the electrode performance [35, 108, 126, 127]. It was found that small particles are preferred for fast charging as compared to the larger particles [35, 126]. This effect is related to Li diffusion inside electrodes. Large particles have longer diffusion pathways, increasing the concentration

and kinetic polarization. Optimizing the particle size in porous electrodes will help to maximize the energy and power density and fast charging capability [127].

3.2 Overpotential and impedance modeling

Overpotential (η), or overvoltage, is one of the essential characteristics influencing battery performance. The overall overpotential is determined by all physical and (electro)chemical processes occurring inside batteries, including the charge-transfer reactions, transport, adsorption of reactants, desorption, transport of reaction products, electronic conduction, *etc*. These complex processes make it difficult to investigate the overall overpotential and its components. Overpotential simulations based on P2D models are convenient for relating the individual contribution of these processes and provide insights in optimizing the battery design.

Dividing the overpotential by the applied current gives the battery impedance. Measuring impedance responses is useful to characterize the physical and (electro)chemical processes inside batteries. Interpreting impedance responses, therefore, has great significance for understanding these processes and overpotentials. Using P2D-based models has the advantage of physically quantifying the influence of multiple processes on the impedance response. This section reviews the applications of P2D-based models to the overpotential and impedance modeling.

3.2.1 Overpotential modeling

The overpotential is defined as the additional potential needed to drive an electrochemical reaction at a given current [49]. For battery applications, the overpotential is mathematically expressed as the deviation of the battery operating voltage (V_{bat}) from its equilibrium potential (U_{bat}), according to

$$\eta_{bat} = V_{bat} - U_{bat} \,. \tag{19}$$

The overpotential creates an additional increase or decrease in the battery output voltage during charging and discharging, respectively. High overpotentials will reduce the battery

power and energy density and induce intensive heat generation, incurring serious safety hazards [128].

Before reviewing overpotential modeling, the difference between planar electrode overpotential, porous electrode overpotential, and battery overpotential needs to be introduced. Figure 11a shows a schematic illustration of a planar electrode reaction, where the electrochemical reaction distributes only at the surface of this electrode. In this case, electrons act as charge carriers crossing the electrode/electrolyte interface. The overpotential of this planar electrode involves the diffusion overpotential, chemical reaction overpotential, and the charge-transfer overpotential [49, 129]. The diffusion overpotential refers to concentration gradients in the electrolyte between the bulk region and electrode surface. The chemical reaction overpotential results from chemical reactions occurring before or after the charge-transfer reaction. The sum of the diffusion overpotential and chemical reaction overpotential is called concentration overpotential. The charge-transfer overpotential reflects the driving force for the charge carriers crossing the electrode/electrolyte interface. The charge-transfer reaction kinetics strongly depend on the electrode potential. In contrast, chemical reactions depend on the (intermediate) reactant or product concentration [129]. When Li-ions are involved in the charge transfer reactions in LIBs, the electrode composition changes during (de)intercalation. In this case, additional diffusion overpotential inside the electrode needs to be considered, representing concentration differences inside the electrodes. The potential drop across the solid-electrolyte-interface (SEI), formed at the surface of electrodes, also poses an important source of overpotential. This potential drop has recently been recognized as an important property to understand the nature of passivation layers and shed lights on optimizing interfacital engineering for better LIBs [130, 131].

In the case of a porous electrode, the overpotential will be even more complicated. Figure 11b schematically shows a porous electrode in a Li-ion battery, where all the active materials are electronically connected by conducting additives, and the pores are filled with liquid electrolyte. The electrochemical reaction distributes all over the surface of the active materials. The concentration overpotential in the electrolyte, charge-transfer overpotential and diffusion overpotential in the solid exist over the entire active electrode surface. The ohmic overpotential also appears because of the connecting issues among the current collector, active materials, and conducting additives. However, the overall overpotential cannot simply be obtained by adding up all these overpotential components since the electrochemical reactions at different positions inside the porous electrode can be thought of as connected in parallel. Besides, the charge-

transfer reactions distribute heterogeneously across the whole surface areas of the active materials, making it even more complicated to investigate the overpotential.

Battery overpotential, in principle, is the combination of all overpotential components inside this battery, including overpotential from two (porous) electrodes, mass transport overpotentials in the bulk electrolyte and electrodes, as well as ohmic overpotentials in the electrolyte and electrode. The critical point is that the electrode overpotential only reflects the deviation from equilibrium at the electrode/electrolyte interface. In contrast, the battery overpotential reflects all deviations from equilibrium inside the battery, including interface regions and bulk regions in the electrodes and electrolyte.

Adopting porous electrodes in LIBs makes it more challenging to characterize the various battery overpotential components. Using physical-based models is, therefore, helpful in distinguishing various types of battery overpotentials and understanding the overpotential behaviors [47, 53, 132-141]. The P2D model has been adopted to study the various above-described overpotential components [134-142]. These models enable an investigation of the spatial distribution of overpotential components inside porous electrodes and electrolyte regions and give critical insight into the origin of the individual overpotential terms. Chandrasekaran [134] simulated the total overpotential of a 18650-type cell, which was split into salt concentration overpotential, ohmic overpotential, and charger-transfer overpotential. The contributions from various overpotential terms were dependent on the storage capacity (or SoC) and C-rates. The charge-transfer overpotentials in both electrodes were, in general, found to be the dominating factors during discharging. These results were further used in the fast charging analysis for a C_6/liquid electrolyte/LiNCM battery at room temperature [142]. The overpotentials arising from the positive and negative porous electrodes accounted for 36% and 57% of the total overpotential, respectively. The overpotential from the separator region contributed to only 7% of the total overpotential at the end of 2C charging. Reducing overpotentials is critical for cell design and operating condition optimization under various fast charging scenarios.

Srinivasan *et al.*[137] described the overpotential components across a Li/LFP cell using a P2D model. Overpotentials induced by the solution resistance, contact resistance, matrix resistance, charge transfer resistance, and diffusion resistance in the electrode explained the total overpotential drop during battery discharge, as shown in Figure 11c. Note that the contact resistance stands for the resistance between the current collector and the porous electrode. Matrix resistance in this paper refers to the resistance across the porous electrode. Both the contact and so-called matrix resistance played a significant role in the total voltage drop. These

resistances were caused by the electronic and ionic transports in the porous electrodes. The solution resistance and kinetic resistance only played a minor effect. Diffusion resistance appeared to be important at the end of discharge. It was proposed to eliminate the contact resistance by using carbon coatings at both the current collectors and electrode particle surface and adding conducting fillers to the porous electrode. Reducing the electrode particle size was also suggested to facilitate the solid-state ionic transport and reduce the matrix resistance.

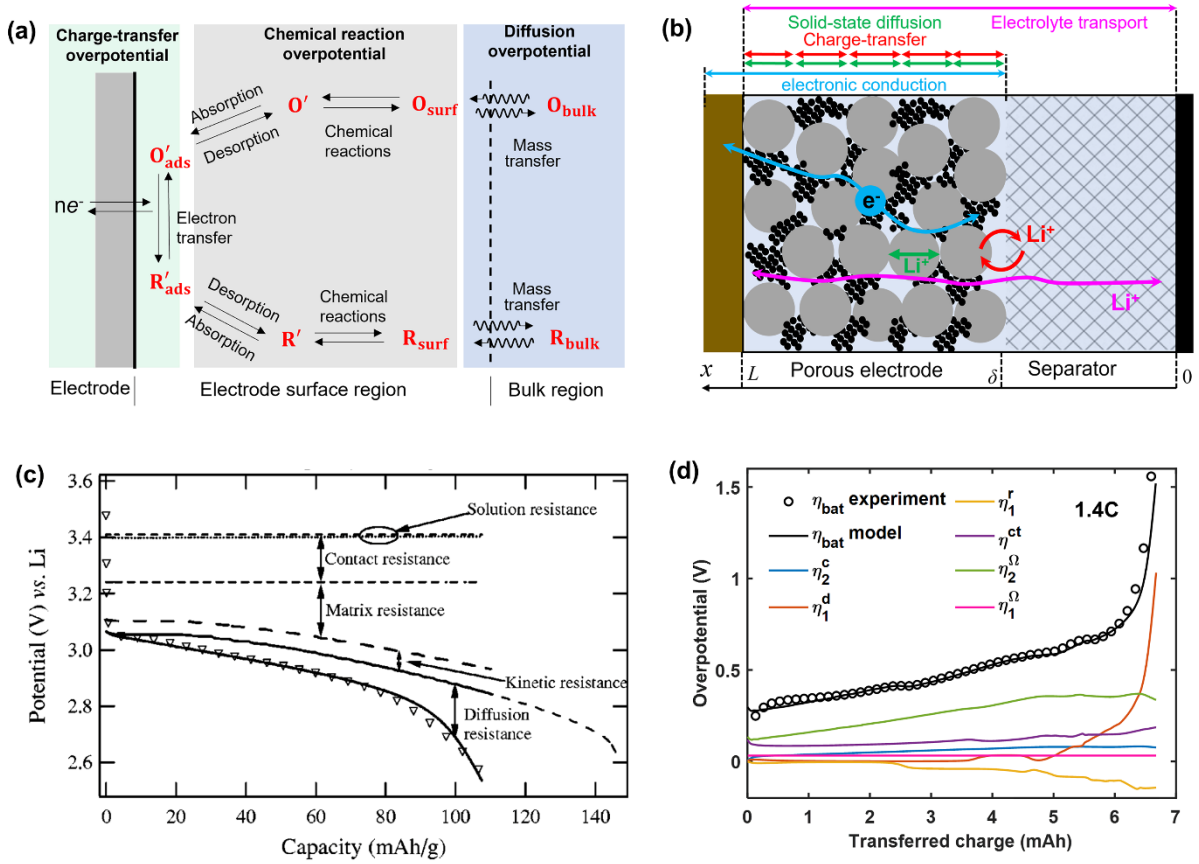

Figure 11. (a) Schematic illustration of a planar electrode reaction, revealing the origin of the various overpotential components [49]. (b) Schematic illustration of a porous electrode reaction in a LIB, indicating multiple electronic and ionic transport processes. (c) Multiple overpotential components across LFP/Li cells using a P2D-model [137]. (d) Overpotential analysis of a graphite-based porous electrode/Li cell during delithiation at 1.4C [141]. The symbols are from measurements, and lines are obtained from simulations. η_{bat} is battery total overpotential. η_2^c represents electrolyte concentration overpotential, η_1^d represents the diffusion induced overpotential in electrode. η_1^r is nonuniform reaction induced overpotential. The summation of $\eta_1^d + \eta_1^r$ represents the Li concentration overpotential in the solid. η^{ct} represents the kinetic overpotential. η_1^Ω and η_2^Ω refer to the ohmic overpotential in the electrode and electrolyte. (a) Reproduced with permission [49]. Copyright 2001, John Wiley and Sons. (c) Reproduced with

permission [137]. Copyright 2001, IOP Publishing. (d) Reproduced under the terms of the CC BY 4.0 license [141]. Copyright 2021, the Authors.

Chen *et al.* [141] considered four overpotential components associated with the Li^+-concentration overpotential in the electrolyte (η_2^c), the Li concentration overpotential in the solid $(\eta_1^d + \eta_1^r)$, the kinetic overpotential (η^{ct}), and the ohmic overpotential $(\eta_1^\Omega + \eta_2^\Omega)$ for a graphite-based porous electrode/Li cell using a P2D model. The simulations are shown in Figure 11d. The electrolyte ohmic overpotential was most dominant, followed by the charge-transfer overpotential. These overpotential components showed fluctuations during operation due to fluctuations of the reaction distribution inside the porous electrode, which further caused the local charge-transfer reaction rate to change and influence the overpotential components.

Quarti and Bessler [140] deconvoluted the total overpotential into ohmic resistance of the current collector and in the electrolyte, the electrolyte concentration overpotential, Li concentrations in the solid electrodes, and activation (charge-transfer) overpotentials for a cell composed of an NCA/LCO blended cathode and a graphite anode. All these overpotential terms showed nonlinear variations with C-rates, SoC, and ambient temperatures. At 20 °C, the overpotential contributions of the cathode were dominant at low C-rates. In contrast, the overpotential contributions corresponding to the anode were dominant at higher C-rates. The ohmic overpotential, related to the current collector and electrolyte, became more important at higher temperatures.

It is worth mentioning that adopting porous electrodes makes it challenging to analyze battery overpotentials due to the heterogeneous and reaction distributions, which leads to dynamic changes in all overpotential components [141]. To reduce the complexity and avoid unnecessary calculations of all overpotential terms, normalized [136] or uniform [138] reaction rate distribution has been applied to the P2D model, where the local reaction rate keeps constant during operation. Battery overpotential analysis is still challenging when the current and reaction rate distribution inside porous electrodes fluctuates during operation.

3.2.2 Impedance response modeling

The impedance is defined as the resistance to the current flow when an alternating-current (AC) signal is applied to the circuit [143]. Impedance is normally a function of the frequency of the AC signal. The set of impedances for all applied frequencies is called the impedance

spectrum. Electrochemical impedance spectroscopy (EIS) has been proven to be a powerful technique for investigating the impedance responses of electrochemical storage reactions. This technique can characterize electrochemical and physical phenomena (ionic transport, solid-phase diffusion, charge-transfer process) occurring inside batteries by investigating the frequency-dependent characteristics. In this technique, a small sinusoidal perturbation is applied to the battery. The resulting response is measured for a set of fixed frequencies. The impedance is calculated according to

$$Z(\omega) = \frac{\eta_{bat}(\omega)}{I(\omega)}, \tag{20}$$

where $Z(\omega)$ denotes the impedance of the processes between the two connecting electrodes, $I(\omega)$ represents the applied current and $\eta_{bat}(\omega)$ the overpotential as a function of frequency. Two types of plots are often used to illustrate impedance spectra [143]. Bode plots show the phase shift and magnitude of the impedance as a function of applied frequency in logarithmic coordinates. Nyquist plots give the real and imaginary parts of the impedance in Cartesian coordinates. Nyquist plots are frequently used for Li-ion batteries to investigate the reaction mechanisms.

After obtaining the impedance spectra, analysis and interpretation need to be performed. Model-based methods are often used. One of the most commonly used models is the equivalent circuit model (ECM). Although an ECM is often rather simple, generic, widely available in commercial software, and provides meaningful analysis, this approach suffers from polysemy, implying that EIS experimental data can be fitted by several different types of ECM [144]. This may lead to uncertain and subjective conclusions.

P2D-based models provide an interesting alternative for EIS modeling and analysis. The original P2D model (Table 1) uses Butler–Volmer charge transfer kinetics to describe a simplified electrode reaction without considering interface effects such as adsorption and the electrochemical double layer, as visualized in Figure 12a. At such a simplified electrode/electrolyte interface, the electric potential of the electrode directly jumps to the electric potential of the electrolyte without any interface charging. Based on the classical concept of the Gouy-Chapman-Stern model, space charges at the electrode/electrolyte interface constitute of electrons at the electrode surface, which are counterbalanced by specifically

adsorbed ionic charges in the inner Helmholtz or Stern plane at the electrolyte side [145]. This charge separation leads to the capacitive behavior of the electrode/electrolyte interface, and the surface potential behaves differently from that of the simplified case (Figure 12b). However, such a detailed electrode interface model makes the description and simulation of the impedance response rather complicated. A simplified electrode interface is therefore often adopted to reduce the complexity and to describe the capacitive behavior. In this approach, the specifically adsorbed charges are ignored. Still, the space charge changes at the electrode/electrolyte interface are considered (Figure 12c). For the electrode surface with SEI formed, this space charge plays an important role in altering the electronic and ionic transport in the interfacial region [130, 131]. As a consequence, an additional equation combining the Faradaic (de)intercalation current and non-faradaic electrical-double-layer current is added to the P2D model [146-149], which replaces Equation 11 in Table 1, according to

$$\frac{\partial i_2}{\partial x} = aFj_i + aC_{dl}\frac{\partial(\Phi_1-\Phi_2)}{\partial t}, \tag{21}$$

where C_{dl} is the electrical double-layer capacitance, and the other symbols have the same meaning as in traditional P2D models, which can be found in Table 6. If both the electrode/SEI film and the SEI film/electrolyte interface are considered, Equation 21 should be modified by considering two electrical double-layer currents [150].

EIS simulations, using P2D-based models, have been implemented in the form of either analytical solutions [145-147, 149-153] or numerical solutions [145, 148, 150, 154, 155]. Several procedures have been applied to obtain analytical solutions. Due to the small amplitude of the input signal, the Butler-Volmer expression has been linearized to reduce the complexity [150-152]. Via Laplace-transform or Fourier-transform techniques [144, 146, 147, 150-152], a system of non-linear differential equations has been derived as a result of conversion from the time- to the frequency domain, which led to the analytical expressions for the impedance. In the numerical solution case, the input signal, for example, sinusoidal current, is supplied to the P2D-based models, , and the output signal, *i.e.*, the resulted overpotential, is calculated numerically. Then the impedance is obtained according to Equation 20. The difference between the analytical solution and the numerical solution is that the analytical solution gives an explicit expression for impedance. In contrast, the numerical solution only gives the numerical result. Both these techniques are based on the porous electrode model.

By both analytical expressions and numerical model responses, EIS data has been investigated. Huang *et al.* [151] developed a full impedance model based on the concentrated solution theory and porous electrode model. Four simplified limiting cases are obtained under several assumptions and approximations. Lateral and cross-sectional inhomogeneities of porous electrodes were also considered. For insertion-type electrode reaction in LIBs (Figure 12d), the EIS characteristics at high frequencies show a cross-point with the real axis, which is due to the ohmic resistance. The semi-circle at the high-to-medium frequencies is due to the charge-transfer reaction coupled with the electrical double layer. Note that a 45° inclining line preceding the semi-circle at high frequencies is due to the distributed charge-transfer reaction impedance throughout the porous electrode [147, 149]. The features at the medium-to-low frequencies are caused by the ionic diffusion in the porous electrodes and electrolyte.

Gruet *et al.* [152] derived an analytical solution for a P2D model of a porous electrode. They studied the dependency of the impedance on SoC and electrode geometrical parameters (Figure 12e-f). The charge-transfer resistance first decreases and subsequently increases with SoC, revealing a minimum at around 50% SoC. Large particle size electrodes increase the charge-transfer resistance and influence the EIS curve in the low-frequency range by enlarging the particle diffusion length (Figure 12e). The electrode porosity also influences the electrolyte ohmic resistance at high frequencies and the ionic diffusion in the electrolyte at low frequencies (Figure 12f). The charge-transfer resistance is also influenced by the electrolyte and binder volume ratio. Optimizing the electrolyte and binder volume ratio leads to the best use of active electrode materials. Kong *et al.* [153] derived a set of closed-form equations for the cell impedance and other electrochemical variables based on a P2D model, including electrolyte concentration, electrolyte potential, solid potential, and solid surface concentration. It was shown that not only the battery voltage showed a phase shift with respect to the sinusoidal input current but also many other electrochemical variables. The closed-form equations exhibited the same output for the impedance as the full-order P2D model with much faster calculations. Cooper *et al.* [156] studied the influence of microstructures on the impedance in porous electrodes. It was shown that the pore shape influenced the impedance in the low and high-frequency ranges.

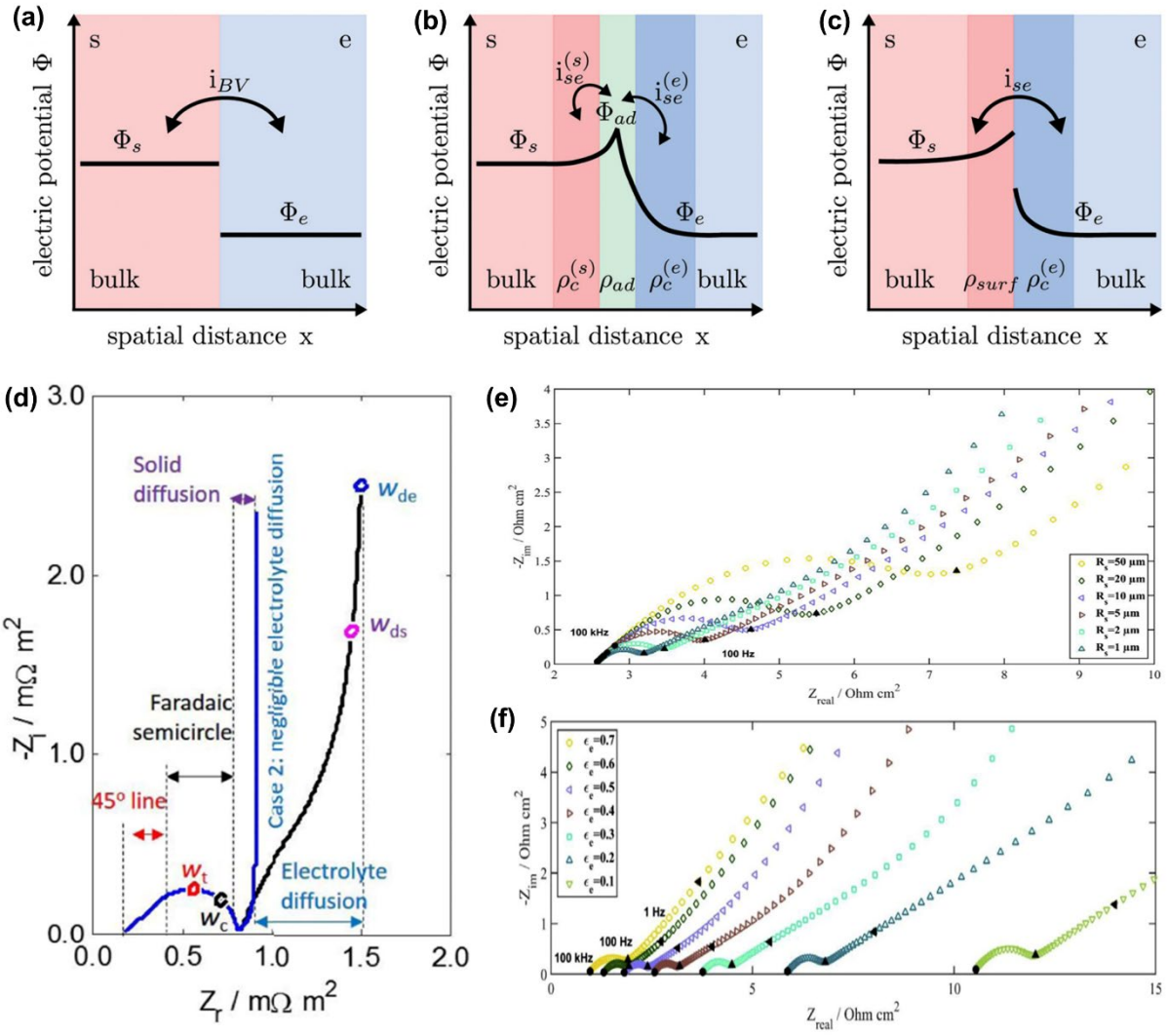

Figure 12. (a-c) Schematic representation of the electrode potential at electrode/electrolyte interfaces [145]. Red areas indicate the electrode region and blue the electrolyte region. (a) The Butler–Volmer approach does not consider charges at the interface. (b) More detailed representation of the electrode/electrolyte interface, considering specifically adsorbed species (green area) and screening counter charges at the surface of the electrode (dark red) and in the electrolyte (dark blue). (c) Reduced electrode/electrolyte interface considering the surface charge in the electrode and screening charge in the electrolyte. (d) Typical examples of impedance spectra for a porous electrode with insertion-type reactions [151]. Impedance simulations of porous graphite electrodes in contact with electrolyte with (e) various particle sizes and (f) electrode porosities [152]. (a-c) Reproduced with permission [145]. Copyright 2019, Royal Society of Chemistry. (d) Reproduced with permission [151]. Copyright 2016, IOP Publishing. (e-f) Reproduced with permission [152]. Copyright 2019, Elsevier.

P2D-based EIS models can not only explain the impedance responses but can also be applied for short-circuit indication, temperature indication, and aging. Kong *et al.* [155] used the impedance response from a P2D-model to detect and predict the internal micro-short-circuits inside lithium-ion cells. The electronic conductivity of the separator was determined as a strong indication for internal short-circuits, which influence the EIS spectra in the low and moderate frequency range. Murbach *et al.* [157, 158] extended the P2D-model to simulate second and third harmonic spectra, allowing them to explore the dependency on the kinetics, mass-transport, and thermodynamic parameters. The second harmonic was sensitive to the charge-transfer coefficient, whereas the EIS results were not. Impedance changes have been used as a method of temperature indication [159], and have also been interpreted by P2D-based impedance modeling [160]. The contribution of various physical parameters, such as ion mobility, electrical double layer capacitance, permittivity, and ionic diffusion coefficient, was analyzed. Impedance measurements have also been used to investigate battery aging [148, 161]. The C-rate and temperature dependence and other physical parameters have been investigated to visualize the relationship between battery aging and impedance variation [148, 159]. With the help of physics-based P2D models, the impact of electrolyte-phase diffusion and solid diffusion was separated. It was concluded that the former played a dominant role in the ageing of LIBs [161].

3.3 Temperature and stress modeling

Temperature and mechanical stress modeling can be performed in conjunction with the electrochemical modeling for LIBs. The overpotentials, simulated by the P2D-model, are essential for calculations of the temperature behavior. Concentration gradients trigger the formation of stress inside active electrode materials and serve as input for mechanical stress modeling. This section will review the temperature and stress simulations coupled with the P2D model.

3.3.1 Temperature modeling

Temperature is a crucial parameter that significantly influences the overall battery performance. All physical and electrochemical processes inside batteries are temperature-dependent. Li diffusion in the electrolyte and electrodes are accelerated at higher temperatures. The charge-transfer reactions are also more facile at high temperatures. Meanwhile, the electronic conductivity is suppressed as the electronic resistance is higher at elevated

temperatures. Lithium plating has to be considered at low temperatures when the kinetics of both Li^+-diffusion and the charge transfer reactions are depressed [162].

The literature considers three types of temperatures [163-165]: the environment, battery surface, and internal battery temperatures. The environmental temperature refers to the ambient temperature of the media surrounding the battery. The surface temperature indicates the temperature at the surface of the battery, and the internal temperature refers to the temperature inside the batteries [164]. When batteries rest for an extended period of time, the surface and internal temperatures will eventually equal to the environmental temperature. However, during battery operation, these temperatures will deviate because of the heat generation, which includes reversible and irreversible heat, as shown in Figure 13a. Reversible heat refers to the entropic heat related to the entropy changes of the (electro)chemical reactions of both battery electrodes. Irreversible heat includes the heat induced by the overpotentials of the various electrochemical reactions and the ohmic effect resulting from the current collectors, porous electrodes, and electrolyte [166].

The internal and surface temperature awareness is vital for optimizing the battery performance and protecting the battery from abuses and hazards. Measurements and simulations are used to monitor the internal and surface temperatures in real-time. Temperature measurements need additional hardware devices, such as thermistors, thermocouples, impedance measurements, and fiber Bragg-grating techniques [128]. A detailed review of temperature-indicating methods can be found elsewhere [128]. Temperature simulations can be easily performed using physics-based models. Combining measurements with simulations provides an accurate and robust method for real-time temperature indication. The following of this section will review the temperature models coupled with P2D-based models.

Table 2. Governing equations in temperature modeling [166, 167]. The meaning of the symbols is listed in Table 6.

	Governing equations	**Eq.**
***m* = *n*, *p*,** where *n* represents the negative electrode, and *p* represents the positive electrode		
Energy conservation	$\rho C_p \frac{\partial T}{\partial t} = \nabla \cdot (\lambda \nabla T) + Q_{re} + Q_{irr}$ Boundary condition $-\lambda \nabla T = -h(T_{amb} - T) - \varepsilon\sigma(T_{amb}^4 - T^4)$	22
Reversible heat	$Q_{re} = aj_m T \frac{\Delta S_m}{n}$	23

	$\Delta S_m = nF\frac{\partial U_m}{\partial T}$	24
Irreversible heat	$Q_{irr} = Q_p + Q_{ohm}$	25
Polarization heat	$Q_p = aj_mF(\Phi_1 - \Phi_2 - U_m)$	26
Total ohmic heat generated in the porous electrode	$Q_{ohm} = Q_e + Q_{s,m} + Q_{cc,m}$	27
Ohmic heat generated in the electrolyte	$Q_e = \kappa_m^{eff}\nabla\Phi_{2,m}\cdot\nabla\Phi_{2,m} + \frac{2RT\kappa_m^{eff}}{F}(t_+ - 1)\left[1 + \frac{\partial lnf}{\partial lnc_2}\right]\cdot\nabla(lnc_2)\cdot\nabla\Phi_{2,m}$	28
Ohmic heat generated in the electrode	$Q_{s,m} = \sigma_m^{eff}\nabla\Phi_{1,m}\cdot\nabla\Phi_{1,m}$	29
Current-collector ohm heat	$Q_{cc,m} = \sigma_{cc,m}\nabla\Phi_{cc,m}\cdot\nabla\Phi_{cc,m}$	30

The energy conservation law has been coupled with a P2D-model to simulate the temperature evolution during battery operation [83, 118, 165-180]. Such coupled models are called electrochemical-thermal (thermal-electrochemical) models. The additional equations are listed in Table 2. The energy conservation law and boundary condition are shown in Equation 22. The reversible heat source is given in Equations 23 and 24, referring to the entropic heat of the electrochemical charge transfer reactions. The irreversible heat sources are given in Equations 25 to 30, including polarization heat, electrode ohmic heat, electrolyte ohmic heat, and current-collector ohmic heat. The reversible and irreversible heat generation can be calculated with the help of the P2D model.

According to the battery geometry and simulation objectives, the energy conservation law can be implemented in zero-dimensional (0D), one-dimensional (1D), two-dimensional (2D), or three-dimensional (3D) configurations. For 0D simulations, the conductive heat transfer is considered to be infinitely fast. Consequently, the whole battery has the same temperature. Temperature changes can directly be related to heat generation and dissipation [118, 165, 175, 176, 181]. The thermal behavior of the battery is closely related to the ambient temperature and applied current. Figure 13b shows the 0D temperature evolution of a commercial cylindrical cell at various C-rates under the ambient temperature of 25 °C. The cell temperature deviates more from the ambient temperature at high C-rates.

For 1D applications, the temperature can be simulated along a single dimension, for example, the radial dimension of a cylindrical cell or the length dimension of a pouch cell. The apparent restrictiveness of such models has led to only a few publications [182]. 2D thermal modeling has been adopted for both cylindrical or pouch-type cells [167, 177, 178, 183]. Its prediction of temperature distribution across batteries is accurate. Figure 13c shows 2D temperature distributions from simulation (left-hand side) and experiment (right-hand side) for a pouch cell at the end of 5C discharging [183]. The simulation matches well with the spatial distribution of the measured surface temperature. It can be seen that the positive tab has a higher temperature than the negative tab due to the higher resistivity of the aluminum current collector at the positive electrode. The cell body adjacent to the tab regions shows the highest temperature. This is because of the higher heat generation and lower heat dissipation in this region. Similar findings are also reported by Zhang *et al.* [178] for pouch-type LIBs.

Nie *et al.* [167] implemented a 2D thermal model into a P2D model for different types of cylindrical cells. It was shown that the highest temperature was located at the center of the cell, and the difference between the internal and surface temperatures increased with the current. For a given C-rate, the temperature at the cell's surface increased as the battery radius increased. Somasundaram *et al.* [177] applied a 2D thermal model to a 18650-type cylindrical cell. They found that the temperature gradient decreased from the center to the cell's surface. They also showed that reversible heat contributed mainly to the temperature rise at low C-rates. In contrast, the ohmic heat was the largest contributor to the temperature at high C-rates. From these 2D simulations of temperatures, optimization of electrode and tab designs is suggested to reduce the heat generation and increase heat dissipation [178]. These studies also benefit the rational design of the cooling system.

A 3D thermal model usually applies to batteries with a pouch or cylindrical shapes. The heat is conducted among the stacked or winded cathode, anode, and separator layers [166, 168, 173, 179, 180]. Saw *et al.* [91] simulated the 3D temperature distribution inside a 18650-type cylindrical cell. The temperature distribution at the end of the 5C charge and discharge is shown in Figure 13d. It can be seen that hot spots are located at the top and bottom of the cell as the larger ohmic heat generation at these two positions. A large temperature gradient exists across the cell in the radial direction. The temperature distribution in an axial direction is relatively uniform. These observations are because the heat generation is confined in the main body of the cell. The heat dissipation in the radial direction is higher than that in the axial direction. Lin *et al.* [179] modeled 3D temperature distribution across the multi-layers of a pouch-type LIB. They indicated that

the strong electrochemical inhomogeneity in the battery stack at high C-rates caused a high local heat generation. The temperature inside the pouch cell is higher than that at the surface. The temperature near the tap region is also higher than in other regions. Mei *et al.* [173] reported that the positive electrode tab exhibits elevated temperature levels compared to that of the negative electrode because of its higher resistance and lower thermal conductivity of the Al current collector. Du *et al.* [166] reported that irreversible heat generation played a dominant role in the battery temperature rise by adopting 3D thermal models. Larger particle sizes increased the irreversible heat generation, as polarization heat played a dominant effect in their investigated batteries.

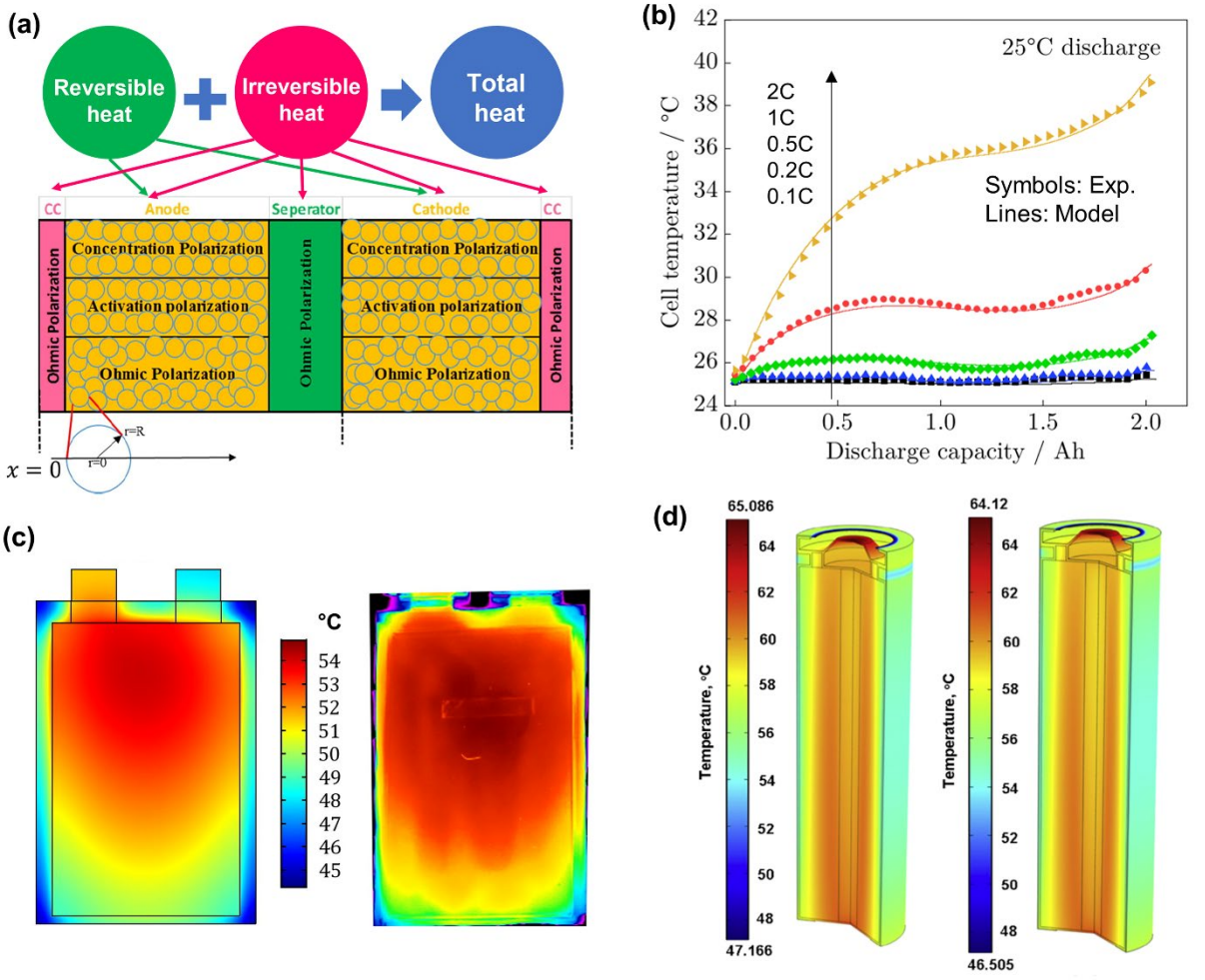

Figure 13. (a) Schematic illustration of the model geometry and the sources of heat generation in LIBs [184]. (b) Modeling (lines) and experimental (symbols) surface temperatures of a cylindrical cell under various C-rates at 25 °C ambient temperature [181]. Due to the slight temperature changes at low C-rates, back and blue lines (symbols), corresponding to 0.1 and 0.2C respectively, almost overlaps in this figure. (c) 2D modeling (left-hand side) and infrared camera measurement (right-hand side) of surface temperature distributions for a pouch-type

cell at the end of 5C discharge [183]. (d) 3D simulation of temperature distribution inside a cylindrical cell at the end of 5C (left-hand side) charge and (right-hand side) discharge [91]. (a) Reproduced with permission [184]. Copyright 2017, Elsevier. (b) Reproduced under the terms of the CC BY 4.0 license [181]. Copyright 2020, the Authors. (c) Reproduced with permission [183]. Copyright 2017, Elsevier. (d) Reproduced with permission [91]. Copyright 2013, Elsevier.

3.3.2 Stress modeling

Li insertion and extraction are usually accompanied by the volumetric changes of the active electrode materials [185, 186] due to lattice changes and phase transformations. During (de)intercalation, Li concentration gradients are built up inside the active electrode particles due to transport limitations, causing strain and stress. This stress is generated at the particle level and has been denoted as diffusion-induced stress (DIS) [187]. For isotropic spherical particles, Li insertion causes concentration gradients along the radial direction. That leads to high concentrations near the surface region (Li-rich) and low concentrations in the core region (Li-poor). Typically, high Li concentrations lead to compression, and low Li concentrations to tension [188]. The difference in Li concentrations results in different internal volume changes, causing radical (σ_r) and tangential (σ_θ) stresses (Figure 14a), along the diameter and perpendicular to the diameter direction, respectively. The stress generated by Li diffusion will, in turn, influence the Li diffusion inside the particles and intercalation kinetics at the particle surface [176, 187-189]. Furthermore, the volume changes of the active electrode particles also cause porosity changes and finally give rise to stress on the cell level because the cell is often enclosed in a rigid housing condition [190].

Table 3. Governing equations in the stress model [176, 189]. The meaning of symbols is listed in Table 6.

	Governing equation	Eq.
Equilibrium of stresses	$\frac{d\sigma_r}{dr}+\frac{2}{r}(\sigma_r-\sigma_\theta)=0$	
	Boundary conditions $\left.\frac{d\sigma_r}{dr}\right\|_{r=0}=0,\quad \sigma_r\|_{r=R_p}=0$	31
Stress-strain relations	$\varepsilon_r=\frac{1}{E}(\sigma_r-2\nu\sigma_\theta)+\frac{\Omega}{3}(c_1-c_1^0)$	32
	$\varepsilon_\theta=\frac{1}{E}(\sigma_\theta-\nu(\sigma_r+\sigma_\theta))+\frac{\Omega}{3}(c_1-c_1^0)$	33

Strain-displacement relations	$\varepsilon_r = \frac{du}{dr},\ \varepsilon_t = \frac{u}{r}$	34
Displacement	$\frac{d^2u}{dr^2} + \frac{2}{r}\cdot\frac{du}{dr} - \frac{2u}{r^2} = \frac{(1+\upsilon)\Omega}{3(1-\upsilon)}\cdot\frac{dc_1}{dr}$	35
Radial stress	$\sigma_r(r) = \frac{2\Omega E}{3(1-\upsilon)}\left[\frac{1}{R_p^3}\int_0^{R_p} c_1 r^2 dr - \frac{1}{r^3}\int_0^{r} c_1 r^2 dr\right]$	36
Tangential stress	$\sigma_t(r) = \frac{\Omega E}{3(1-\upsilon)}\left[\frac{2}{R_p^3}\int_0^{R_p} c_1 r^2 dr + \frac{1}{r^3}\int_0^{r} c_1 r^2 dr - c_1\right]$	37
Hydrostatic stress	$\sigma_h(r) = \frac{\sigma_r(r) + 2\sigma_t(r)}{3}$	38

On a particle level, the DIS is treated analogously to thermal stress [189]. The governing equations in spherical coordinates are listed in Table 3. The stress equilibrium equation and the corresponding boundary conditions are described by Equation 31. The stress-strain and strain-displacement relations are given by Equations 32 and 33, respectively. The differential equation of displacement is given by Equation 34. Solving these equations leads to radial (σ_r in Equation 36) and tangential stress (σ_t in Equation 37), both of which depend on the Li concentration. The hydrostatic stress (σ_h) in a spherical coordinate is given by Equation 38. The Li concentration gradients inside particles are thought to be the driving force for stress in mechanical models. The P2D model can be used to predict the Li concentration distribution inside the electrode particles.

Many studies discuss implementing the stress model in the P2D framework [39, 176, 191-195]. Such models are called electrochemical-mechanical or mechanical-electrochemical models. Figure 14b and c show the radial (σ_r) and tangential (σ_t) stress along the particle radius direction for a graphite particle during 30C delithiation [192]. It can be seen that the stresses are built up rapidly after current application because of the evolution of concentration gradients inside particles. The radial stress σ_r shows the maximum compressive stress at the center of particle and is zero at the particle surface. The tangential stress σ_t shows a maximum compressive stress at the center and a maximum tensile stress at the particle surface. Figure 14d shows the stress at the particle surface across the thickness of the negative electrode at the end of discharging with various C-rates [194]. Obviously, the stress level is higher in the particles near the separator interface (x=0) than in the particles near the current collector interface (x=1). The magnitude of stress within the electrode increases with discharge C-rates. These observations are because the utilization of active materials is nonuniform across the electrode thickness direction. Higher reaction rates take place near the separator interface, causing larger

concentration gradients inside the active materials near this interface, eventually leading to a higher stress level. At high C-rates, higher concentration gradients cause larger stress level. These results indicate that particles near the separator interface have a higher possibility to develop microcracks or fracture. These generated stresses decrease with thinerelectrode thickness, smaller particle size, and larger porosity.

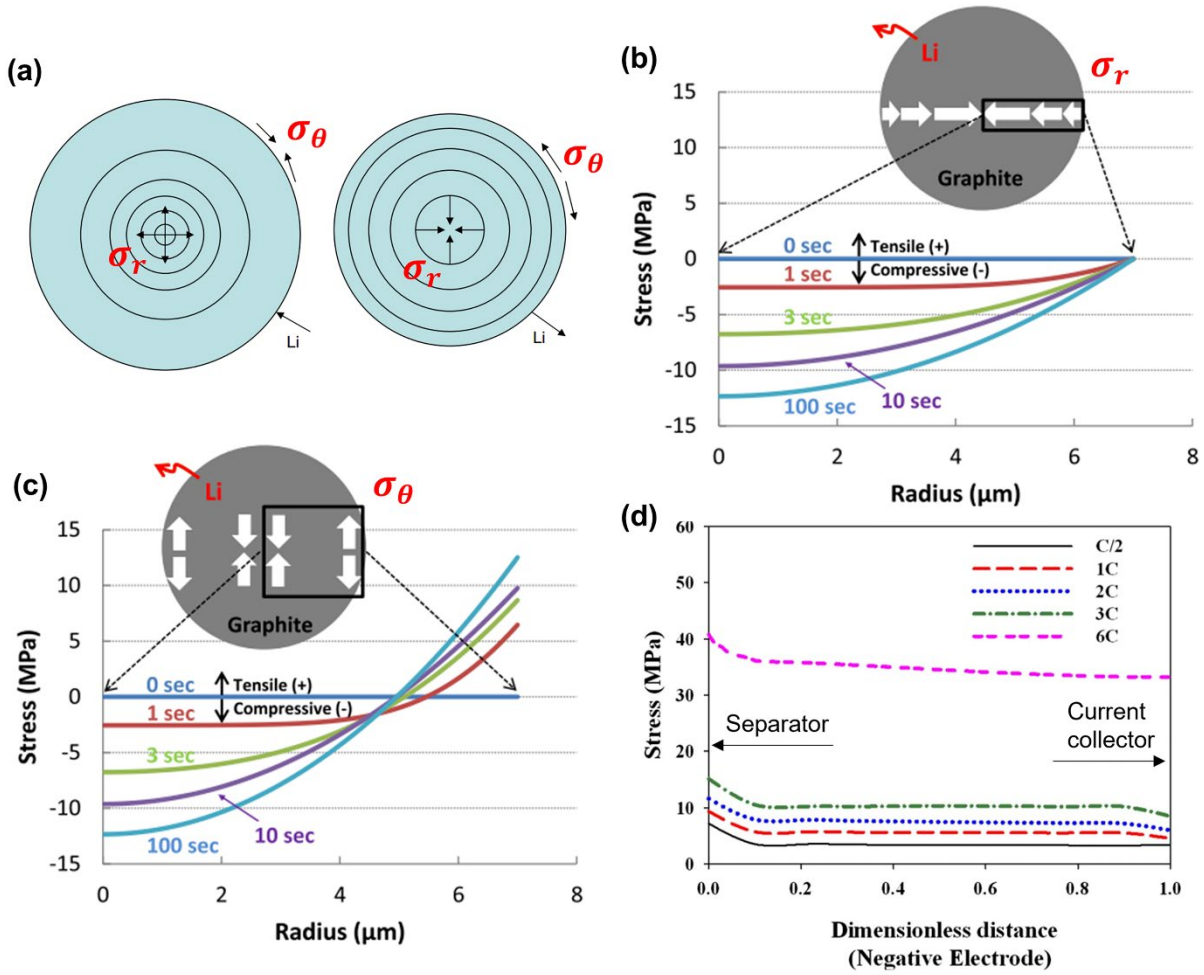

Figure 14. (a) Schematic representation of particle expansion (left-hand side) and contraction (right-hand side) during lithiation and delithiation [196]. The generated radical (σ_r) and tangential (σ_θ) stresses are along the diameter and perpendicular to the diameter directions, respectively. (b-c) The radial (σ_r) and tangential (σ_t) stresses along the particle radius direction for a graphite particle during 30C delithiation [192]. (d) The stress at the particle surface across the thickness of the negative electrode at the end of various discharge C-rates [194]. (a) Reproduced with permission [196]. Copyright 2006, Springer Nature. (b-c) Reproduced under the terms of the CC BY-NC-ND 4.0 license [192]. Copyright 2015, the Authors. (d) Reproduced with permission [194]. Copyright 2009, IOP Publishing.

Ai *et al.* [176] applied a stress model to the P2D model to investigate the stress inhomogeneity in batteries during operation. They also found that the electrode near the separator experienced large tangential stress at the beginning of discharging due to the high local reaction current density in this region. Upon further discharging, a tangential stress peak propagated towards the current collector due to the propagation of the charge transfer reaction current. The electrode at the separator interface clearly experienced nonlinear increased stress at higher C-rates. Contrastingly, the stress at the electrode/current collector interface was found to be less dependent on the applied current. Suthar *et al.* [195] adopted a reformulated P2D model, considering intercalation-induced stress for optimization of charging current. The nonuniform local current distribution significantly influenced both the radial and tangential stress.

In addition, the volume changes of the active electrode particles will influence the porosity and electrode thickness. Garrick *et al.* [197] simulated the porosity and dimensional changes due to the volume changes of active particles. Different battery cases were examined by the stress and strain simulations to provide better insight into the battery design. Rieger *et al.* [190] related the thickness changes of pouch cells to the concentration-dependent volume changes of the particles inside the electrode, which were obtained by coupling the mechanical materials properties with a P2D model. The presented model can predict the cell thickness changes with high accuracy at different C-rates.

Furthermore, thermal and mechanical models can be implemented simultaneously into the electrochemical P2D model [198-200]. Such models can describe the temperature, stress, and electrochemical properties simultaneously.

3.4 Battery aging modeling

Degradation of batteries is related to undesirable (electro)chemical side reactions and mechanical degradation that leads to capacity decline and power fade [201]. Various degradation mechanisms have been proposed and are experimentally validated so far. Figure 15a presents some well-accepted degradation mechanisms [202], including SEI formation at graphite anodes, Li plating, transition metal dissolution from the cathode, active particle cracking, structural disordering, *etc*. Based on the existing aging literature and their impact on the battery

performance, these degradation mechanisms can be classified into two groups: *(i)* loss of Li inventory (LLI) and *(ii)* loss of active materials (LAM) [202-205].

LLI results from side reactions, such as the SEI formation reactions with the electrolyte solvent(s), irreversible Li plating, *etc*. These side reactions electrochemically consume active lithium, which is therefore no longer available for the basic intercalation reactions. It also results in shifting the anode and cathode voltage curves with respect to each other, causing decreases in the output battery voltage upon aging [202, 206]. LAM occurs in both cathodes and anodes due to particle cracking, loss of electrical contact, active site blocking, *etc*. Transition metal dissolution in cathode material also leads to LAM. LAM will cause a shrinking effect on the potential curves of both cathodes and anodes [202]. In this section, the modeling of LLI and LAM coupled with the P2D model is reviewed.

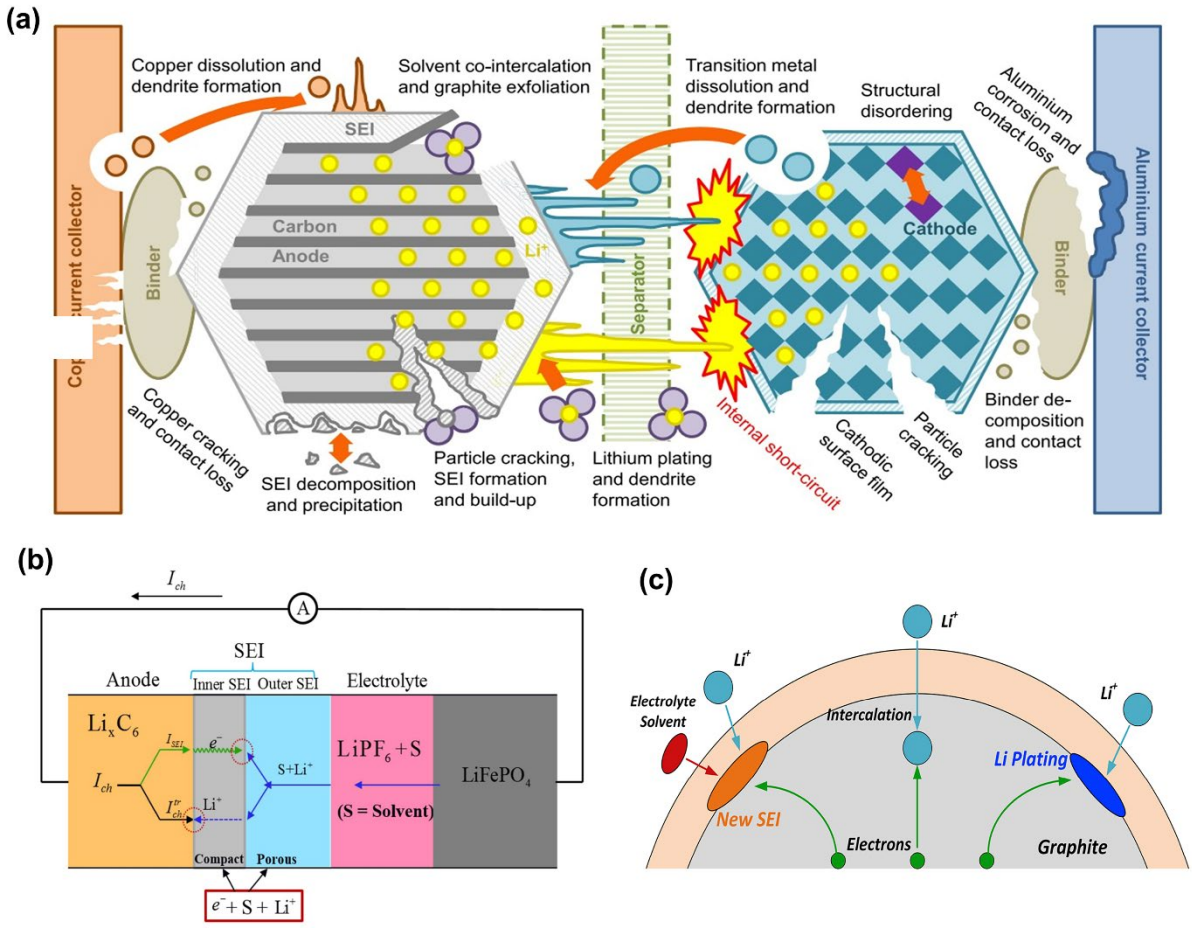

Figure 15. (a) Typical degradation mechanisms in Li-ions batteries using graphite-based anodes [202]. Schematic representation of the SEI formation mechanism by adopting the electron tunneling approach [207]. (c) Li plating and SEI formation mechanism [208]. (a) Reproduced under the terms of the CC BY 4.0 license [202]. Copyright 2017, the Authors. (b) Reproduced under

the terms of the CC BY-NC-ND 4.0 license [207]. Copyright 2015, the Authors. (c) Reproduced with permission [208]. Copyright 2017, Elsevier.

3.4.1 Modeling Li losses

Over the years, Li losses have been considered to be one of the most dominant factors causing battery aging [209, 210]. The time-dependent SEI development and Li plating are the leading processes responsible for these losses [181, 207, 208, 211]. The SEI is a complex film formed at the surface of the anode active materials, such as graphite, silicon, alkali metal, *etc*. It grows extremely fast during the first charging (formation) cycles [212, 213]. The structure of SEI is complex, as schematically shown in Figure 15b. A compact inorganic inner layer is formed at the surface of the active material and is called inner SEI. The inner SEI layer is electronically insulating and ionically conducting, protecting the surface of the anode from solvent molecules penetration but permitting Li-ions transport. A porous, mostly organic, outer SEI layer is formed between the inner SEI and the electrolyte. It allows the transport of both Li-ions and electrolyte solvent molecules (S) [207, 214]. The thickness of the inner SEI is in the range of several nanometers, and the outer SEI is of the order of tens to hundreds of nanometers [207]. Equations 39-41 show possible electrochemical charge transfer reactions involved in the SEI formation. One- or two-electrons transfer reactions have been reported to accompany, for example, the reduction of EC-based electrolytes at graphite-based anodes [214-216]

$$\text{EC-Li}^+ + e^- \rightarrow \text{C}_2\text{H}_4\text{OCO}_2^- + \text{Li}^+ , \tag{39}$$

$$2\text{EC} + 2\text{Li}^+ + 2e^- \rightarrow (\text{CH}_2\text{OCO}_2\text{Li})_2(\text{s}) + \text{C}_2\text{H}_4(\text{g}) , \tag{40}$$

$$\text{EC} + 2\text{Li}^+ + 2e^- \rightarrow \text{Li}_2\text{CO}_3(\text{s}) + \text{C}_2\text{H}_4(\text{g}) . \tag{41}$$

$$\text{Li}^+ + e^- \rightarrow \text{Li} . \tag{42}$$

Electrochemical modeling of the SEI formation at anode surfaces dates back to Peled [217, 218], who considered the transport of electrons through the (inner) SEI and obtained a parabolic rate of SEI growth, as shown in Equation 43a. Later, the electron tunneling mechanism was put forward to describe the possibility of electrons crossing the energy barrier of the insulating inner SEI. The other mention of SEI formation is related to the early works of Broussely *et al.* [219],

as represented by Equation 43b. Broussely assumed that tunneling current declines linearly with the inner SEI layer thickness. The rate of the SEI growth is also parabolic, though the exact expression is different from that of Peled. Diffusion-controlled growth of SEI on planar geometry is also applied and gives rise to a square root relation with respect to time [130]. Subsequent investigations used an analytical solution of the quantum-mechanical tunneling problem to derive an expression for the SEI formation rate [207, 220]. Figure 15b shows an example of electrons hopping through the inner SEI while charging a graphite/LFP cell. Considering electron tunneling as the rate-determining step for the SEI formation, the capacity loss caused by the electron tunneling current was analytically derived [207], according to Equation 43c. The resulting capacity loss model was successfully applied to predict the cycle life of various types of LIBs [207, 221-223].

In an alternative approach, the SEI formed at the surface of the electrode active materials is due to the diffusion of solvent molecules, as shown in Figure 15c. The reaction rate is described by the Butter-Volmer type equations, as shown in Equation 43d. This model was extensively used in describing the SEI evolution due to the convenience of relating the overpotential and solvent concentration [208].

Once a stable SEI is formed, it will protect electrode materials from further severe corrosion and deterioration. However, due to the porous morphology of the outer SEI film, a small amount of electrolyte can still diffuse through the SEI layer and will be reduced at the electrode surface during cycling and storage, leading to a slow but ongoing SEI growth [208]. Following the SEI growth mechanism, the capacity loss exhibits a (nearly) square root dependence on time or output capacity [224-226]. In addition, high temperatures accelerate side reactions, enhancing the SEI formation rate and increasing the capacity loss [227].

Another important source for LLI losses is Li-plating on graphite-based anodes, according to Equation 42. This reaction is initiated by charge-transfer or Li diffusion limitations [81, 228-230]. Under charge-transfer limitations, Li plating occurs as soon as the anode electrode potential becomes close to 0 V *vs*. Li^+/Li. When Li diffusion limitation occurs inside the anode, the Li diffusion rate is lower than the Li intercalation rate of the charge-transfer reaction. Both situations frequently occur when charging at high currents and/or at low temperatures [229, 231]. Li plating may occur even at moderate C-rates and temperatures for aged batteries due to the deteriorated kinetics and active anode material losses [232, 233]. In addition, other factors may lead to Li plating, such as temperature heterogeneity [234], mechanical stress [235], and inhomogeneous current and potential distribution [236].

Li consumption caused by SEI formation is irreversible. It causes permanent capacity losses [213]. However, it was demonstrated that part of plated Li could intercalate back into the active parties during the relaxation and strip into the electrolyte at the subsequent discharging [237, 238], recovering part of the battery capacity, but these recovery processes show a dependence on the battery aging status [233]. In addition, plated Li may react with electrolytes to form new SEI or lose contact with the electrode matrix, causing irreversible losses of the active Li [208]. When the SEI evolution is dominant, the capacity loss was shown to be linear in time or cycle number (except at the beginning). If the dominant factor is Li plating, then the capacity loss has been reported to be nonlinear [232, 233].

Table 4. Governing equations of losses in Li inventory models [208, 217, 219]. The meaning of symbols is listed in Table 6.

	Governing equations	Eq.
Peled (1979) approach [217]	$j_{corr} = \frac{V_{eq}}{\rho\, l_{tot}}$	43a
Broussely (2001) approach [219]	$j_{Br} = \frac{Fk\chi}{l_{tot}}$	43b
Electron tunneling based SEI formation	$j_{tl,C} = \frac{(6+x)\rho_C}{4M_C} \nu_e P_0 \exp\left(-\frac{2l_{tot,C}^{in}\sqrt{2m_e\Delta E_C}}{\hbar}\right)$	43c
Butler-Volmer based SEI formation	$j_{SEI} = -k_{SEI} c_{EC}^{s} F \exp\left[-\frac{\alpha_{c,SEI} F}{RT}\left(\Phi_1 - \Phi_2 - j_{tot} F R_{film} - U_{SEI}\right)\right]$	43d
Li plating	$j_{LP} = -\frac{i_{LP}^0}{F} \exp\left[-\frac{\alpha_{c,LP} F}{RT}\left(\Phi_1 - \Phi_2 - j_{tot} F R_{film}\right)\right]$	44
Film resistance and thickness evolution	$-D_{\mathrm{EC}} \frac{c_{EC}^{s} - c_{EC}^{0}}{\delta_{film}} = -j_{SEI}$	45
	$\frac{\partial c_{SEI}}{\partial t} = -\frac{a j_{SEI}}{2} - \frac{a j_{LP}}{2}\beta$	46
	$\frac{\partial c_{Li}}{\partial t} = -a j_{LP}(1-\beta)$	47
	$\delta_{film} = \frac{1}{a}\left(\frac{c_{SEI} M_{SEI}}{\rho_{SEI}} + \frac{c_{Li} M_{Li}}{\rho_{Li}}\right)$	48
	$R_{film} = \frac{\delta_{film}}{\kappa_{SEI}}$	49
Porosity evolution	$\frac{d\varepsilon}{dt} = -a\frac{d\delta_{film}}{dt}$	50

Aging models based on SEI formation and Li-plating have been integrated into P2D models to simulate the battery capacity losses [181, 208, 211, 239-248]. The additionally required equations are summarized in Table 4. The SEI formation (Equation 43d) and Li-plating (Equation 44) are frequently described by cathodic Tafel expressions in order to reduce the computational complexity of the simulations. The film resistance and thickness evolution are shown in Equations 45-49. The electrolyte porosity change has been described by Equation 50. In Refs. [211, 239-242], the SEI growth is implemented into the framework of a P2D model to simulate battery capacity losses. For example, Frank *et al.* [211] modeled the capacity and power losses during battery cycling and storage. Zhang *et al.* [239] developed a side-reaction aging model based on the P2D framework to simulate the thickness and corresponding resistance of the formed SEI layer upon cycling. These side reactions resulted in significant battery performance degradation. Lamorgese *et al.* [241] simulated the mean SEI film thickness as a function of cycle number and time at various C-rates by integrating the SEI growth model into a P2D-based electrochemical-thermal model. They found that aging influences thermal dissipation due to the increasing SEI thickness. Dhillon *et al.* [242] implemented the SEI growth in a P2D model for a graphite/silicon composite electrode. They found that the SEI growth only played a minor effect on the battery capacity fading.

Both the SEI growth and Li plating are added to the P2D model to investigate the influences on the battery performance [181, 208, 243-249]. Yang *et al.* [208] introduced the SEI growth and Li plating into a P2D model. They simulated the capacity behavior of a graphite/$LiNi_{0.6}Co_{0.2}Mn_{0.2}O_2$ pouch cell and found that it changed from a linear to a nonlinear capacity loss dependency (Figure 16a). The SEI growth caused a linear capacity loss at the early stages of cycling. It preferably was initiated at the surface near the anode/separator interface, resulting in a thicker surface film, larger resistance, and lower electrode porosity near this interface. This situation facilitated Li-plating near the separator interface, causing a nonlinear capacity loss at higher cycle numbers (Figure 16a). Keil *et al.* [181] designed a P2D-based model with SEI formation and Li plating/stripping for 18650-type cylindrical graphite/$LiNi_{0.33}Co_{0.33}Mn_{0.33}O_2$ cells. SEI formation dominated the capacity loss before 500 cycles, and Li plating started after 300 cycles showing an accelerated capacity loss. Irreversible Li plating caused the accelerated (nonlinear) capacity losses (black and blue lines in Figure 16b). If Li was fully stripped after plating, no extra capacity loss would be expected, as shown in the green line in Figure 16b. Yang *et al.* [247] and Liang *et al.* [248] introduced the SEI formation and Li plating into a P2D-based electrochemical-thermal-mechanical model to investigate the

battery cycling performance at various currents and temperatures. The SEI formation was found to be accelerated at high temperatures, as expected. Li plating also led to accelerated capacity losses at low temperatures and large C-rates. Suthar *et al.* [249] investigated the influence of electrode porosity, electrode thickness, and tortuosity on the battery capacity fading. Smaller porosities with larger tortuosities significantly reduced the discharging capacity even for thin electrodes. Applying a porosity gradient increasing from the current-collector interface to the separator interface would help to reduce the capacity fading during battery operation. Müller *et al.* [250] studied the influence of the porosity on the capacity of a graphite-based LIB (Figure 16c) by introducing an aging model into the P2D model. Battery with conventional porosity design showed a linear capacity loss followed by a nonlinear capacity loss. Battery with a linear porosity design increased the porosity linearly from the current collector interface to the separator interface. Battery with two-stage porosity meant the porosity shows two typical values. Both the batteries with linear and two-stage porosities showed extended cycle life because the varied porosity designs can postpone and decrease Li plating.

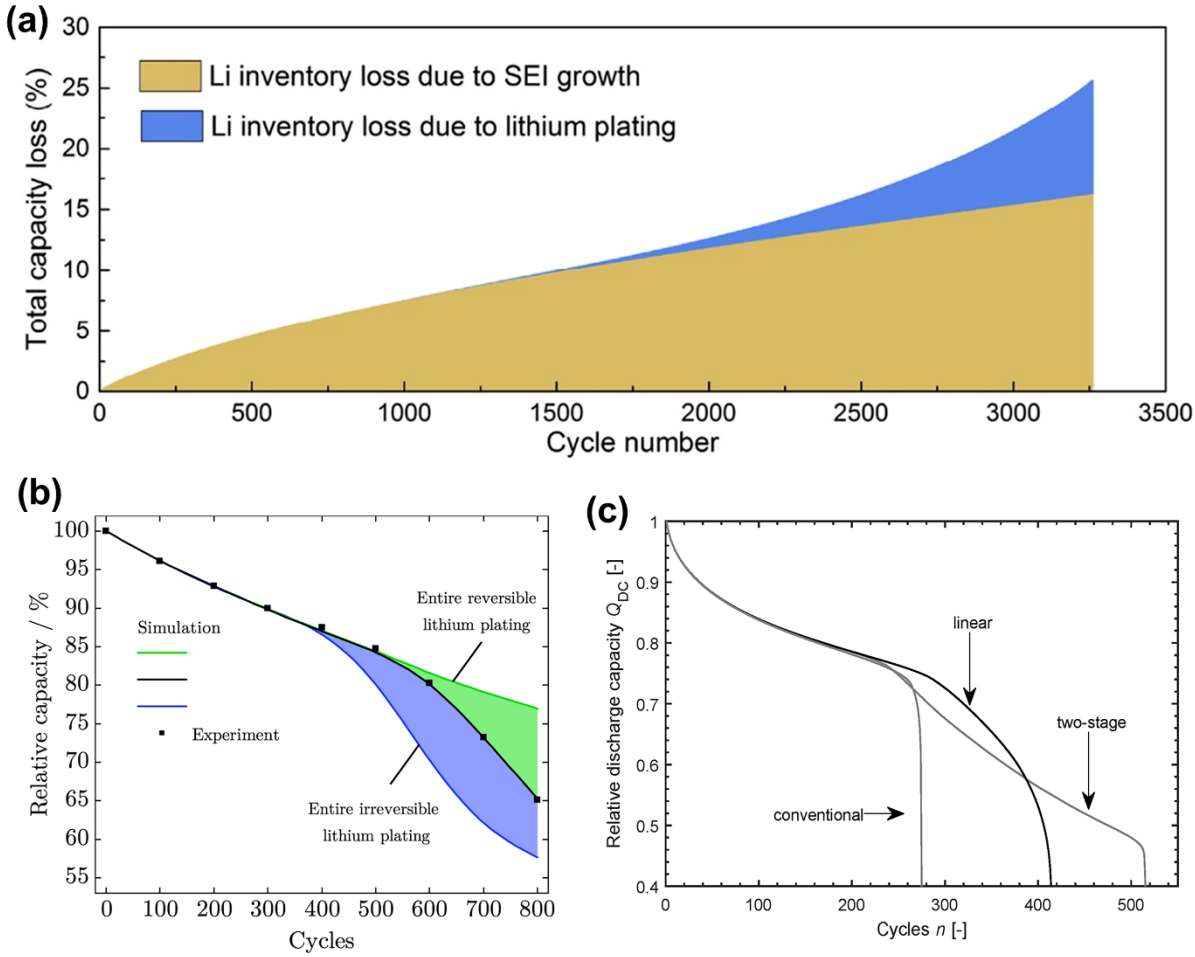

Figure 16. (a) Battery capacity loss caused by SEI formation (brown area) and Li plating (blue area) during long-time cycling [208]. The SEI formation induces a linear capacity loss to nonlinear, while Li-plating causes a nonlinear capacity loss. (b) Nonlinear capacity losses at higher cycle numbers [181]. The symbols represent the experimental, and lines are obtained from simulations. The black line denotes the fit to the experiments. The green and blue lines represent the cases where Li plating is totally reversible and irreversible. (c) Capacity losses with different electrode porosity designs [250]. The lines indicated by "conventional", "linear" and "two-stage" denote the uniform porosity design, porosity gradient, and the design with two typical values of the porosity. (a) Reproduced with permission [208]. Copyright 2017, Elsevier. (b) Reproduced under the terms of the CC BY 4.0 license [181]. Copyright 2020, the Authors. (c) Reproduced under the terms of the CC BY 4.0 license [250]. Copyright 2019, the Authors.

In addition, diffusion-induced stress may cause cracks and crack propagation in the active electrode particles and SEI layers [210, 251]. SEI will subsequently be formed at the newly exposed pristine surfaces, leading to an elevated loss of cyclable lithium. Generally, SEI growth modeling of cracks is performed on a single-particle level [251-253] due to the intense computational load introduced by the complicated crack propagation.

3.4.2 Modeling active material losses

LAM causes irreversible battery capacity and power losses [202], which may occur at both the cathode and anode. Among all degradation mechanisms shown in Figure 15a, two are frequently modeled as leading factors: (*i*) transition metal dissolution from the cathode into the electrolyte [211, 254], followed by the subsequent deposition of the dissolved ions at the anode [223]; *(ii)* particle mechanical fatigue due to DIS and volume expansion/contraction.

Transition metal dissolution from the cathode is considered to be initiated by hydrofluoric (HF) acid. HF can be generated by the decomposition of $LiPF_6$ salt and the reaction with the residual water in the electrolyte [255], according to Equations 51-52. It is reported that the generation of HF is accelerated at a potential above 4.0 V *vs*. Li^+/Li [256].

$$LiPF_6 \rightarrow LiF(s) + PF_5, \quad (51)$$

$$PF_5 + H_2O \rightarrow POF_3 + 2HF. \quad (52)$$

Subsequently, the active cathode material is attacked by HF, and metal ions dissolve into the electrolyte [257]. To reduce the complexity of simulations during cycling, the reaction rate of metal dissolution has been expressed by the anodic branch of the Butler-Volmer relation at positive electrode potentials [211, 254, 258], as shown by Equation 53 in Table 5. When the overpotentials are larger than 0 V, metal dissolution starts. Kindermann *et al.* [211] implemented the metal dissolution mechanism of the cathode in a P2D-based model. It was reported that a non-linear capacity loss was initiated as soon as the LAM of the cathode caused by metal dissolution became more prominent than the LLI caused by SEI formation. Lin *et al.* [258] simulated Mn dissolution from the cathode and subsequent precipitation at the anode, which caused severe degradation of both electrodes.

Table 5. Governing equations for active material loss models [210, 211, 259, 260]. The meaning of symbols is listed in Table 6.

Governing equations		Eq.
Transition metal dissolution	$j_{TMD} = \frac{i_{TMD}^0}{F} \exp\left[\frac{F}{RT}(\Phi_1 - \Phi_2 - U_{TMD})\right]$	53
Mechanical fatigue	$D_1^{cyc} = (1-\xi)D_1$	54
	$E^{cyc} = (1-\xi)E$	55
	$\xi = exp\left(-\beta_1 \frac{d_0}{d}\right)$	56
Influence of LAM	$\frac{\partial \varepsilon_{act}}{\partial t} = \beta \left(\frac{\sigma_{h,max} - \sigma_{h,min}}{\sigma_{yield}}\right)^{\frac{1}{b}}$	57

Mechanical fatigue on the particle level is another factor causing LAM. Particle cracks and interfacial debonding from the conducting matrix are considered two primary degradation mechanisms [261, 262]. Figure 17a and b show examples of particle fracture and interfacial debonding of a cycled NMC electrode. During repeated (dis)charging, active material particles undergo periodic volume shrinking and expansion [185]. DIS inside particles leads to particle crack initiation and crack growth along the pre-existing crack position. In addition, the volume expansion and contraction also cause particle debonding at the particle interface with the binder [263].

Generally, several intrinsic and external factors influence particle cracking [264]. Intrinsic factors include particle size, morphology, composition, structure, defects, mechanical properties, *etc*. Size-dependent fracture has been observed in both cathode [265] and anode active

materials [266, 267] during battery operation. The particle morphology is also important [268]. The DIS inside particles is calculated as a function of sphericity. Fibrous or flake-like particles exhibit reduced stress levels compared to the spherical particles of the same material [268]. In general, alloy-type and conversion-type electrode materials experience larger volume expansion/contraction than the traditional intercalation-type materials [269], leading to a larger possibility of particle crack formation. External factors refer to current, cut-off voltage, thermal conditions, and cycling time [264]. High C-rates, long cycling numbers, and high temperatures usually lead to severe particle cracks. Increasing the upper cut-off voltage for charging and decreasing the lower cut-off voltage for discharging accelerate the crack growth [270].

During repeated (dis)charging, the relentless volume changes of active electrode particles break the weak point of bonding between the active material and binder, causing damage to the conductive matrix. DIS inside the active particles and the adhesion between the particles and binders significantly affect the interfacial debonding behavior [271-273]. Simulations showed that debonding at the interface is initiated at the edge of the contacting area and gradually propagates towards the center of the contacting area [273]. Debonding at the interface is more likely to occur as the particle size and current decrease. That is opposite to the trend of fracturing inside particles, which is more likely to occur at a larger particle size and high currents [263].

Two approaches have been used to simulate the influence of mechanical fatigue on the electrochemical performance of batteries using a P2D model. The first approach is to express the degradation using a decreased Li diffusion coefficient and mechanical properties, as shown in Equations 54-56. A so-called damage factor [259, 260] has been proposed to modify the Li diffusion coefficient in the solid based on mechanical properties, such as stress, strain, stress, and strain energy. It has been suggested that the damage accumulation during cycling significantly contributed to battery capacity fading and mechanical performance loss by suppressing the diffusivity and concentration in the active electrode material. Particles near the current collector showed delays in damage evolution [259]. Figure 17c shows the cell voltage curve by integrating the damage into the Li diffusion in solid. The voltage curve and discharge capacity are obviously depressed (red curve in Figure 17c). Barai and Chen *et al.* [274, 275] showed that the effective diffusivity in the electrode correlated with the microcrack density. They found mechanical damage to the electrode particles near the separator was more dominant in the beginning and subsequently spread across the electrode thickness. After multiple (dis)charge cycles, the damage became more or less uniform. Small particles near the separator interface

and large particles near the current collector interface bored less to mechanical degradation and can help in reducing the capacity fade under driving cycles.

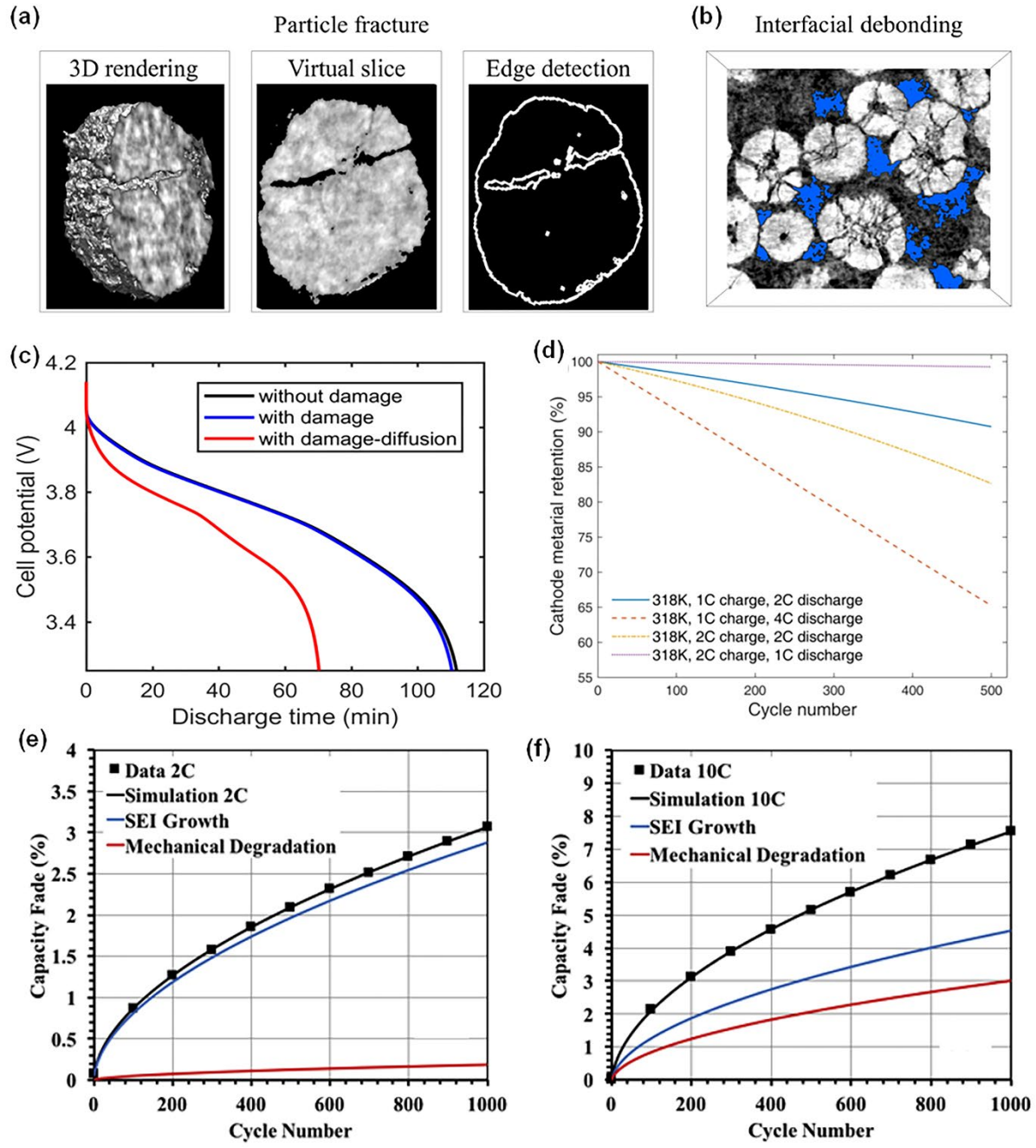

Figure 17. (a) Particle fracture with 3D rendering, central virtual slice, and edge detection of an NMC secondary particle after cycling [261]. (b) Interfacial debonding of active particles from the conductive network [261]. The void regions between the active particles and the conductive network of a cycled NMC cathode (10 cycles at 5C) are indicated in blue. (c) The cell voltage curves without electrode particle damage (black curve) and with damage to the mechanical properties (blue curve) and solid-state diffusion (red curve) [259]. (d) Cathode material loss at

different cycling currents [247]. (e, f) Model-based simulations of the SEI (blue curve) and mechanical degradation (red curve) contributions to the overall capacity fading at 2C and 10C discharge current for $LiFePO_4/C_6$ cells [243]. (a-b) Reproduced with permission [261]. Copyright 2019, Elsevier. (c) Reproduced with permission [259]. Copyright 2017, IOP Publishing. (d) Reproduced with permission [247]. Copyright 2019, Elsevier. (e, f) Reproduced with permission [243]. Copyright 2018, Elsevier.

In another approach, the amount of active material has been reduced due to the particle crack growth and interfacial debonding. Multiple criteria have been proposed to indicate electrode failure under stress [276], including the maximum shear or principal stress, maximum principal strain, and volumetric strain. For active particles, similar criteria also have been implemented. Crawford *et al.* [254] introduced a fatigue criterion by comparing the stress at the particle surface with the yield stress and adopted 20% active material loss after a 4-hour exposure to the yield stress. Reniers *et al.* [210] suggested using the ratio of the maximum hydrostatic stress and yield stress as an indicator for LAM (Equation 57) by fitting to the capacity loss during cycling. Cheng *et al.* [277] indicated that the total strain energy stored in spheres provided the driving force for the fracturing of particles. The total strain energy can be obtained by integrating the strain energy over the entire volume of spherical particles during battery operation. Yang *et al.* [247] and Liang *et al.* [248] used a critical limiting value of the total strain energy to indicate LAM for cathodes and anodes, respectively. In their methods, an active material loss rate was bound together with the total strain energy inside particles. Figure 17d shows the cathode material loss at different cycling currents. More cathode material loss was found at high C-rate charging and discharging as high stress levels are generated inside the electrode particles.

Jin *et al.* [278, 279] implemented the capacity loss by an Arrhenius-type equation of material loss, which is a function of the operation time, temperature, and activation energy. In their approach, both the cycling- and storage-induced LAM nicely fitted the experimental data. Tahmasbi *et al.* [243] predicted the crack area growth within particles by adopting the Paris law. The crack areas were then used to simulate the particle breakage and agglomeration during cycling by making use of a population balance model. The crack growth led to an increased particle surface area during initial degradation, followed by a surface area decrease due to particle agglomeration during the subsequent cycles.

3.4.3 Modeling other factors inducing degradation

Some other factors that lead to battery capacity and power losses are also modeled, such as side reactions at the cathode [258], growth of cathode electrolyte interface (CEI) [280], porosity changes during cycling [242], structural disorder, and structural changes of cathode materials [281], *etc*.

3.4.4 Combined degradation model

Li-ion battery degradation is a complex issue caused by many different degradation processes. Many researchers have combined different degradation mechanisms together to fit and simulate the battery performance based on a P2D model. Figure 17e and f show examples of a combined aging model for $LiFePO_4/C_6$ cells cycling at C-rates, where the SEI formation and mechanical degradation are deconvoluted. The capacity losses caused by SEI growth show dominant roles at all different cycling C-rates. The contributions from mechanical degradation remain small at low C-rates even after longer cycling (Figure 17e). At high C-rate (Figure 17f), the capacity loss caused by mechanical degradation takes an increasing share.

The degradation mechanism of LLI induced by SEI growth and LAM induced by DIS are commonly simulated together [243, 247, 248, 251, 254, 260, 274, 278]. LLI induced by irreversible Li plating [244, 247, 248] and transition metal dissolution [211, 254, 256, 257] is sometimes added to the P2D model. In general, LLI induced by SEI growth dominates the capacity loss under mild cycling conditions [246], at low and moderate C-rate cycling and moderate temperatures. SEI growth causes the battery capacity to decrease linearly with cycles [208] or exhibits a (nearly) square root dependency on time [224]. Both Li plating and LAM will lead to non-linear capacity losses [208, 211] and are reported to be the dominant factors causing capacity losses at low-temperature cycling [247, 248]. The SEI growth, on the other hand, is most dominant at higher temperatures [227, 247].

3.5 Model simplification for advanced Battery Management Systems (BMS)

Due to the high precision and easy access to internal battery states, such as SoC, State-of-Health (SoH), and State-of-Temperature (SoT), P2D models are very suitable for state estimation in advanced BMS applied in, for example, electric vehicles [19, 282, 283]. However, the high complexity of these models causes an enormous computation burden, which limits extensive applications. P2D-model simplification and acceleration are in high demand and have therefore become an essential research topic.

3.5.1 Model simplification and acceleration

The complete P2D model includes numerous PDEs, ODEs, and algebraic equations. After discretization, the total number of parameters increases dramatically [19]. Adding thermal, mechanical, and aging models to the P2D model will increase complexity. Appropriate model simplification is therefore essential for practical applications. Two approaches have been adopted in the literature to reduce the model complexity: optimized calculations and suitable model simplifications.

Several mathematical methods, such as proper orthogonal decomposition [82, 284], Chebyshev orthogonal collocation [25], QR factorization [285], implicit–explicit combined method [286], *etc.*, have been applied to reduce the complexity of the P2D models and increase the calculation efficiency. Xia *et al.* [82] proposed a computationally efficient method to optimize the calculation of the full and reduced P2D model. They combined a proper orthogonal decomposition and a discrete empirical interpolation to reduce the order of the nonlinear algebraic equations. A Gauss-Seidel approach and a damped Newton's method were used to accelerate the convergence speed for the numerical calculation. The proposed method showed a high computation efficiency and sufficient accuracy compared to the full order model. Bermejo *et al.* [286] applied a second-order implicit-explicit Runge-Kutta-Chebyshev scheme to the time discretization of the system of governing equations describing Li concentration in the particle and electrolyte. Their method showed an increased computational efficiency compared to the full-order model. Han *et al.* [86] applied a numerically efficient method to solve the full-order P2D model. In their approach, the Li^+ transport in the particles and electrolyte were only solved once at each time step. The proposed method showed a reduction in the computational cost. It achieved a high accuracy compared with the results from COMSOL Multiphysics.

Simplifying the mathematical model equations is another method to reduce the model complexity [16]. The coupled relations between the various variables, including the Li^+ concentration and electric potential distribution inside the electrodes and electrolyte and reaction rate distribution within the porous electrodes, cause slow convergence in the calculations. To simplify the calculations of the Li^+ concentration inside the electrode particles, many methods have been proposed based on, for example, a second-order or higher-order polynomial approximation [287, 288], a pseudo-steady-state (PSS) approach [289-291], the so-called Padé approximation [292, 293] or using the Galerkin reformulation [294].

For the Li^+ concentration distribution in the electrolyte, other additional approaches have been adopted, including the polynomial approximation [288], the Galerkin method [93], the volume averaging technique [293], and the Padé approximation [295]. Electric potential distributions inside the electrodes and electrolyte are influenced by the reaction rate distribution inside the porous electrodes, which is very complicated due to the highly coupled relations with numerous battery parameters [100, 141]. Proper approximations can reduce the model complexity significantly. Assuming that the charge transfer reactions occur uniformly across the porous electrodes [138, 296-298], this has resulted in a so-called average model (AM). Based on this assumption, the electric potential gradients inside the electrodes and electrolyte can be easily and fast simulated. Furthermore, only using a single particle to represent a porous electrode will significantly reduce the model complexity. Such a model is usually interpreted as a single-particle model (SPM) [43, 299-301], where the distribution of variables across the porous electrode (reaction rate, electric potential, Li^+ electrolyte concentration distributions) are ignored. Consequently, only Li^+ diffusion inside the single particle and the charge transfer kinetics at the particle surface is considered, resulting in even faster calculations. However, these major simplifications lead to poorer voltage accuracies in the simulations at moderate and high currents[16, 302]. Electrolyte dynamics have been added to the SPM to mitigate this drawback [303-305].

3.5.2 Online applications

Both the complete and simplified P2D models have been applied to online state estimations [19, 282, 283, 297, 298, 301, 306-313], such as SoC and SoH. SoC often relates to the mean Li^+ concentration in the positive or negative battery electrode [309]. Based on the applied current, the P2D model or its simplified version can be used to calculate the mean or surface Li^+ concentration of electrode particles, and simulate the SoC and output voltage, respectively. The output voltage can also be experimentally determined by making use of voltage sensors for online applications. State filters are frequently applied to minimize the error between the voltage measurements and simulations.

Examples are Kalman filters (KF) [310], extended Kalman filters (EKF) [297, 298, 307, 311], unscented Kalman filters (UKF) [308], and Luenberger observers [309]. Figure 18a shows an example of a general flowchart of a model-based SoC estimation method, in which the electrochemical models (or ECM) are applied with state filters (or observers) to estimate the

battery SoC and output voltage. Domenico *et al.* [297, 298] simplified the P2D model into an average model. With the help of EKF, they realized a good estimation of the SoC for online applications. Li *et al.* [308] adopted an extended single-particle model (eSPM) with the addition of Li^+ concentration distribution in the electrolyte. They used the Padé approximation to reduce the model complexity further. Through an adaptive UKF, they simulated the Li^+ concentration in the electrode and electrolyte and the battery SoC.

Li *et al.* [311] adopted an SPM, incorporating Li^+ ionic transport in the separator. They added a description of the electrical double layer at the electrode/electrolyte interface to modify the output voltage. This model was further used to estimate the battery SoC with the help of EKF. Figure 18b shows a comparison of their proposed method (EDL-EKF), experimental results, and the Ah method (coulomb counting) for SoC indication. Note that the EDL-EKF represents the proposed method considering an electrical double layer and extended Kalman filter. The Ah method stands for the conventional method using applied current and time. It can be seen their proposed model shows high accuracy even though a large deviation of the initial estimation was found in comparison to the experimental data for the New European Driving Cycle test. Sturm *et al.* [312] used the polynomial approximation or eigenfunction method to simplify the Li^+ concentration inside electrodes using a complete P2D model. Using the EKF estimation method, the simplified model in combination with the eigenfunction method showed fast convergences and low estimation errors.

SoH is an important parameter to indicate the battery aging status and provide lifetime predictions for online applications. Battery aging mechanisms and corresponding aging models have been reviewed in Section 3.4. In this Section, online SoH estimation making use of complete and simplified P2D models will be reviewed. The most commonly used indicators for online SoH assessment are the battery storage capacity and internal resistance [314, 315]. Other indicators, such as solid-state diffusion coefficient, SEI growth, and cyclable Li^+ amount, have also been used [315-317]. By employing P2D-based models and state estimation techniques [318-321], SoH estimation can be accurately performed.

Li *et al.* [301] coupled an SPM with SEI formation and stress-induced crack growth. The reduced complexity of the model and fast computation can be used for fast SoH estimation. Gao *et al.* [318] simplified the P2D model by adopting the Padé approximation for the Li^+ concentration inside porous electrodes and electrolyte, assuming a uniform reaction rate distribution. SoH has been defined as the storage capacity of an aged cell with respect to its initial capacity. Considering the loss of Li-ions, loss of active material, and resistance increment,

co-estimation of SoC and SoH has also been performed with an EKF procedure. Liu *et al.* [319] adopted a PSS method and average reaction rate distribution for the Li^+ concentration inside the electrodes and a polynomial approximation for the Li^+ concentration in the electrolyte. The electric potential distribution and overpotentials were also simplified by making use of an average reaction rate distribution. Using a particle filter (PF), SoH estimation can be achieved with high accuracy. Figure 18c compares the referenced and the estimated SoH for 15 cells by this method. It is shown that the estimated SoH is accurate and robust.

Besides the online estimation of SoC and SoH, other states, including State-of-Power (SoP), State-of-Energy (SoE), State-of-Temperature (SoT) [313, 322], can also be determined by making use of complete and simplified P2D-models coupled with state filters or other techniques.

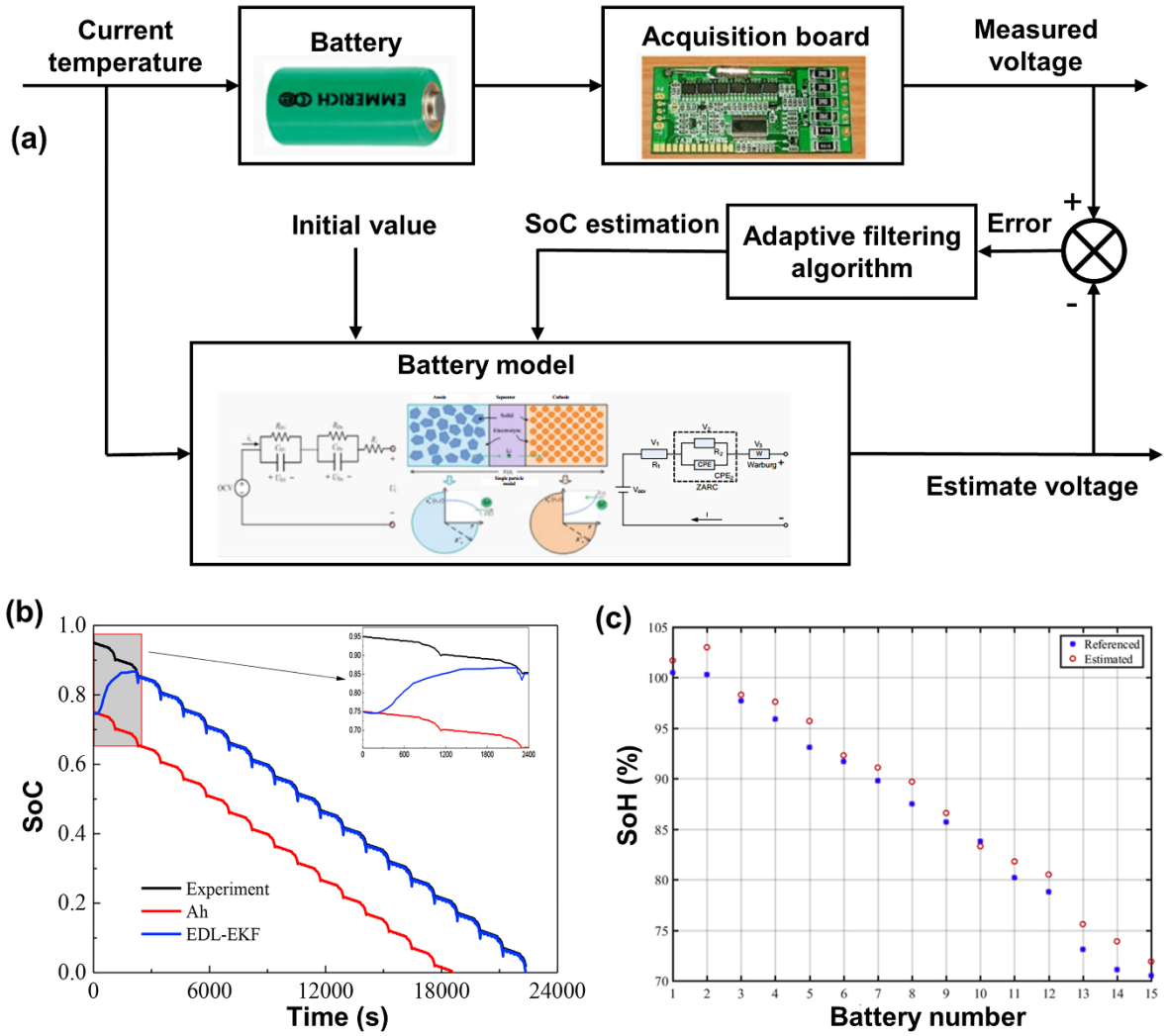

Figure 18. (a) General flowchart of a model-based SoC estimation method [323]. (b) Comparison of estimated SoC by experiment method (black curve), Ah method (red curve), and proposed electrical double layer and extended Kalman filter (EDL-EKF) method (blue curve) [311]. (c)

Comparison of simulated (red) and referenced (blue) SoH for 15 different cells [319]. (a) Reproduced with permission [323]. Copyright 2020, Springer Nature. (b) Reproduced with permission [311]. Copyright 2019, Elsevier. (c) Reproduced with permission [319]. Copyright 2020, Elsevier.

3.6 Other applications

P2D-based models can also be used for other applications, such as electrode and electrolyte parameters extraction and estimation [74, 75], 2D and 3D simulations [324, 325], fault diagnosis and predictions [155, 326, 327], fast charging optimizations [328, 329], *etc.* It can be applied not only for modeling porous electrodes in liquid-electrolyte LIBs, but also for the porous electrode in solid-state batteries. Importantly, some points need to carefully treat for the porous electrode modeling in solid-state battery.

As described in Section 2, porosity ε is defined as the volume ratio between the void space with respect to the total volume. In a typical liquid-electrolyte Li-ion battery, the ionic transport in the electrolyte is modified by the porosity ε since this void space is filled by liquid electrolyte, for example, Equation 7 and 12. However, the porosity is used differently in solid-state battery electrodes. The porosity ε should be differentiated from the volume ratio of solid electrolyte ($\varepsilon_{\mathrm{SE}}$) [330-332], which is defined as the ratio between the solid electrolyte volume with respect to the total volume. The ionic transport in the solid electrolyte is confined with the ratio of $\varepsilon_{\mathrm{SE}}$, not the porosity ε any longer [332]. The tortuosity (τ) is therefore influenced by the volume ratio of solid electrolyte $\varepsilon_{\mathrm{SE}}$. Applying porous electrode modeling can reveal the relationships between solid-state battery performance and electrode microstructures [332, 333]. It shows that small $\varepsilon_{\mathrm{SE}}$ leads to a large τ, a similar dependence as the porous electrode in liquid electrolyte. It also reveals that small void space volume ε and large solid electrolyte volume $\varepsilon_{\mathrm{SE}}$ helps to increase the effective ionic conductivity and reduce the tortuosity significantly. Small active particle size causes a slight decrease in effective ionic conductivity but facilitates Li diffusion inside particles. A trade-off strategy needs to be applied. Rate capability is improved by a high $\varepsilon_{\mathrm{SE}}$, a low τ, and a thin electrode thickness.

Other battery chemistry with porous structures can also be simulated, such as Na-ion battery [48], Li-S battery [334], fuel cell [335], redox flow cell [336], *etc*.

4. Challenges and outlook

Modeling nowadays has become an important tool for the fundamental research and engineering for LIBs. The P2D-based porous electrode model is one of the most popular models because it provides a deep understanding of the thermodynamics, reaction kinetics, and transport processes inside LIBs. The applications of the P2D porous electrode model to LIBs have been systematically reviewed in Section 3. In this Section, the remaining challenges will be discussed, and these issues might be addressed in future research:

1. P2D models include a macroscale and microscale dimension, as shown in Figure 3. On a macroscale, the P2D model only considers battery parameters and properties in the thickness direction. In-plane direction inhomogeneities are ignored. This simplification helps to reduce the computing complexity. Still, it could miss some important aspects, such as reaction rate inhomogeneity and temperature gradients in the in-plane direction, which play an important role for large-scale batteries and high current applications [337, 338]. The P2D model, therefore, needs to be extended to P3D [339] or even P4D models to cope with the above battery properties. However, such an approach will surely increase the calculation burden. On a microscale, all active particles are considered spheres in the P2D models, and Li diffusion inside particles is assumed to be isotropic. However, the geometries of active particles are in reality, very complicated, varying from spherical to more irregular shapes. The diffusion pathways for various materials changes from 1-dimensional for olivine materials ($LiFePO_4$) and 2-dimensional for layered materials ($LiCoO_2$, C_6) to 3-dimensional for spinel-type of materials ($LiMn_2O_4$) [4, 340]. These physical details may lead to more accurate models but significantly increase the model complexity. A trade-off strategy between high accuracy and low computational cost is quite challenging and very likely will be addressed in future research.

2. Owing to the advantages of porous electrode models, some hardly measurable battery properties, such as the Li^+ concentration distribution in the electrolyte and electrodes, the electric potential, and reaction rate distribution, can accurately be simulated. However, these simulated properties highly rely on the parameters given to the model, such as porosity, tortuosity, diffusion coefficients, electronic and ionic conductivities, *etc*. Therefore, it is vital to experimentally determine these battery parameters with high accuracy. Various types of simulations and experimental techniques have been used, for example, reconstruction of porous electrodes by focused ion beam (FIB) and scanning electron microscopy (SEM) [341], impedance spectroscopy (EIS) analysis based on transmission line models (TLM) [30, 37], and restricted-diffusion methods (RDM) [30]. Transport properties of ions in the electrolytes are a function of

concentration and temperature. Accurate determination of different electrolyte systems and electrode materials is also essential and highly demanded. Electrochemical experiments and mathematical models can be used together in this regard [74, 342].

3. Optimization of the battery design is an important topic for engineering applications. Simulations by porous electrode models can reveal the influence of different parameters on the battery performance. It can achieve fast and reliable optimization in practice. In this field, several points need to be carefully treated: *(i)* Optimization objectives need to be optimized for high-energy and high-power batteries. *(ii)* Multiple effects need to be considered by changing one parameter, *i.e.* increasing electronic conductivity but decreasing the porosity of the porous electrode by adding more conducting additives, increasing porosity and also increasing the electrode thickness by reducing the pressing pressure. *(iii)* Saturation conditions, which are defined by the maximum achievable battery performance, need to be considered [100]. *(iv)* Battery aging needs to be taken into consideration for optimized designs.

4. The influence of the reaction rate distribution on battery properties, including overpotential, impedance, temperature, stress, and aging, should be carefully investigated. Influenced by thermodynamics and kinetics, the reaction rate distribution is generally not uniform across porous electrodes. Nonuniform reaction rate distribution will cause a nonuniform utilization of active materials across porous electrodes. This behavior will generate additional battery overpotential [141]. The influence of nonuniform reaction rate distribution on the impedance is still not clear. A nonuniform reaction rate distribution usually influences the temperature distribution in the in-plane direction. Areas near the positive tap generally show higher temperatures. Active electrode particles near the separator interface usually suffer more from parasitic side reactions and larger stress, leading to a higher degree of degradation. P2D models can be applied to visualize these phenomena, leading to improvements in electrode performance and battery design.

5. Ageing models still need further development. Several points have to be stressed for future considerations: *(i)* Electron tunneling approach can be added to aging models to give an accurate elaboration of the SEI formation mechanism [207, 223]. Up to date, different approaches have been used to describe the SEI models, as shown in Equations 43a-d. A Butler-Volmer type of equations under diffusion or kinetic control are mostly used. However, this mechanism only involves the general formation of SEI without considering details, such as SEI's inner and outer layers. *(ii)* Active materials experience particle fracturing and interfacial debonding during cycling. However, it is still challenging to model these two types of degradation mechanisms.

Fractures lead to more exposed particle surfaces to the electrolyte. That increases the SEI formation and hinders Li^+ diffusion inside the particles. The fractures also increase the probability of particle breakage and disturb the electrical connection with the conducting matrix. Particle fracturing is often related to cycle numbers and DIS by Paris Law [243, 252]. Correlating fracturing to the diffusion, kinetic properties, and particle breakage remains a challenge. Interfacial debonding occurs during extended cycling due to repeated volume changes of active electrode particles and mechanical fatigue of binders. DIS is usually assigned as a reason for interfacial debonding. However, it is still highly desirable to physically relate the interfacial debonding to LAM during cycling.

6. Model simplification relies on reducing battery operating variables, such as Li^+ concentration in the electrodes and electrolyte, electric potential, and reaction rate distribution inside the porous electrodes. Realizing the reduction of battery operation variables will increase the computing efficiency. However, the simulation accuracy still needs to be improved, especially at high current loads. Balancing model reduction and simulation accuracy should be investigated in more detail in future research. In BMS applications, simplified P2D models are typically used. Battery states (SoC and SoH) are subsequently estimated by state filters. Several points could be addressed in future research: *(i)* The ability of fast response needs to be improved through calculation optimization; *(ii)* For aged cells, the SoC estimation should consider the influence of SoH; *(iii)* Fault tolerance and correction need to be investigated, especially for aged cells, and *(iv)* State estimation methods should be improved to adapt to batteries with flat OCV curves.

5. Conclusions

The present paper reviewed the development of pseudo-two-dimensional (P2D) porous electrode models and their applications to Li-ion batteries. The P2D model, using a combination of the porous electrode theory and concentrated solution theory, provides a basic theoretical framework for the physical and electrochemical processes taking place inside Li-ion batteries (LIBs). Simulations of the P2D-based model have been extensively used for LIBs and provide a better understanding of the reaction mechanisms and the battery state monitoring. Through the modeling, battery properties can be visualized, *i.e.,* output voltage and current, Li^+ concentration distribution and electric potential distribution in the electrolyte and electrode, and reaction rate distribution. Based on the modeling results, the optimization of battery design can

be critically made. The features of battery overpotential and impedance can also be explained, revealing a deep understanding of the reaction mechanism inside porous electrodes. The simulated overpotential and Li concentration distribution from the P2D model can be used to calculate the temperature and stress distribution inside the battery. Equipped with an aging mechanism, the P2D model can simulate the battery degradation and suggest better battery designs for stable cycling behavior. The simplified P2D model can be applied to estimate and monitor battery states in real-time with the help of state observers. Due to the numerous advantages, P2D-based models have become essential for developing LIBs in scientific research and engineering fields. In scientific research, complicated electrode and active materials geometry details and other sophisticated physical parameters can be included in the model to reveal battery properties during operations. The P2D-based models need to be further simplified in the engineering field while keeping the accuracy to meet the requirements for real-time responses.

Table 6. List of symbols.

Nomenclature	
P2D model	
a	Specific interfacial area of the porous electrode (m^{-1})
$brugg$	Bruggeman coefficient in the porous electrode and separator membrane region (-)
c_1	Li concentration in the solid particle (mol m^{-3})
c_1^s	Surface Li concentration of the solid particle (mol m^{-3})
$\overline{c_1}$	Total average Li concentration in the solid particle (mol m^{-3})
c_2	Electrolyte concentration (mol m^{-3})
D_2	Diffusion coefficient of the electrolyte (m^2 s^{-1})
$D_{2,m}^{eff}$	Effective diffusion coefficient of the electrolyte in the porous electrode and separator region $D_{2,i}^{eff} = D_{2,i}(\varepsilon_i)^{brugg_i}$, $m = n, sep, p$ (m^2 s^{-1})
$D_{1,m}$	Diffusion coefficient of Li-ions in the solid particle, $m = n, p$ (m^2 s^{-1})
F	Faraday's constant, 96487 (C mol^{-1})
i_1	Current density in the solid (A m^{-2})
i_2	Current density in the electrolyte (A m^{-2})
I	Applied current density (A m^{-2})
i^0	Exchange current density of the porous electrode (A m^{-2})
j	Reaction-rate distribution of the porous electrode (mol m^{-2} s^{-1})
k	Kinetic constant of the porous electrode (-)
L	Thickness of the cell, equal to $\delta_n + \delta_{sep} + \delta_p$ (m)
r_m	Radius vector of the C-based particle, $m = n, p$ (-)
R	Gas constant, 8.314 (J mol^{-1} K^{-1})
R_f	Ohmic resistance (Ωm^2)
R_m	Radius of the solid particle, $m = n, p$ (m)
t	Time vector (s)

t_+	Transference number of Li-ions in the electrolyte (-)
T	Temperature (K)
U_m	Equilibrium potential of the porous electrode, *m = n, p* (V)
x	Normalized position vector of the battery (-)
α	Charge-transfer coefficients (-)
δ_m	Thickness of the porous electrode and separator, *m = n, sep, p* (m)
ε_m	Porosity of the porous electrode and separator, *m = n, sep, p* (-)
η_m^{ct}	Charge-transfer overpotential of the porous electrode, *m = n, p* (V)
Φ_1	Potential in the solid (V)
Φ_2	Potential in the solution (V)
κ_m	Ionic conductivity of the electrolyte *m = n, sep, p,* (S m^{-1})
σ_m	Electronic conductivity of the solid *m = n, p,* (S m^{-1})
κ_m^{eff}	Effective ionic conductivity of the electrolyte in the porous electrode and separator region $\kappa_m^{eff} = \kappa_m(\varepsilon_m)^{brugg_m}$, *m = n, sep, p* (S m^{-1})
σ_m^{eff}	Effective electronic conductivity of the porous electrode $\sigma_m^{eff} = \sigma_i(1-\varepsilon_m)$, (S m^{-1})
$f_\pm$	Activity coefficient of electrolyte salt, (-)
Subscripts	
1	Properties in the solid phase of the electrode
2	Properties in the electrolyte phase
n	Negative porous electrode
sep	Porous separator
p	Positive porous electrode
Superscripts	
s	Surface
ct	Charge transfer
eff	Effective properties
Temperature model	
C_p	Specific heat capacity (J kg^{-1}K^{-1})
h	Convective heat transfer coefficient (W m^{-2} K^{-1})
Q_{re}	Reversible heat generation rate (W m^{-3})
Q_{irr}	Irreversible heat generation rate (W m^{-3})
Q_p	Polarization heat generation rate (W m^{-3})
Q_{ohm}	Ohmic heat rate (W m^{-3})
Q_e	Solution-phase ohm heat rate (W m^{-3})
$Q_{s,m}$	Solid-phase ohmic heat rate, *m = n, p* (W m^{-3})
Q_{cc}	Current-collector heat rate (W m^{-3})
ΔS_m	Entropy change, *m = n, p* (J mol^{-1} K^{-1})
T	Battery temperature (K)
T_{amb}	Ambient temperature (K)
ρ	Density (kg m^{-3})
λ	Thermal conductivity (W m^{-1} K^{-1})
ε	emissivity factor (-)
σ	Stefan–Boltzmann constant (5.6704×10^{-8} J s^{-1} m^{-2} K^{-4})
$\sigma_{cc,m}$	Electronic conductivity of the current collector, *m = n, p* (S m^{-1})
$\Phi_{cc,m}$	Electric potential of the current collector, *m = n, p* (V)
Stress model	
E	Young's modulus (Pa)
σ_r	Radial stress (Pa)

σ_θ	Tangential stress (Pa)
σ_h	Hydrostatic stress (Pa)
ε_r	Radial strain (-)
ε_θ	Tangential strain (-)
u	Displacement (m)
υ	Poisson's ratio (-)
Ω	Partial molar volume (m^3 mol^{-1})
Aging model	
c_{EC}^s	EC concentration at the surface of the electrode (mol m^{-3})
c_{EC}^0	Initial EC concentration at the surface of the electrode (mol m^{-3})
c_{Li}	Li concentration in the plated Li (mol m^{-3})
c_{SEI}	SEI concentration at the surface of the electrode (mol m^{-3})
D_{EC}	Diffusion coefficient of EC (m^2 s^{-1})
D_1^{cyc}	Li diffusion coefficient in solid after cycles (m^2 s^{-1})
E^{cyc}	Young's modulus after cycles (Pa)
ΔE	Energy barrier (eV)
j_{SEI}	Reaction rate of the SEI formation (mol m^{-2} s^{-1})
j_{LP}	Reaction rate of Li plating (mol m^{-2} s^{-1})
j_{TMD}	Reaction rate of transition metal dissolution (mol m^{-2} s^{-1})
$j_{tl,C}$	Electron tunneling induced reaction rate of graphite electrode (C) (mol m^{-2} s^{-1})
j_{tot}	Total reaction rate (mol m^{-2} s^{-1})
$l_{tot,C}^{in}$	Total inner SEI layer thickness at graphite electrode (m)
l_{tot}	Total SEI thickness (m)
m_e	Electron mass (kg)
M_m	Molar mass, *m = SEI, Li, C* (g mol^{-1})
P_0	Electron tunneling probability (-)
R_{film}	Film resistance (Ω m^2))
U_{SEI}	Equilibrium potential of the SEI formation reaction (V)
U_{TMD}	Equilibrium potential of transition metal dissolution (V)
U_{eq}	Equilibrium potential of the electrode (V)
x	State of Charge (SoC) of graphite electrode (-)
δ_{film}	Thickness of film (m)
k	Proportionality constant (-)
κ_{SEI}	Conductivity of the SEI (S m^{-1})
ρ_m	Density, *m = SEI, Li, C* (g mol^{-1})
$\alpha_{c,m}$	Cathodic charge-transfer coefficient *m = SEI, LP* (-)
β	Fraction of plated Li turning into SEI (-)
β_1	Damage slop parameter 1 (-)
β_2	Damage slop parameter 2 (-)
ξ	Damage level (-)
d_0	Initial damage threshold (-)
d	Maximum damage level (-)
σ_{yield}	Yield strength (Pa)
v_e	Fermi velocity of electron in the bulk of graphite (m s^{-1})
b	Exponential factor of the damage (-)
$\hbar$	Reduced Planck constant (1.055×10^{-34} J s)
χ	Specific conductivity of SEI (S m^{-1})
ρ	Electronic resistivity of SEI (Ω m)

References

[1] D. Larcher, J. M. Tarascon, Nat. Chem. 2015, 7, 19.
[2] Y. Yang, E. G. Okonkwo, G. Huang, S. Xu, W. Sun, Y. He, Energy Storage Mater. 2021, 36, 186.
[3] L. Yang, Z. G. Chen, M. S. Dargusch, J. Zou, Adv. Energy Mater. 2017, 8, 170179.
[4] N. Nitta, F. Wu, J. T. Lee, G. Yushin, Mater. Today 2015, 18, 252.
[5] T. Kim, W. Song, D.-Y. Son, L. K. Ono, Y. Qi, J. Mater. Chem. A 2019, 7, 2942.
[6] Q. Zhao, S. Stalin, C.-Z. Zhao, L. A. Archer, Nat. Rev. Mater. 2020, 5, 229.
[7] Q. Li, J. Chen, L. Fan, X. Kong, Y. Lu, Green Energy Environ. 2016, 1, 18.
[8] M. Park, X. Zhang, M. Chung, G. B. Less, A. M. Sastry, J. Power Sources 2010, 195, 7904.
[9] A. A. Franco, RSC Adv. 2013, 3.
[10] S. Shi, J. Gao, Y. Liu, Y. Zhao, Q. Wu, W. Ju, C. Ouyang, R. Xiao, Chinese Physics B 2016, 25.
[11] V. Ramadesigan, P. W. C. Northrop, S. De, S. Santhanagopalan, R. D. Braatz, V. R. Subramanian, J. Electrochem. Soc. 2012, 159, R31.
[12] A. A. Franco, A. Rucci, D. Brandell, C. Frayret, M. Gaberscek, P. Jankowski, P. Johansson, Chem. Rev. 2019, 119, 4569.
[13] S. J. An, J. Li, C. Daniel, D. Mohanty, S. Nagpure, D. L. Wood, Carbon 2016, 105, 52.
[14] Q. Wang, G. Zhang, Y. Li, Z. Hong, D. Wang, S. Shi, Npj Comput. Mater. 2020, 6.
[15] A. Fotouhi, D. J. Auger, K. Propp, S. Longo, M. Wild, Renew. Sust. Energ. Rev. 2016, 56, 1008.
[16] A. Jokar, B. Rajabloo, M. Désilets, M. Lacroix, J. Power Sources 2016, 327, 44.
[17] Q. He, B. Yu, Z. Li, Y. Zhao, Energy Environ. Sci. 2019, 2, 264.
[18] S. Nejad, D. T. Gladwin, D. A. Stone, J. Power Sources 2016, 316, 183.
[19] J. Meng, G. Luo, M. Ricco, M. Swierczynski, D.-I. Stroe, R. Teodorescu, Appl. Sci. 2018, 8, 659.
[20] H. J. Bergveld, W. S. Kruijt, P. H. L. Notten, *Battery management Systems: design by modelling*, Kluwer Academic Publishers, 2002.
[21] H. J. Bergveld, W. S. Kruijt, P. H. L. Notten, J. Power Sources 1999, 77, 143.
[22] P. H. L. Notten, W. S. Kruijt, H. J. Bergveld, J. Electrochem. Soc. 1998, 145, 3774.
[23] U. Krewer, F. Röder, E. Harinath, R. D. Braatz, B. Bedürftig, R. Findeisen, J. Electrochem. Soc. 2018, 165, A3656.
[24] S. Wilkins, S. v. Sterkenburg, E. Hoedemaekers, B. Rosca, D. Danilov, R. Baert, EVS30 International Battery, Hybrid and Fuel Cell Electric Vehicle Symposium 2017.
[25] A. M. Bizeray, S. Zhao, S. R. Duncan, D. A. Howey, J. Power Sources 2015, 296, 400.
[26] J. Newman, W. Tiedemann, AIChE Journal 1975, 21, 25.
[27] M. Doyle, T. F. Fuller, J. Newman, J. Electrochem. Soc. 1993, 140, 1526.
[28] T. F. Fuller, M. Doyle, J. Newman, J. Electrochem. Soc. 1994, 141, 1.
[29] A. Vu, Y. Qian, A. Stein, Adv. Energy Mater. 2012, 2, 1056.
[30] T.-T. Nguyen, A. Demortière, B. Fleutot, B. Delobel, C. Delacourt, S. J. Cooper, Npj Comput. Mater. 2020, 6, 123.
[31] J. Le Houx, D. Kramer, Energy Rep. 2020, 6, 1.
[32] Y. Liang, C. Z. Zhao, H. Yuan, Y. Chen, W. Zhang, J. Q. Huang, D. Yu, Y. Liu, M. M. Titirici, Y. L. Chueh, H. Yu, Q. Zhang, InfoMat 2019, 1, 6.
[33] S. Santhanagopalan, R. E. White, Encyclopedia of Electrochemical Power Sources 2009, 110.
[34] W. B. Hawley, J. Li, J. Energy Storage 2019, 25, 100862.
[35] M. Smith, R. E. García, Q. C. Horn, J. Electrochem. Soc. 2009, 156, A896.

[36] D. Qu, in *AIP Conference Proceedings*, 2014, 14.
[37] B. Suthar, J. Landesfeind, A. Eldiven, H. A. Gasteiger, J. Electrochem. Soc. 2018, 165, A2008.
[38] X. Zhang, Z. Hui, S. King, L. Wang, Z. Ju, J. Wu, K. J. Takeuchi, A. C. Marschilok, A. C. West, E. S. Takeuchi, G. Yu, Nano Lett. 2021, 21, 5896.
[39] D. Sauerteig, N. Hanselmann, A. Arzberger, H. Reinshagen, S. Ivanov, A. Bund, J. Power Sources 2018, 378, 235.
[40] J. Euler, W. Nonnenmacher, Electrochim. Acta 1960, 2, 268.
[41] J. Newman, C. W. Tobias, J. Electrochem. Soc. 1962, 109, 1183.
[42] J. Newman, T. W. Chapman, AIChE Journal 1973, 19, 343.
[43] S. Santhanagopalan, Q. Guo, P. Ramadass, R. E. White, J. Power Sources 2006, 156, 620.
[44] J. C. Forman, S. J. Moura, J. L. Stein, H. K. Fathy, J. Power Sources 2012, 210, 263.
[45] H. Arunachalam, S. Onori, J. Electrochem. Soc. 2019, 166, A1380.
[46] I. Korotkin, S. Sahu, S. E. J. O'Kane, G. Richardson, J. M. Foster, J. Electrochem. Soc. 2021, 168, 060544.
[47] D. Danilov, R. A. H. Niessen, P. H. L. Notten, J. Electrochem. Soc. 2011, 158, A215.
[48] K. Chayambuka, G. Mulder, D. L. Danilov, P. H. L. Notten, Journal of Power Sources Advances 2021, 9, 100056.
[49] A. J. Bard, L. R. Faulkner, *Electrochemical Methods Fundamentals and Applications*, John Wiley & Sons, 1980.
[50] J. Newman, K. E. Thomas-Alyea, *Electrochemical Systems*, John Wiley & Sons 2004.
[51] A. Salvadori, D. Grazioli, M. Magri, M. G. D. Geers, D. Danilov, P. H. L. Notten, J. Power Sources 2015, 294, 696.
[52] A. Salvadori, D. Grazioli, M. G. D. Geers, D. Danilov, P. H. L. Notten, J. Power Sources 2015, 293, 892.
[53] D. Danilov, P. H. L. Notten, Electrochim. Acta 2008, 53, 5569.
[54] G. W. Richardson, J. M. Foster, R. Ranom, C. P. Please, A. M. Ramos, European Journal of Applied Mathematics 2021, 1.
[55] V. Ramadesigan, V. Boovaragavan, J. C. Pirkle, V. R. Subramanian, J. Electrochem. Soc. 2010, 157, A854.
[56] M. Torchio, L. Magni, R. B. Gopaluni, R. D. Braatz, D. M. Raimondo, J. Electrochem. Soc. 2016, 163, A1192.
[57] G. G. Botte, V. R. Subramanian, R. E. White, Electrochim. Acta 2000, 45, 2595.
[58] M. D. Berliner, H. Zhao, S. Das, M. Forsuelo, B. Jiang, W. H. Chueh, M. Z. Bazant, R. D. Braatz, J. Electrochem. Soc. 2021, 168, 090546.
[59] V. Sulzer, S. G. Marquis, R. Timms, M. Robinson, S. J. Chapman, J. Open Res. Softw. 2021, 9.
[60] M. Doyle, PhD Thesis 1995.
[61] C. Chen, Y. Zuo, W. Ye, X. Li, Z. Deng, S. P. Ong, Adv. Energy Mater. 2020, 10.
[62] Y. Elbaz, D. Furman, M. Caspary Toroker, Adv. Funct. Mater. 2019, 30.
[63] A. Mishra, A. Mehta, S. Basu, S. J. Malode, N. P. Shetti, S. S. Shukla, M. N. Nadagouda, T. M. Aminabhavi, Materials Science for Energy Technologies 2018, 1, 182.
[64] Y. Yamada, J. Wang, S. Ko, E. Watanabe, A. Yamada, Nat. Energy 2019, 4, 269.
[65] K. L. Gering, Electrochim. Acta 2006, 51, 3125.
[66] D. Takamatsu, A. Yoneyama, Y. Asari, T. Hirano, J. Am. Chem. Soc. 2018, 140, 1608.
[67] D.-H. Kim, S. Hwang, J.-J. Cho, S. Yu, S. Kim, J. Jeon, K. H. Ahn, C. Lee, H.-K. Song, H. Lee, ACS Energy Lett. 2019, 4, 1265.
[68] S. J. Harris, A. Timmons, D. R. Baker, C. Monroe, Chem. Phys. Lett. 2010, 485, 265.

[69] S. A. Krachkovskiy, J. M. Foster, J. D. Bazak, B. J. Balcom, G. R. Goward, J. Phys. Chem. C 2018, 122, 21784.
[70] H. Murayama, K. Kitada, K. Fukuda, A. Mitsui, K. Ohara, H. Arai, Y. Uchimoto, Z. Ogumi, E. Matsubara, J. Phys. Chem. C 2014, 118, 20750.
[71] H. Cha, J. Kim, H. Lee, N. Kim, J. Hwang, J. Sung, M. Yoon, K. Kim, J. Cho, Adv. Mater. 2020, 2003040.
[72] B. G. Chae, S. Y. Park, J. H. Song, E. Lee, W. S. Jeon, Nat Commun 2021, 12, 3814.
[73] L. O. Valøen, J. N. Reimers, J. Electrochem. Soc. 2005, 152, A882.
[74] A. Ehrl, J. Landesfeind, W. A. Wall, H. A. Gasteiger, J. Electrochem. Soc. 2017, 164, A826.
[75] D. W. Dees, S. Kawauchi, D. P. Abraham, J. Prakash, J. Power Sources 2009, 189, 263.
[76] M. Doyle, T. F. Fuller, J. Newman, Electrochim. Acta 1994, 39, 2073.
[77] K. P. C. Yao, J. S. Okasinski, K. Kalaga, I. A. Shkrob, D. P. Abraham, Energy Environ. Sci. 2019, 12, 656.
[78] F. Rittweger, C. Modrzynski, V. Roscher, D. L. Danilov, P. H. L. Notten, K.-R. Riemschneider, J. Power Sources 2021, 482, 228943.
[79] C. Hogrefe, S. Hein, T. Waldmann, T. Danner, K. Richter, A. Latz, M. Wohlfahrt-Mehrens, J. Electrochem. Soc. 2020, 167, 140546.
[80] F. Jiang, P. Peng, Sci Rep 2016, 6, 32639.
[81] A. M. Colclasure, T. R. Tanim, A. N. Jansen, S. E. Trask, A. R. Dunlop, B. J. Polzin, I. Bloom, D. Robertson, L. Flores, M. Evans, E. J. Dufek, K. Smith, Electrochim. Acta 2020, 337, 135854.
[82] L. Xia, E. Najafi, Z. Li, H. J. Bergveld, M. C. F. Donkers, Appl. Energy 2017, 208, 1285.
[83] M. Ghalkhani, F. Bahiraei, G.-A. Nazri, M. Saif, Electrochim. Acta 2017, 247, 569.
[84] M. Xu, B. Reichman, X. Wang, Energy 2019, 186, 115864.
[85] M. Al-Gabalawy, N. S. Hosny, S. A. Hussien, Batteries 2020, 6, 37.
[86] S. Han, Y. Tang, S. Khaleghi Rahimian, J. Power Sources 2021, 490, 229571.
[87] Y. Bai, Y. Zhao, W. Liu, B.-X. Xu, J. Power Sources 2019, 422, 92.
[88] S. Malifarge, B. Delobel, C. Delacourt, J. Electrochem. Soc. 2018, 165, A1275.
[89] S. Khaleghi Rahimian, S. Rayman, R. E. White, J. Power Sources 2013, 224, 180.
[90] Z. Geng, S. Wang, M. J. Lacey, D. Brandell, T. Thiringer, Electrochim. Acta 2021, 372, 137829.
[91] L. H. Saw, Y. Ye, A. A. O. Tay, Energy Convers. Manag. 2013, 75, 162.
[92] Z. Chen, D. L. Danilov, R.-A. Eichel, P. H. L. Notten, Energy Storage Mater. 2022, 48.
[93] T.-S. Dao, C. P. Vyasarayani, J. McPhee, J. Power Sources 2012, 198, 329.
[94] G. Richardson, I. Korotkin, R. Ranom, M. Castle, J. M. Foster, Electrochim. Acta 2020, 339, 135862.
[95] Y. Orikasa, Y. Gogyo, H. Yamashige, M. Katayama, K. Chen, T. Mori, K. Yamamoto, T. Masese, Y. Inada, T. Ohta, Z. Siroma, S. Kato, H. Kinoshita, H. Arai, Z. Ogumi, Y. Uchimoto, Sci. Rep. 2016, 6, 26382.
[96] F. Wang, M. Tang, J. Electrochem. Soc. 2020, 167, 120543.
[97] Y. Tang, M. Jia, J. Li, Y. Lai, Y. Cheng, Y. Liu, J. Electrochem. Soc. 2014, 161, E3021.
[98] R. J. Brodd, Electrochim. Acta 1966, 11, 1107.
[99] R. Darling, J. Newman, J. Electrochem. Soc. 1997, 144, 3057.
[100] Z. Chen, D. L. Danilov, R.-A. Eichel, P. H. L. Notten, Electrochem. Commun. 2020, 121, 106865.

[101] M. Wang, J. Li, X. He, H. Wu, C. Wan, J. Power Sources 2012, 207, 127.
[102] M. Doyle, J. Newman, J. Appl. Electrochem. 1997, 27, 846.
[103] M. Doyle, J. Newman, J. Power Sources 1995, 54, 46.
[104] C. Heubner, M. Schneider, A. Michaelis, Adv. Energy Mater. 2019, 10, 1902523.
[105] Lain, Brandon, Kendrick, Batteries 2019, 5, 64.
[106] S. De, P. W. C. Northrop, V. Ramadesigan, V. R. Subramanian, J. Power Sources 2013, 227, 161.
[107] W. Mei, H. Chen, J. Sun, Q. Wang, Sustain. Energy Fuels 2019, 3, 148.
[108] S. T. Taleghani, B. Marcos, K. Zaghib, G. Lantagne, J. Electrochem. Soc. 2017, 164, E3179.
[109] H. Hamed, S. Yari, J. D'Haen, F. U. Renner, N. Reddy, A. Hardy, M. Safari, Adv. Energy Mater. 2020, 10, 2002492.
[110] D. Miranda, A. Gören, C. M. Costa, M. M. Silva, A. M. Almeida, S. Lanceros-Méndez, Energy 2019, 172, 68.
[111] F. Wang, M. Tang, Cell Reports Physical Science 2020, 1, 100192.
[112] C. Liu, L. Liu, J. Electrochem. Soc. 2017, 164, E3254.
[113] Z. Hui, K. S. Mayilvahanan, K. Ganko, Y. Yang, X. Zhang, Z. Ju, K. J. Takeuchi, A. C. Marschilok, G. Yu, E. Takeuchi, A. C. West, Energy Storage Mater. 2021, 39, 176.
[114] K. Xu, Chem. Rev. 2004, 104, 4303.
[115] M. Jiang, Q. Zhang, X. Wu, Z. Chen, D. L. Danilov, R.-A. Eichel, P. H. L. Notten, ACS Appl. Energy Mater. 2020, 3, 6583.
[116] S. B. Chikkannanavar, D. M. Bernardi, L. Liu, J. Power Sources 2014, 248, 91.
[117] S. Chae, S. H. Choi, N. Kim, J. Sung, J. Cho, Angew. Chem. Int. Ed 2020, 59, 110.
[118] J. Sturm, A. Rheinfeld, I. Zilberman, F. B. Spingler, S. Kosch, F. Frie, A. Jossen, J. Power Sources 2019, 412, 204.
[119] K. H. Chen, V. Goel, M. J. Namkoong, M. Wied, S. Müller, V. Wood, J. Sakamoto, K. Thornton, N. P. Dasgupta, Adv. Energy Mater. 2020, 2003336.
[120] X. Li, S.-Y. Choe, W. T. Joe, J. Power Sources 2015, 294, 545.
[121] P. F. Lory, B. Mathieu, S. Genies, Y. Reynier, A. Boulineau, W. Hong, M. Chandesris, J. Electrochem. Soc. 2020, 167, 120506.
[122] S. Jung, J. Power Sources 2014, 264, 184.
[123] W. A. Appiah, J. Park, L. Van Khue, Y. Lee, J. Choi, M.-H. Ryou, Y. M. Lee, Electrochim. Acta 2016, 187, 422.
[124] Y. Dai, L. Cai, R. E. White, J. Power Sources 2014, 247, 365.
[125] K. P. C. Yao, J. S. Okasinski, K. Kalaga, J. D. Almer, D. P. Abraham, Adv. Energy Mater. 2019, 9, 1803380.
[126] R. Darling, J. Newman, J. Electrochem. Soc. 1997, 144, 4201.
[127] B. K. Kanchan, P. R. Randive, J. Electrochem. Soc. 2021, 168.
[128] L. H. J. Raijmakers, D. L. Danilov, R. A. Eichel, P. H. L. Notten, Appl. Energy 2019, 240, 918.
[129] K. J. Vetter, Academic Press 1967.
[130] C. Xiao, R. Usiskin, J. Maier, Adv. Funct. Mater. 2021, 2100938.
[131] R. Guo, B. M. Gallant, Chem. Mater. 2020, 32, 5525.
[132] L. H. J. Raijmakers, D. L. Danilov, R. A. Eichel, P. H. L. Notten, Electrochim. Acta 2020, 330, 135147.
[133] N. Kazemi, D. L. Danilov, L. Haverkate, N. J. Dudney, S. Unnikrishnan, P. H. L. Notten, Solid State Ion. 2019, 334, 111.
[134] R. Chandrasekaran, J. Power Sources 2014, 262, 501.
[135] F. Yang, Y. Qiao, B. Gao, P. Duan, Y. Zhu, Ionics 2016, 22, 1603.

[136] A. Nyman, T. G. Zavalis, R. Rlger, M. Behem, G. Lindbergh, J. Electrochem. Soc. 2010, 157, A1236.
[137] V. Srinivasan, J. Newman, J. Electrochem. Soc. 2004, 151, A1517.
[138] E. Prada, D. Di Domenico, Y. Creff, J. Bernard, V. Sauvant-Moynot, F. Huet, J. Electrochem. Soc. 2012, 159, A1508.
[139] D. M. Bernardi, J.-Y. Go, J. Power Sources 2011, 196, 412.
[140] M. Quarti, W. G. Bessler, Energy Technol. 2021, 9, 2001122.
[141] Z. Chen, D. L. Danilov, L. H. J. Raijmakers, K. Chayambuka, M. Jiang, L. Zhou, J. Zhou, R.-A. Eichel, P. H. L. Notten, J. Power Sources 2021, 509, 230345.
[142] R. Chandrasekaran, J. Power Sources 2014, 271, 622.
[143] W. Choi, H.-C. Shin, J. M. Kim, J.-Y. Choi, W.-S. Yoon, J. Electrochem. Sci. Technol. 2020, 11, 1.
[144] J. Huang, Y. Gao, J. Luo, S. Wang, C. Li, S. Chen, J. Zhang, J. Electrochem. Soc. 2020, 167, 166503.
[145] J. Luck, A. Latz, Phys. Chem. Chem. Phys. 2019, 21, 14753.
[146] M. Doyle, J. P. Meyers, J. Newman, J. Electrochem. Soc. 2000, 147, 99.
[147] J. P. Meyers, M. Doyle, R. M. Darling, J. Newman, J. Electrochem. Soc. 2000, 147, 2930.
[148] Y. Xie, J. Li, C. Yuan, Electrochim. Acta 2014, 127, 266.
[149] S. Devan, V. R. Subramanian, R. E. White, J. Electrochem. Soc. 2004, 151, A905.
[150] G. Sikha, R. E. White, J. Electrochem. Soc. 2007, 154, A43.
[151] J. Huang, J. Zhang, J. Electrochem. Soc. 2016, 163, A1983.
[152] D. Gruet, B. Delobel, D. Sicsic, I. T. Lucas, V. Vivier, Electrochim. Acta 2019, 295, 787.
[153] X. Kong, G. L. Plett, M. S. Trimboli, Z. Zhang, Y. Zheng, J. Electrochem. Soc. 2020, 167, 013539.
[154] D. Dees, E. Gunen, D. Abraham, A. Jansen, J. Prakash, J. Electrochem. Soc. 2008, 155, A603.
[155] X. Kong, G. L. Plett, M. Scott Trimboli, Z. Zhang, D. Qiao, T. Zhao, Y. Zheng, J. Energy Storage 2020, 27, 101085.
[156] S. J. Cooper, A. Bertei, D. P. Finegan, N. P. Brandon, Electrochim. Acta 2017, 251, 681.
[157] M. D. Murbach, D. T. Schwartz, J. Electrochem. Soc. 2018, 165, A297.
[158] M. D. Murbach, D. T. Schwartz, J. Electrochem. Soc. 2017, 164, E3311.
[159] L. H. J. Raijmakers, D. L. Danilov, J. P. M. van Lammeren, M. J. G. Lammers, P. H. L. Notten, J. Power Sources 2014, 247, 539.
[160] M. Xiao, S.-Y. Choe, J. Power Sources 2015, 277, 403.
[161] X. Zhou, J. Huang, Z. Pan, M. Ouyang, J. Power Sources 2019, 426, 216.
[162] M. Alipour, C. Ziebert, F. V. Conte, R. Kizilel, Batteries 2020, 6.
[163] S. Ma, M. Jiang, P. Tao, C. Song, J. Wu, J. Wang, T. Deng, W. Shang, Prog. Nat. Sci. 2018, 28, 653.
[164] S. Novais, M. Nascimento, L. Grande, M. F. Domingues, P. Antunes, N. Alberto, C. Leitao, R. Oliveira, S. Koch, G. T. Kim, S. Passerini, J. Pinto, Sensors (Basel) 2016, 16.
[165] Y. Ji, Y. Zhang, C.-Y. Wang, J. Electrochem. Soc. 2013, 160, A636.
[166] S. Du, Y. Lai, L. Ai, L. Ai, Y. Cheng, Y. Tang, M. Jia, Appl. Therm. Eng. 2017, 121, 501.
[167] P. Nie, S.-W. Zhang, A. Ran, C. Yang, S. Chen, Z. Li, X. Zhang, W. Deng, T. Liu, F. Kang, G. Wei, Appl. Therm. Eng. 2021, 184.
[168] Y. Lai, S. Du, L. Ai, L. Ai, Y. Cheng, Y. Tang, M. Jia, Int. J. Hydrog. Energy 2015, 40, 13039.

[169] B. Wu, V. Yufit, M. Marinescu, G. J. Offer, R. F. Martinez-Botas, N. P. Brandon, J. Power Sources 2013, 243, 544.
[170] D. Li, L. Yang, C. Li, Energy 2021, 214, 119057.
[171] D. Wang, H. Huang, Z. Tang, Q. Zhang, B. Yang, B. Zhang, Electrochim. Acta 2020, 362, 137118.
[172] T. Dong, P. Peng, F. Jiang, Int. J. Heat Mass Transfer 2018, 117, 261.
[173] W. Mei, C. Liang, J. Sun, Q. Wang, Int. J. Energy Res. 2020, 44, 8919.
[174] J. Li, Y. Cheng, L. Ai, M. Jia, S. Du, B. Yin, S. Woo, H. Zhang, J. Power Sources 2015, 293, 993.
[175] W. Fang, O. J. Kwon, C.-Y. Wang, Int. J. Energy Res. 2010, 34, 107.
[176] W. Ai, L. Kraft, J. Sturm, A. Jossen, B. Wu, J. Electrochem. Soc. 2019, 167, 013512.
[177] K. Somasundaram, E. Birgersson, A. S. Mujumdar, J. Power Sources 2012, 203, 84.
[178] X. Zhang, X. Chang, Y. Shen, Y. Xiang, J. Energy Storage 2017, 11, 249.
[179] N. Lin, F. Röder, U. Krewer, Energies 2018, 11.
[180] O. Capron, A. Samba, N. Omar, P. Van Den Bossche, J. Van Mierlo, Energies 2015, 8, 10017.
[181] J. Keil, A. Jossen, J. Electrochem. Soc. 2020, 167, 110535.
[182] M. Muratori, N. Ma, M. Canova, Y. Guezennec, in *Proceedings of the ASME 2010 Dynamic Systems and Control Conference*, Cambridge, Massachusetts, USA 2010.
[183] S. Goutam, A. Nikolian, J. Jaguemont, J. Smekens, N. Omar, P. Van Dan Bossche, J. Van Mierlo, Appl. Therm. Eng. 2017, 126, 796.
[184] A. Nazari, S. Farhad, Appl. Therm. Eng. 2017, 125, 1501.
[185] R. Koerver, W. Zhang, L. de Biasi, S. Schweidler, A. O. Kondrakov, S. Kolling, T. Brezesinski, P. Hartmann, W. G. Zeier, J. Janek, Energy Environ. Sci. 2018, 11, 2142.
[186] L. de Biasi, A. O. Kondrakov, H. Geßwein, T. Brezesinski, P. Hartmann, J. Janek, J. Phys. Chem. C 2017, 121, 26163.
[187] Y. Zhao, P. Stein, Y. Bai, M. Al-Siraj, Y. Yang, B.-X. Xu, J. Power Sources 2019, 413, 259.
[188] R. Xu, K. Zhao, J. Electrochem. Energy Convers. Storage 2016, 13.
[189] X. Zhang, W. Shyy, A. Marie Sastry, J. Electrochem. Soc. 2007, 154, A910.
[190] B. Rieger, S. V. Erhard, K. Rumpf, A. Jossen, J. Electrochem. Soc. 2016, 163, A1566.
[191] W. Mei, Q. Duan, P. Qin, J. Xu, Q. Wang, J. Sun, J. Electrochem. Soc. 2019, 166, A3319.
[192] K. Takahashi, V. Srinivasan, J. Electrochem. Soc. 2015, 162, A635.
[193] K. Takahashi, K. Higa, S. Mair, M. Chintapalli, N. Balsara, V. Srinivasan, J. Electrochem. Soc. 2015, 163, A385.
[194] S. Renganathan, G. Sikha, S. Santhanagopalan, R. E. White, J. Electrochem. Soc. 2010, 157, A155.
[195] B. Suthar, P. W. C. Northrop, R. D. Braatz, V. R. Subramanian, J. Electrochem. Soc. 2014, 161, F3144.
[196] J. Christensen, J. Newman, J. Solid State Electrochem. 2006, 10, 293.
[197] T. R. Garrick, X. Huang, V. Srinivasan, J. W. Weidner, J. Electrochem. Soc. 2017, 164, E3552.
[198] H. Li, B. Liu, D. Zhou, C. Zhang, J. Electrochem. Soc. 2020, 167, 120501.
[199] W. Mei, Q. Duan, W. Lu, J. Sun, Q. Wang, J. Clean. Prod. 2020, 274, 122643.
[200] X. Duan, W. Jiang, Y. Zou, W. Lei, Z. Ma, J. Mater. Sci. 2018, 53, 10987.
[201] M. R. Palacin, Chem Soc Rev 2018, 47, 4924.
[202] C. R. Birkl, M. R. Roberts, E. McTurk, P. G. Bruce, D. A. Howey, J. Power Sources 2017, 341, 373.
[203] M. Dubarry, C. Truchot, B. Y. Liaw, J. Power Sources 2012, 219, 204.

[204] X. Han, M. Ouyang, L. Lu, J. Li, Y. Zheng, Z. Li, J. Power Sources 2014, 251, 38.
[205] C. Pastor-Fernández, K. Uddin, G. H. Chouchelamane, W. D. Widanage, J. Marco, J. Power Sources 2017, 360, 301.
[206] J. Christensen, J. Newman, J. Electrochem. Soc. 2005, 152, A818.
[207] D. Li, D. Danilov, Z. Zhang, H. Chen, Y. Yang, P. H. L. Notten, J. Electrochem. Soc. 2015, 162, A858.
[208] X.-G. Yang, Y. Leng, G. Zhang, S. Ge, C.-Y. Wang, J. Power Sources 2017, 360, 28.
[209] J. Wang, J. Purewal, P. Liu, J. Hicks-Garner, S. Soukazian, E. Sherman, A. Sorenson, L. Vu, H. Tataria, M. W. Verbrugge, J. Power Sources 2014, 269, 937.
[210] J. M. Reniers, G. Mulder, D. A. Howey, J. Electrochem. Soc. 2019, 166, A3189.
[211] F. M. Kindermann, J. Keil, A. Frank, A. Jossen, J. Electrochem. Soc. 2017, 164, E287.
[212] A. Barré, B. Deguilhem, S. Grolleau, M. Gérard, F. Suard, D. Riu, J. Power Sources 2013, 241, 680.
[213] E. Peled, S. Menkin, J. Electrochem. Soc. 2017, 164, A1703.
[214] A. Wang, S. Kadam, H. Li, S. Shi, Y. Qi, Npj Comput. Mater. 2018, 4, 15.
[215] Y. Wang, S. Nakamura, M. Ue, P. B. Balbuena, J. Am. Chem. Soc. 2001, 123, 11708.
[216] M. Safari, M. Morcrette, A. Teyssot, C. Delacourt, J. Electrochem. Soc. 2009, 156, A145.
[217] E. Peled, J. Electrochem. Soc. 1979, 12, 2047.
[218] E. Peled, in *Lithium Batteries*, (Ed: J. P. Gabano), Academic Press, NY 1983, 43.
[219] M. Broussely, S. Herreyre, P. Biensan, P. Kasztejna, K. Nechev, R. J. Staniewicz, J. Power Sources 2001, 97, 13.
[220] Y.-X. Lin, Z. Liu, K. Leung, L.-Q. Chen, P. Lu, Y. Qi, J. Power Sources 2016, 309, 221.
[221] D. Li, D. L. Danilov, L. Gao, Y. Yang, P. H. L. Notten, Electrochim. Acta 2016, 210, 445.
[222] D. Li, H. Li, D. Danilov, L. Gao, J. Zhou, R.-A. Eichel, Y. Yang, P. H. L. Notten, J. Power Sources 2018, 396, 444.
[223] D. Li, D. L. Danilov, B. Zwikirsch, M. Fichtner, Y. Yang, R.-A. Eichel, P. H. L. Notten, J. Power Sources 2018, 375, 106.
[224] J. Wang, P. Liu, J. Hicks-Garner, E. Sherman, S. Soukiazian, M. Verbrugge, H. Tataria, J. Musser, P. Finamore, J. Power Sources 2011, 196, 3942.
[225] P. M. Attia, W. C. Chueh, S. J. Harris, J. Electrochem. Soc. 2020, 167, 090535.
[226] N. Kamyab, J. W. Weidner, R. E. White, J. Electrochem. Soc. 2019, 166, A334.
[227] C. Yan, Y.-X. Yao, W.-L. Cai, L. Xu, S. Kaskel, H. S. Park, J.-Q. Huang, J. Energy Chem. 2020, 49, 335.
[228] N. Legrand, B. Knosp, P. Desprez, F. Lapicque, S. Raël, J. Power Sources 2014, 245, 208.
[229] C. Uhlmann, J. Illig, M. Ender, R. Schuster, E. Ivers-Tiffée, J. Power Sources 2015, 279, 428.
[230] H. Ge, T. Aoki, N. Ikeda, S. Suga, T. Isobe, Z. Li, Y. Tabuchi, J. Zhang, J. Electrochem. Soc. 2017, 164, A1050.
[231] M. Petzl, M. Kasper, M. A. Danzer, J. Power Sources 2015, 275, 799.
[232] S. F. Schuster, T. Bach, E. Fleder, J. Müller, M. Brand, G. Sextl, A. Jossen, J. Energy Storage 2015, 1, 44.
[233] J. Keil, N. Paul, V. Baran, P. Keil, R. Gilles, A. Jossen, J. Electrochem. Soc. 2019, 166, A3908.
[234] H. Wang, Y. Zhu, S. C. Kim, A. Pei, Y. Li, D. T. Boyle, H. Wang, Z. Zhang, Y. Ye, W. Huang, Y. Liua, J. Xua, J. Li, F. Liu, Y. Cui, PNAS 2020, 117, 29453.
[235] G. Fuchs, L. Willenberg, F. Ringbeck, D. U. Sauer, Sustainability 2019, 11, 6738.

[236] V. Zinth, C. von Lüders, J. Wilhelm, S. V. Erhard, M. Hofmann, S. Seidlmayer, J. Rebelo-Kornmeier, W. Gan, A. Jossen, R. Gilles, J. Power Sources 2017, 361, 54.
[237] V. Zinth, C. von Lüders, M. Hofmann, J. Hattendorff, I. Buchberger, S. Erhard, J. Rebelo-Kornmeier, A. Jossen, R. Gilles, J. Power Sources 2014, 271, 152.
[238] D. Anseán, M. Dubarry, A. Devie, B. Y. Liaw, V. M. García, J. C. Viera, M. González, J. Power Sources 2017, 356, 36.
[239] X. Zhang, Y. Gao, B. Guo, C. Zhu, X. Zhou, L. Wang, J. Cao, Electrochim. Acta 2020, 343, 136070.
[240] A. Sarkar, P. Shrotriya, A. Chandra, C. Hu, J. Energy Storage 2019, 25, 100911.
[241] A. Lamorgese, R. Mauri, B. Tellini, J. Energy Storage 2018, 20, 289.
[242] S. Dhillon, G. Hernández, N. P. Wagner, A. M. Svensson, D. Brandell, Electrochim. Acta 2021, 377, 138067.
[243] A. A. Tahmasbi, M. H. Eikerling, Electrochim. Acta 2018, 283, 75.
[244] A. Sarkar, I. C. Nlebedim, P. Shrotriya, J. Power Sources 2021, 502, 229145.
[245] T. Katrašnik, I. Mele, K. Zelič, Energy Convers. Manag. 2021, 236, 114036.
[246] Y. Zhao, S.-Y. Choe, J. Kee, Electrochim. Acta 2018, 270, 440.
[247] S.-c. Yang, Y. Hua, D. Qiao, Y.-b. Lian, Y.-w. Pan, Y.-l. He, Electrochim. Acta 2019, 326, 134928.
[248] J. Liang, Y. Gan, M. Yao, Y. Li, Int. J. Heat Mass Transfer 2021, 165, 120615.
[249] B. Suthar, P. W. C. Northrop, D. Rife, V. R. Subramanian, J. Electrochem. Soc. 2015, 162, A1708.
[250] D. Müller, T. Dufaux, K. P. Birke, Batteries 2019, 5, 49.
[251] I. Laresgoiti, S. Käbitz, M. Ecker, D. U. Sauer, J. Power Sources 2015, 300, 112.
[252] J. Purewal, J. Wang, J. Graetz, S. Soukiazian, H. Tataria, M. W. Verbrugge, J. Power Sources 2014, 272, 1154.
[253] A. Verma, T. Kotaka, Y. Tabuchi, P. P. Mukherjee, J. Electrochem. Soc. 2018, 165, A2397.
[254] A. J. Crawford, D. Choi, P. J. Balducci, V. R. Subramanian, V. V. Viswanathan, J. Power Sources 2021, 501, 230032.
[255] L. Terborg, S. Weber, F. Blaske, S. Passerini, M. Winter, U. Karst, S. Nowak, J. Power Sources 2013, 242, 832.
[256] A. Bhandari, J. Bhattacharya, J. Electrochem. Soc. 2016, 164, A106.
[257] J. S. Edge, S. O'Kane, R. Prosser, N. D. Kirkaldy, A. N. Patel, A. Hales, A. Ghosh, W. Ai, J. Chen, J. Yang, S. Li, M.-C. Pang, L. Bravo Diaz, A. Tomaszewska, M. W. Marzook, K. N. Radhakrishnan, H. Wang, Y. Patel, B. Wu, G. J. Offer, Phys. Chem. Chem. Phys. 2021.
[258] X. Lin, J. Park, L. Liu, Y. Lee, A. M. Sastry, W. Lu, J. Electrochem. Soc. 2013, 160, A1701.
[259] R. Behrou, K. Maute, ECS Trans. 2017, 77, 1163.
[260] R. Behrou, K. Maute, J. Electrochem. Soc. 2017, 164, A2573.
[261] R. Xu, Y. Yang, F. Yin, P. Liu, P. Cloetens, Y. Liu, F. Lin, K. Zhao, J. Mech. Phys. Solids 2019, 129, 160.
[262] P. Liu, R. Xu, Y. Liu, F. Lin, K. Zhao, J. Electrochem. Soc. 2020, 167, 040527.
[263] H. Wang, S. P. V. Nadimpalli, V. B. Shenoy, Extreme Mech. Lett. 2016, 9, 430.
[264] P. Li, Y. Zhao, Y. Shen, S.-H. Bo, J. Phys. Energy 2020, 2, 022002.
[265] D. Chen, D. Kramer, R. Mönig, Electrochim. Acta 2018, 259, 939.
[266] S. Kalnaus, K. Rhodes, C. Daniel, J. Power Sources 2011, 196, 8116.
[267] I. Ryu, J. W. Choi, Y. Cui, W. D. Nix, J. Mech. Phys. Solids 2011, 59, 1717.
[268] S. K. Vanimisetti, N. Ramakrishnan, Proc IMechE Part C: J Mechanical Engineering Science 2011, 226, 2192.

[269] H.-J. Kim, T. N. V. Krishna, K. Zeb, V. Rajangam, C. V. V. M. Gopi, S. Sambasivam, K. V. G. Raghavendra, I. M. Obaidat, Electronics 2020, 9, 1161.
[270] Y. Mao, X. Wang, S. Xia, K. Zhang, C. Wei, S. Bak, Z. Shadike, X. Liu, Y. Yang, R. Xu, P. Pianetta, S. Ermon, E. Stavitski, K. Zhao, Z. Xu, F. Lin, X. Q. Yang, E. Hu, Y. Liu, Adv. Funct. Mater. 2019, 29, 1900247.
[271] J. M. Foster, X. Huang, M. Jiang, S. J. Chapman, B. Protas, G. Richardson, J. Power Sources 2017, 350, 140.
[272] N. Iqbal, Y. Ali, S. Lee, J. Electrochem. Soc. 2020, 167, 060515.
[273] N. Iqbal, Y. Ali, S. Lee, J. Power Sources 2020, 457, 228019.
[274] P. Barai, K. Smith, C.-F. Chen, G.-H. Kim, P. P. Mukherjee, J. Electrochem. Soc. 2015, 162, A1751.
[275] C.-F. Chen, P. Barai, K. Smith, P. P. Mukherjee, Electrochim. Acta 2016, 204, 31.
[276] J. Lian, T. Wierzbicki, J. Zhu, W. Li, Eng. Fract. Mech. 2019, 217, 106520.
[277] Y.-T. Cheng, M. W. Verbrugge, J. Power Sources 2009, 190, 453.
[278] X. Jin, A. Vora, V. Hoshing, T. Saha, G. Shaver, R. E. García, O. Wasynczuk, S. Varigonda, J. Power Sources 2017, 342, 750.
[279] X. Jin, C. Liu, Electrochim. Acta 2019, 312, 188.
[280] W. A. Appiah, J. Park, S. Byun, M.-H. Ryou, Y. M. Lee, J. Electrochem. Soc. 2016, 163, A2757.
[281] A. Ghosh, J. M. Foster, G. Offer, M. Marinescu, J. Electrochem. Soc. 2021, 168, 020509.
[282] Z. Li, J. Huang, B. Y. Liaw, J. Zhang, J. Power Sources 2017, 348, 281.
[283] R. Xiong, J. Cao, Q. Yu, H. He, F. Sun, IEEE Access 2018, 6, 1832.
[284] L. Cai, R. E. White, J. Electrochem. Soc. 2010, 157, A1188.
[285] N. Jin, D. L. Danilov, P. M. J. Van den Hof, M. C. F. Donkers, Int. J. Energy Res. 2018, 42, 2417.
[286] R. Bermejo, P. G. d. Sastre, Appl. Math. Comput. 2019, 361, 398.
[287] V. R. Subramanian, V. D. Diwakar, D. Tapriyal, J. Electrochem. Soc. 2005, 152, A2002.
[288] Z. Deng, L. Yang, H. Deng, Y. Cai, D. Li, Energy 2018, 142, 838.
[289] S. Liu, Solid State Ion. 2006, 177, 53.
[290] Q. Zhang, R. E. White, J. Power Sources 2007, 165, 880.
[291] K. Chayambuka, G. Mulder, D. L. Danilov, P. H. L. Notten, Solid State Commun. 2019, 296, 49.
[292] J. C. Forman, S. Bashash, J. L. Stein, H. K. Fathy, J. Electrochem. Soc. 2011, 158, A93.
[293] L. Wu, K. Liu, H. Pang, Electrochim. Acta 2021, 368, 137604.
[294] V. Ramadesigan, V. Boovaragavan, J. C. P. Jr., V. R. Subramanian, J. Electrochem. Soc. 2010, 157, A854.
[295] J. Xu, T. Wang, L. Pei, S. Mao, C. Zhu, J. Power Sources 2020, 460, 228093.
[296] V. Senthil Kumar, J. Power Sources 2013, 222, 426.
[297] D. Di Domenico, A. Stefanopoulou, G. Fiengo, J. Dyn. Syst., Meas., Control 2010, 132, 061302.
[298] D. D. Domenico, G. Fiengo, A. Stefanopoulou, 17th IEEE International Conference on Control Applications 2008, 702.
[299] D. Zhang, B. N. Popov, R. E. White, J. Electrochem. Soc. 2000, 147, 831.
[300] M. Guo, G. Sikha, R. E. White, J. Electrochem. Soc. 2011, 158, A122.
[301] J. Li, K. Adewuyi, N. Lotfi, R. G. Landers, J. Park, Appl. Energy 2018, 212, 1178.
[302] R. Mehta, A. Gupta, Electrochim. Acta 2021, 389.
[303] K. Gopalakrishnan, G. J. Offer, IEEE Trans. Contro.l Syst. Technol. 2021, 1.

[304] Z. Khalik, H. J. Bergveld, M. C. F. Donkers, in *IEEE 58th Conference on Decision and Control (CDC)*, Nice, France 2019, 7740.
[305] Z. Khalik, M. C. F. Donkers, H. J. Bergveld, J. Power Sources 2021, 488, 229427.
[306] Y. Chaochun, International Journal of Electrochemical Science 2018, 1131.
[307] Y. Liu, Y. Huangfu, R. Ma, L. Xu, D. Zhao, J. Wei, 2019 IEEE Industry Applications Society Annual Meeting 2019, 1.
[308] W. Li, Y. Fan, F. Ringbeck, D. Jöst, X. Han, M. Ouyang, D. U. Sauer, J. Power Sources 2020, 476, 228534.
[309] X. Han, M. Ouyang, L. Lu, J. Li, J. Power Sources 2015, 278, 814.
[310] K. A. Smith, C. D. Rahn, C.-Y. Wang, IEEE Trans. Contro.l Syst. Technol. 2010, 18, 654.
[311] H. Li, W. Zhang, X. Yang, H. Jiang, Y. Wang, T. Yang, L. Chen, H. Shen, Electrochim. Acta 2019, 326, 134966.
[312] J. Sturm, H. Ennifar, S. V. Erhard, A. Rheinfeld, S. Kosch, A. Jossen, Appl. Energy 2018, 223, 103.
[313] X. Hu, F. Feng, K. Liu, L. Zhang, J. Xie, B. Liu, Renew. Sust. Energ. Rev. 2019, 114, 109334.
[314] L. Yao, S. Xu, A. Tang, F. Zhou, J. Hou, Y. Xiao, Z. Fu, World Electr. Veh. J. 2021, 12, 113.
[315] R. Xiong, L. Li, J. Tian, J. Power Sources 2018, 405, 18.
[316] Z. Khalik, H. J. Bergveld, M. C. F. Donkers, in *American Control Conference*, Denver, USA 2020, 2213.
[317] Z. Khalik, H. J. Bergveld, M. C. F. Donkers, in *American Control Conference*, New Orleans, USA 2021, 4414.
[318] Y. Gao, K. Liu, C. Zhu, X. Zhang, D. Zhang, IEEE Trans. Ind. Electron. 2021, 1.
[319] B. Liu, X. Tang, F. Gao, Electrochim. Acta 2020, 344, 136098.
[320] S. J. Moura, N. A. Chaturvedi, M. Krstić, J. Dyn. Syst., Meas., Control 2014, 136, 011015.
[321] C. Zou, C. Manzie, D. Nešić, A. G. Kallapur, J. Power Sources 2016, 335, 121.
[322] F. Feng, S. Teng, K. Liu, J. Xie, Y. Xie, B. Liu, K. Li, J. Power Sources 2020, 455, 227935.
[323] R. Xiong, *Battery management algorithm for electric vehicles*, Springer Nature, 2020.
[324] B. Trembacki, E. Duoss, G. Oxberry, M. Stadermann, J. Murthy, J. Electrochem. Soc. 2019, 166, A923.
[325] Z. Y. Jiang, Z. G. Qu, L. Zhou, W. Q. Tao, Appl. Energy 2017, 194, 530.
[326] J. Xu, Y. Wu, S. Yin, RSC Adv. 2017, 7, 14360.
[327] X. Lai, C. Jin, W. Yi, X. Han, X. Feng, Y. Zheng, M. Ouyang, Energy Storage Mater. 2021, 35, 470.
[328] M. Xu, R. Wang, P. Zhao, X. Wang, J. Power Sources 2019, 438, 227015.
[329] Z. Chu, X. Feng, L. Lu, J. Li, X. Han, M. Ouyang, Appl. Energy 2017, 204, 1240.
[330] A. Bielefeld, D. A. Weber, J. Janek, J. Phys. Chem. C 2018, 123, 1626.
[331] D. H. Kim, D. Y. Oh, K. H. Park, Y. E. Choi, Y. J. Nam, H. A. Lee, S. M. Lee, Y. S. Jung, Nano Lett. 2017, 17, 3013.
[332] A. Bielefeld, D. A. Weber, J. Janek, ACS applied materials & interfaces 2020, 12, 12821.
[333] M. Finsterbusch, T. Danner, C. L. Tsai, S. Uhlenbruck, A. Latz, O. Guillon, ACS applied materials & interfaces 2018, 10, 22329.
[334] N. Kamyab, P. T. Coman, S. K. Madi Reddy, S. Santhanagopalan, R. E. White, J. Electrochem. Soc. 2020, 167, 130532.

[335] H. Xu, B. Chen, P. Tan, W. Cai, W. He, D. Farrusseng, M. Ni, Appl. Energy 2018, 219, 105.
[336] Q. Wang, Z. G. Qu, Z. Y. Jiang, W. W. Yang, Appl. Energy 2018, 220, 106.
[337] G. Zhang, C. E. Shaffer, C.-Y. Wang, C. D. Rahn, J. Electrochem. Soc. 2013, 160, A610.
[338] S. V. Erhard, P. J. Osswald, P. Keil, E. Höffer, M. Haug, A. Noel, J. Wilhelm, B. Rieger, K. Schmidt, S. Kosch, F. M. Kindermann, F. Spingler, H. Kloust, T. Thoennessen, A. Rheinfeld, A. Jossen, J. Electrochem. Soc. 2017, 164, A6324.
[339] S. Carelli, M. Quarti, M. C. Yagci, W. G. Bessler, J. Electrochem. Soc. 2019, 166, A2990.
[340] C. M. Julien, A. Mauger, K. Zaghib, H. Groult, Inorganics 2014, 2, 132.
[341] G. Inoue, M. Kawase, J. Power Sources 2017, 342, 476.
[342] J. Landesfeind, H. A. Gasteiger, J. Electrochem. Soc. 2019, 166, A3079.